

# **Evolution of Galaxies- Star Formation Histories in Nearby Spheroids**

**Mark Steven Northeast**

A thesis submitted in partial fulfilment of the requirements for the degree of  
Doctor of Philosophy, at the  
Centre for Astrophysics  
Department of Physics, Astronomy and Mathematics  
University of Central Lancashire

**September 2006**

## Student Declaration

### Concurrent registration for two or more academic awards

Either \*I declare that while registered as a candidate for the research degree, I have not been a registered candidate or enrolled student for another award of the University or other academic or professional institution

or ~~\*I declare that while registered for the research degree, I was with the University's specific permission,~~  
a \*registered candidate/\*enrolled student for the following award:

---

### Material submitted for another award

Either \*I declare that no material contained in the thesis has been used in any other submission for an academic award and is solely my own work.

or ~~\*I declare that the following material contained in the thesis formed part of a submission for the award of~~

---

(state award and awarding body and list the material below):

### Collaboration

Where a candidate's research programme is part of a collaborative project, the thesis must indicate in addition clearly the candidate's individual contribution and the extent of the collaboration. Please state below

Signature of Candidate



Type of Award

DOCTOR of PHILOSOPHY

Department

PHYSICS, ASTRONOMY & MATHEMATICS

# Abstract

This thesis is about an investigation into the formation of spheroidal type galaxies. The investigation began with modelling studies of early-type galaxies and spiral bulges (SBs). From galaxy formation modelling studies led by experiments with a sample galaxy, some results were obtained; non-solar abundance ratios in Elliptical galaxies (Es) achieved better fits between model and data than solar abundance ratios. For both early-type and late-type galaxies, best fits with non-solar abundance ratios were more constrained than in the solar abundance ratio case. A strong link between star formation histories and the supernova Ia rate for the early and late-type galaxies was shown. The model code itself was tested by way of pseudo galaxy experiments, and shown to reliably reproduce model parameters. In the topic area of galaxy formation, regions of spectra particularly sensitive to a galaxy's age and metallicity were measured as equivalent widths and then calibrated to the common scale of the Lick Indices. The Lick Indices were used in deriving all key results throughout the thesis.

The modelled sample of galaxies from Proctor & Sansom (2002) lacked data on low velocity dispersion ( $\sigma$ ) galaxies for line strengths versus kinematics correlations. In regards to low  $\sigma$  galaxies, Low Luminosity Es (LLEs) were considered to be likely candidates. Long-slit spectra of a sample of 12 LLEs, taken at the European Southern Observatory New Technology Telescope, were sub-selected for their low velocity dispersions. The spectra of 10 of these LLEs were successfully reduced. Line strengths and kinematics were measured. The Lick Indices of these LLEs were correlated with velocity dispersion ( $\sigma$ ), alongside the previously modelled companion data set. Ages and metallicities of the LLEs were estimated. From these results, the LLEs were found to have significant correlations of line strength versus  $\sigma$  with SBs. However, the LLEs do not appear to be younger than SBs, but younger than Es. The LLEs seem to consist of a low metallicity group (possibly misclassified dwarf spheroidal galaxies) and a high metallicity group. Future possible work that may uncover which models of galaxy formation for high and low metallicity LLEs these results support is suggested.

# Contents

<b>1 Introduction</b>	<b>1</b>
1.1 Background to Elliptical Galaxy Formation .....	1
1.2 Background to GCE Modelling.....	2
1.3 Motivation for Thesis.....	4
1.3.1 Motivation for Observing Low Luminosity Elliptical Galaxies.....	5
1.4 Overview of Thesis.....	8
<b>2 Initial GCE Modelling Studies (WHT Data)</b>	<b>10</b>
2.1 Galactic Chemical Evolution (GCE) Modelling.....	10
2.2 Mass Loss.....	17
2.3 Supernovae Ia Rates.....	20
2.4 Sample Galaxy NGC 2831.....	25
2.5 Pseudo Galaxies.....	28
2.5.1 Test for a Perfect Match.....	29
2.5.2 The Perturbed Case.....	29
2.6 Testing Small Time Step (DT).....	31
2.7 Comparing Fineness of Parameter Space Searches by SSP and GCE Models.....	32
2.8 Comparing Solar vs. Non-solar Abundance Ratios.....	33
2.8.1 Contour Plots and Output Indices.....	34
2.9 Summary of Experiments on Sample Galaxy.....	38
2.10 All Galaxies.....	39
2.10.1 The WHT Data Set.....	40
2.10.2 Variation of Supernovae Rate.....	40
2.10.3 Solar Ratio vs. Non-Solar Ratio Experiments, Using WHT data..	43
<b>3 Observations and Initial Data Reductions of LLEs</b>	<b>47</b>
3.1 Preparations for Observations with EMMI on the NTT.....	47
3.2 Observations.....	52
3.3 Data reductions.....	54
3.4 Preparatory Steps for Measurement of Kinematics.....	68
<b>4 Derivation of Galaxy Kinematics, Line Strengths and Ages</b>	<b>70</b>

4.1	Measurements of Kinematics.....	71
4.1.1	Lick Calibration Star Radial Velocity Measurements.....	71
4.1.2	Measurement of Galaxy Kinematics.....	72
4.2	Lick Calibrations .....	75
4.2.1	Correction to Lick Spectral Resolution.....	75
4.2.2	Corrections for Velocity Dispersion Broadening.....	76
4.2.3	Flux-calibration Correction.....	77
4.3	Emission Corrections.....	79
4.4	Line Measurements and Errors.....	80
4.5	Galaxy Age Estimates.....	82
<b>5</b>	<b>Analysis of Results</b>	<b>83</b>
5.1	Line Strength versus Velocity Dispersion.....	83
5.2	Galaxy Ages.....	89
5.3	Discussion of Results.....	92
<b>6</b>	<b>Discussion, Conclusions and Future Work</b>	<b>97</b>
6.1	Discussion and Conclusions from GCE modelling.....	97
6.2	Discussion and Conclusions from Study of LLEs.....	99
6.2.1	Conclusions from Study of LLEs.....	99
6.2.2	Speculative Discussion from Study of LLEs.....	101
6.3	Future work.....	102
	<b>Appendices</b>	<b>105</b>
A	GCE code detailed.....	105
B	Proto-type web-site.....	106
C	Critical Values for Pearson's r.....	116
	<b>Bibliography</b>	<b>117</b>

## List of Tables

2.1 Model input parameters .....	13
2.2 Example Model Input Parameters Used by the GCE Code.....	14
2.3 Comparison of times for IMFMR from Wood (1992) and Kauffman (1994).....	19
2.4 Mass dependant stellar MS lifetimes and MS to WD lifetimes.....	20
2.5 Observational SN Rates based on studies of various galaxy types.....	22
2.6 Model Parameters and Predicted SNIa Rates from Matteucci & Recchi (2001).....	23
2.7 NGC 2831 best fit model parameters for various SNIa rates.....	28
2.8 Perturbed Pseudo Galaxy Runs.....	30
2.9 Pseudo line strengths, including after perturbation.....	30
2.10 Differences in line strengths between solar and non-solar abundance ratio best fits, for different SNIa rates.....	35
2.11 $\chi^2$ for full WHT sample.....	42
2.12 $\chi^2$ for different galaxy types, for solar and non-solar ratios, with SNIa rate of $6.5 \times 10^{-5} M_{\odot} \text{Gyr}^{-1}$ .....	43
3.1 Galaxies observed with NTT.....	53
3.2 Calibration stars observed with NTT.....	54
3.3 Absolute and relative values for flux calibration stars.....	66
4.1 Radial velocity measurements of Lick calibration stars.....	72
4.2 Velocity dispersions and redshift for NTT.....	73
4.3 Values for calibration to Lick resolution.....	78
4.4 Lick Index sample errors.....	80
4.5 Lick Index Measurements of the NTT data set.....	82
5.1 Correlations between Lick indices and $\log(\sigma)$ , for Es/SOs.....	87
5.2 Correlations Lick indices, calculated for the NTT data set.....	88
5.3 Correlations between Lick indices and $\log(\sigma)$ , for late-types.....	89
5.4 NTT data set ages, and also [Fe/H].....	90
5.5 $\log(\sigma)$ against $\log(\text{Age})$ and also [Fe/H], for NTT data set.....	90

## List of Figures

1.1	Figure 4 from PS02.....	6
1.2	Figure 5 from CRC03.....	7
2.1	An overview block diagram of the GCE code 2003.....	11
2.2	Two different SFHs, from the same initial model input parameters.....	13
2.3	Variation of Line Strength of $Mg_b$ from its solar abundance ratio.....	17
2.4	Supernovae rate variation over time.....	24
2.5	NGC 2831 is shown with the larger cD galaxy, NGC 2832.....	26
2.6a	Example contour plot of non-solar model run.....	36
2.6b	Example contour plot of solar model run.....	37
3.1	EMMI optical layout.....	49
3.2	Sample finding charts.....	51
3.3	CCD frames.....	56
3.4	A debiased galaxy exposure mean spatial (x) profile before (top) and after (bottom) initial cosmic ray cleaning.....	60
3.5	The bias offsets, before being removed by debiasing.....	61
3.6	Residual step between frames after debiasing.....	61
3.7	Correlation in the shift found in cross-correlations of arcs to a reference arc.....	62
3.8	Division of normalised smooth interpolations of standard flux calibration spectrum by the observed flux calibrated spectrum.....	66
3.9	Nightly instrumental (normalised) response.....	67
3.10	Before and after using CLEAN (i.e. on NGC2328) to remove residual CRs.....	68
4.1	$C_i$ versus $\sigma_c$ , sample plots.....	77
5.1a	Metallicity-sensitive indices plotted against $\log(\sigma)$ .....	84
5.1b	Metallicity-sensitive indices plotted against $\log(\sigma)$ .....	85
5.2	Age sensitive indices versus $\log(\sigma)$ .....	86
5.3	$\log(\text{Age})$ versus $\log(\sigma)$ , of NTT and WHT data sets.....	90
5.4	$[\text{Fe}/\text{H}]$ versus $\log(\sigma)$ , of NTT and WHT data sets.....	91
5.5	$[\text{Fe}/\text{H}]$ is plotted against $\log(\text{Age})$ .....	91

# Acknowledgements

The road to completion of this thesis has been one not journeyed entirely alone. Amongst the helpers that kept the thesis from being just that little bit too far over the horizon, are those that gave brief respite for weary legs, those that gave food for thought and those that offered me a lift part way. Then there are those from whom I no doubt gleaned advice and skill before even beginning this venture. There are even those I no doubt learned from without even realizing I had.

Many thanks are due to them all. I should like to thank my supervisory team, especially my primary supervisor Dr. Anne Sansom, for making the PhD possible, and for continuing to make it possible till the very end. My thanks to Dr. Barbara Hassall and my PhD research predecessor Dr. Rob Proctor for their acts of encouragement, besides their technical helps.

On a very practical side, my thanks go first to Dr. Steve Higgins for introducing me to c-shell, that most favoured and trusted walking stick of mine on this long journey. My great gratitude to Steve Chapman, Andreas Papageorgiou and Barbara Ridding for helping me so many times to rebuild either desktop PC or laptop, and also debug operating systems, attempt to recover corrupted back-up files and so on and so forth. They were each like a well chalked hand-hold and foot hold on an otherwise particularly greasy part of a climb. I also thank Dr. Dave Berry and Malcolm Currie for their helps and advice on syntax, debugging, and questions on Starlink packages. They were like a well made compass in a white-out snow storm.

I owe much to Dr. Lars Freyhammer for his technical insights and for both his and John Riley's kind words of research advice. Along a similar vein my thanks go to Dr. Katrien Uytterhoeven and Dr. Andrei Sokolov. All four were great "traveling" companions.

I should also like to thank my wife for her great support whilst completing this PhD. She has been like a sturdy rock in the sun I can lean my back against. Finally, my thanks go to my family, for all the countless things of theirs I am no doubt taking for granted. Many acknowledgements and thanks to them.

# Abbreviations

ADU.....	(Analogue Digital Unit)
AGB.....	(Asymptotic Giant Branch)
bc.....	(Barycentric correction)
BH.....	(Black Hole)
BIMG.....	(Blue Imaging Mode)
CRC03.....	(Caldwell, Concannon and Rose 2003)
GCE.....	(Galactic Chemical Evolution)
dex.....	(A logarithmic unit used in Astronomy. The name “dex” is a contraction of “decimal exponent”. For example, -0.1 dex is $10^{-0.1}$ ).
DSS.....	(Digital Sky Survey)
dSph.....	(Dwarf spheroidal galaxy)
E.....	(Elliptical galaxy)
EMMI.....	(ESO Multi-Mode Instrument)
ESO.....	(European Southern Observatory)
HMS.....	(High Mass Star)
IMF.....	(Initial Mass Function)
IMFMR.....	(Initial Mass Final Mass Relation)
IMS.....	(Intermediate Mass Star)
LBV.....	(Luminous Blue Variable)
LLE.....	(Low Luminosity Elliptical galaxy)
$M_B$ .....	(Bolometric magnitude)
MS.....	(Main Sequence)
NAM.....	(National Astronomical Meeting)
NASA ADS.....	(National Astronomical and Space Administration Archive Data Service)
NED.....	(Nasa Extragalactic Database)
NTT.....	(New Technology Telescope)
PA.....	(Position Angle)
PS02.....	(Proctor and Sansom 2002)
RC3.....	(The Third Reference Catalogue of Bright Galaxies)

REMD..... (Red Medium Dispersion Spectroscopy)  
SO, SOa..... (Lenticular galaxy)  
Sa, Sab, Sb..... (Late-type galaxies in the Hubble type classification system, between E and Irregular)  
SB..... (The central bulge part of a spiral galaxy)  
SDSS..... (Sloan Digital Sky Survey)  
SFH..... (Star Formation History)  
SFR..... (Star Formation Rate)  
SN..... (Supernovae)  
SNe..... (Supernovae explosion)  
SNIa..... (Supernovae Ia)  
SNII..... (Supernovae II)  
SNu..... (Supernova Units)  
SPS03..... (Stellar Population Synthesis conference 2003)  
SSP..... (Single Stellar Population)  
SW..... (Stellar Wind)  
WD..... (White Dwarf star)  
WHT..... (William Herschel Telescope)  
WMAP..... (Wilkinson Microwave Anisotropy Probe)  
WR..... (Wolf-Rayet stars)

# Chapter 1

## Introduction

### 1.1 Background to Elliptical Galaxy Formation

In the development of galaxy formation, Elliptical galaxies (Es) play an important role. E galaxies do not have the added complication of spiral arms to model that spiral galaxies have, so they make a logical choice for a first step in attempts to model the observed spectra of galaxies.

The picture of spheroidals (i.e. Es, Lenticulars and spiral bulges) presented by Baade (1944a, b), was one of objects consisting of old, red stars. Younger, bluer star populations he observed as being situated in the spiral arms of spiral galaxies. Models of galaxy formation in regard to spheroidals were thus initially designed upon the belief that the spheroidals were formed by single starbursts, sometime during the age of the Universe.

Single Stellar Population (SSP) models have the simple approach of synthesising the observed population of a galaxy by approximating the origin of the population to a single starburst (e.g. Tinsley 1974, 1981). Such a starburst produces in models a population of stars that forms at a single epoch with a specific mass function. For single stellar populations the evolution of such a population is well understood and forms the basis for understanding globular clusters. SSP models allow researchers to calculate the change in a population's colour and spectrum, dependant upon the initial  $Z$  ( $Z$ , defined in section 2.1) and time over which the population is allowed to develop (e.g. Buzzoni 1989, Sil'chenko 2006).

Models for Galactic Chemical Evolution (GCE) are the next step beyond SSP models. This is since multiple generations of stars are believed to have been made since galaxies first began to form. In the Milky Way Galaxy and nearby galaxies star formation is observed. Further, in these galaxies old stars from an earlier population and resolved stars are observed with non-

primordial abundances. This suggests a star formation history (SFH) that includes chemical enrichment of stars by the recycling of material from an unobserved earlier population of stars. GCE models are designed to uncover the SFH of galaxies (i.e. Es and Lenticulars).

A possibility for the formation of spheroidals, in particular Es that show evidence for younger stars, is that of the hierarchical clustering (e.g. Cole et al., 1994). In hierarchical clustering scenarios, a galaxy forms as it accretes (by way of merger events) smaller galaxies. Such scenarios would lead to complex Star Formation Histories (SFHs), which lend themselves in particular, to GCE modelling (e.g. Proctor, PhD thesis, 2002).

However, evidence in support of monolithic collapse remains. For example, the work of Kodama & Arimoto 1997, who used the dissipative collapse picture of Larson (1974) to explain observations of Es in their models. Monolithic collapse to some extent at least may yet explain the evolution of some spheroidals. Further discussion of GCE modelling is given in section 2.1.

Bender, Burstein & Faber (1992) suggested that dynamically hot galaxies (i.e. high mass, compact spheroidals such as spiral bulges and giant Es) form increasingly as a result of mergers of whole galaxies as opposed to gaseous mergers of smaller systems. That is to say, the more massive a galaxy, the more strongly a hierarchical merger mechanism may have affected the SFH of the galaxy. If this is so, the less massive, Low Luminosity Ellipticals (LLEs), could form important building blocks to larger E galaxies.

Some studies involving LLEs have considered the velocity dispersion ( $\sigma$ ) of these galaxies in relation to the line strengths, as well as sought to identify ages (e.g. Halliday, PhD thesis, 1998, Caldwell, Concannon & Rose 2003).

## **1.2 Background to GCE Modelling**

The cosmic cycle represents the mass transfer between stars and the interstellar medium (ISM) in galaxies and vice versa via successive

generations of star "birth" (e.g. a starburst) and star "death" (e.g. supernovae - SNe). This mass transfer lies at the centre of any GCE model. Stars of different masses form in each new generation, in accordance with an initial mass function (IMF). Two main theories are found throughout the literature as to the formation of early-type (i.e. E and SO) galaxies.

E galaxies could form monolithically by gravitational collapse of gas cloud(s) (see Arimoto & Yoshii 1987). Alternatively Es could form initially via mergers of relatively small galaxies (hierarchical collapse, see Lacey & Cole 1994).

The conventional hypothesis is that Es and Lenticulars (SOs) formed early on in the Universe (e.g. Binney and Tremaine, 1987, Chapter 9, p. 553). However, recent research suggests that galaxies formed at various times throughout the age of the Universe (see Trager et al. 2000, Proctor and Sansom 2002, hereafter PS02, and Dekel & Cox 2006).

The apparent redness of a galaxy's light may be due to age (light output dominated by old stars) or  $[Z/H]$  (the galaxy has an appreciable population of young stars, but their light is reddened due to their high  $[Z/H]$ ). From Worthey (1994), if the change of age ( $\Delta\text{age}$ ) with respect to change of  $[Z/H]$  ( $\Delta Z$ ) approximately equals  $3/2$  for two populations, then the spectra will appear almost identical. A few spectral line strengths (the Lick Indices) have been established as standards. Some of these Lick Indices break this age- $[Z/H]$  degeneracy by being age or abundance sensitive (see Worthey et al., 1994). The Lick Indices are discussed further in section 2.1.

Research into galactic evolution is now driven at least partly by GCE, as made apparent in the Stellar Population Synthesis conference 2003 (hereafter SPS03). Research into galaxy formation is generally concerned with developing GCE models, as well as attempting to improve SSPs on which the GCE models are based (for example Trager et al. 2000; Thomas, Maraston and Bender 2003a). Though some researchers use multi-zone models (see Tantalo et al. 1998), these require a far greater level of complexity (since the dynamics of the gas flow then have to be modelled) in the design of the model and computer code. Multi-zone modelling is beyond the scope of this author's work.

Currently, researchers continue to look for ways to improve GCE models. This includes examination of the effect on fits of variable model IMF (e.g. Ballero, Matteucci & Chiappini 2006), chemical enrichment from supernovae Ia (Matteucci 2005) and new synthesis of stellar populations (e.g. Trager et al. 2005).

### 1.3 Motivation for Thesis

This research began centered on chemical evolution modelling of nearby Es and spiral bulges (SBs), using the William Herschel Telescope (WHT) data set introduced in section 2.10.1. After initial modelling studies, a decision was made to focus the research onto an under-observed galaxy type, the LLEs.

In work detailed in PS02, correlations between line strength and  $\sigma$  had been looked for. In regards to metal sensitive line strength versus  $\sigma$  plots (see Figure 1.1) the WHT data set lacked galaxies with low  $\sigma$  values; Below about  $79 \text{ km s}^{-1}$  plots were lacking data points. Whether a continuation of the correlations found for SBs existed at low  $\sigma$  or not remained uninvestigated. For the early-type galaxies in the WHT data set the correlations lacked a sufficient range in  $\sigma$  to achieve a significant Pearson's  $r$  correlation. The trend lines taken from Kuntschner 2000, hereafter K000, for early-type galaxies were thus where possible included in line strength versus  $\sigma$  plots in PS02. The principal aims of this thesis became to answer these questions:

- How will observed low  $\sigma$  galaxies correlate with the WHT late-type galaxies?
- How, if at all, will low  $\sigma$  data points fall on the extrapolations of the K000 early-type galaxy trend lines given in PS02?

Other researchers (i.e. Caldwell, Concannon and Rose 2003, hereafter CRC03) have observations of low  $\sigma$ , early-type galaxies. However, the errors on these observations make confident identification of trend lines at low  $\sigma$  difficult. LLEs are expected to be generally of lower  $\sigma$  than more luminous E galaxies. This expectation follows the line of thought that with regard to a given morphological type (i.e. Es) lower luminosity implies lower mass (from the mass luminosity relation); which in turn implies lower  $\sigma$  (from the Virial theorem).

As such LLEs are a good choice for low  $\sigma$  observing targets, though to be sure a few of those selected were of known low  $\sigma$ . The focus of this thesis was shifted from GCE modelling to the measurement of the kinematics and line strengths of a sample of LLEs. The main objective became to search for correlations that could be compared to trends reported in PS02. The motivation behind the LLE observations is discussed further below.

### **1.3.1 Motivation for Observing Low Luminosity E Galaxies**

As mentioned above, observations of low  $\sigma$  galaxies were designed in part to provide further points to the line strength versus  $\sigma$  plots provided by PS02 (reproduced here in Figure 1.1). For comparison to Figure 1.1, plots are given below in Figure 1.2 taken from CRC03.

Comparing the plots, the relatively low errors provided by PS02 are evident. The observations of LLEs for this Thesis work were designed so as to provide at least comparable errors in line strengths to those achieved by PS02, by using an appropriate large diameter telescope, and sufficiently long exposure times for good signal to noise (at around  $\sim 70$  for galaxy exposures). The signal to noise ratios measured are mentioned in section 3.2.

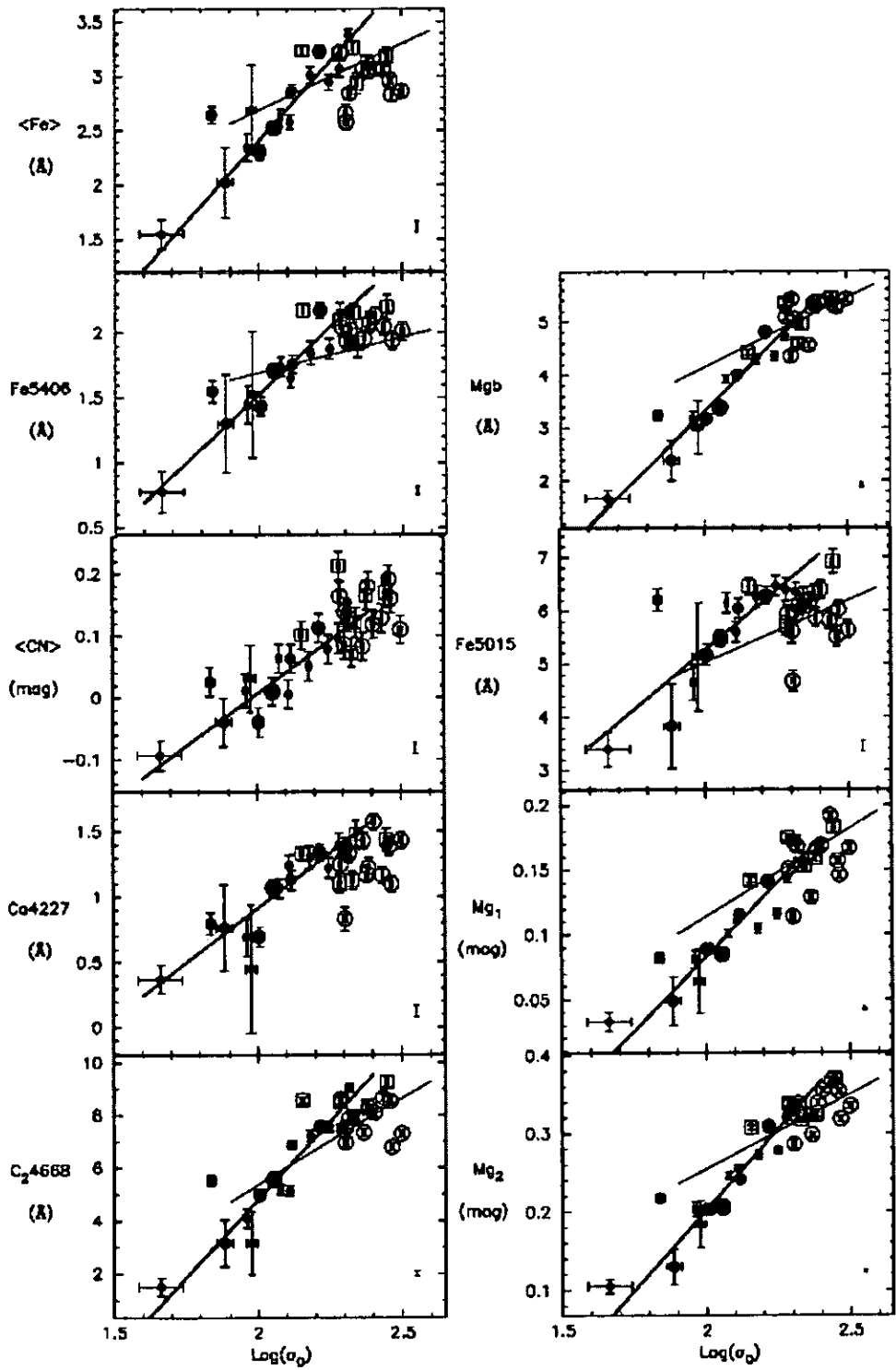


Figure 1.1: Figure 4 from PS02. Thick lines are fits to the spiral bulge data (solid symbols with symbol size largest for SOa and smallest for Sbc). Open symbols show early-type galaxies (circles for Es and squares for SOs). Thin lines show trends for early-type galaxies (from Kuntschner 2000). Below  $\log(\sigma) \approx 1.89$  (about  $79 \text{ km s}^{-1}$ ) there is but one data point, at  $\log(\sigma) \approx 1.62$  ( $42 \text{ km s}^{-1}$ ), apart from that of NGC 4313 at  $\log(\sigma) \approx 1.83$  which was omitted from correlations in PS02. It is in this bottom end of the plots that data was sought via the observing run applied for.

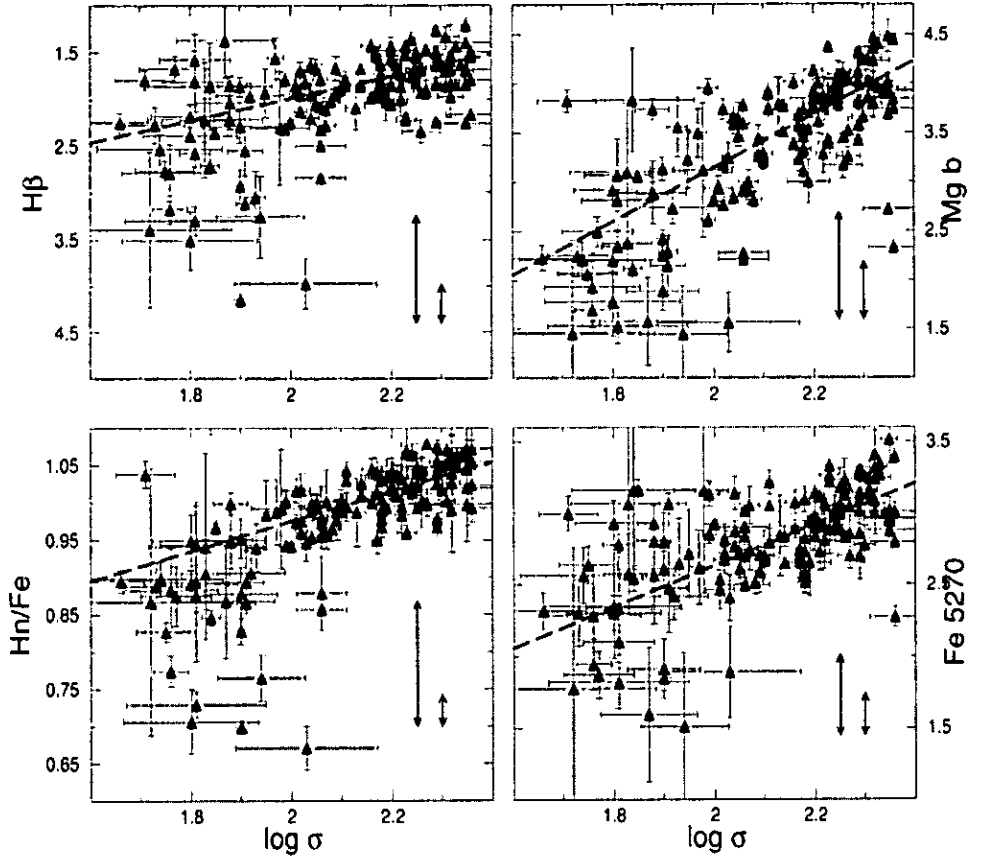


Figure 1.2: Figure 5 from CRC03, showing line strengths versus  $\log(\sigma)$ . The vertical arrow headed error-bars in the bottom right corner of each panel are representations of the measured intrinsic scatter in the high- $\sigma$  galaxies ( $\log(\sigma) > 2.0$ ; right) and the low- $\sigma$  galaxies ( $\log(\sigma) < 2.0$ ; left).

An observing run was sought at the European Southern Observatory's (ESO's) New Technology Telescope (NTT), by Dr. A. Sansom (the author's research supervisor). This was for the purpose of the author gathering data for the thesis, whilst acquiring observing experience; all of which was achieved as described in Chapter 3. The selection of instrumentation meant that observations would, potentially, be of competitive signal-to-noise and dispersion to existing observations (e.g. Halliday, PhD thesis, 1998, and CRC03). Should correlations between Z sensitive line strengths and  $\sigma$  be confirmed by measurements of a new data set of galaxies of relatively low  $\sigma$  to the WHT data set, some further possible questioning arises:

- What galaxy formation mechanism do the LLE galaxies appear to support?
- Time permitting to measure them, what ages do the LLE galaxies appear to have?

## **1.4 Overview of Thesis**

The work of this thesis introduced in this chapter unfolds as follows. In Chapter 2 the initial modelling studies of the WHT data set are detailed. The GCE model used is introduced and discussed, as well as the choice of a sample galaxy with which to begin investigations. The design of modelling experiments drew upon the findings of a literature review, and these findings are reported. These modelling experiments are then expanded where appropriate to include the whole WHT data set, and the results discussed.

In Chapter 3 the observations of LLEs and data reductions are discussed. This begins with discussion of preparatory steps for observations for a necessary understanding of the instrumentation involved as well as the choice of galaxies to observe. The data reduction procedures are outlined, with some of the main problems encountered detailed. This includes the handling of the separate frames of the CCD used and the cleaning of spectra of galaxies with large amounts of emission.

Chapter 4 details the measurement of relevant galaxy and star kinematics, needed for calibration to a common scale so as to make results comparable to that of other researchers. Calibrations to galaxy spectra designed to counter the affect of emission on spectra are discussed. Finally, the measurement of line strengths in galaxies is detailed, and the age estimates using those line strengths as inputs to appropriate SSP software.

Chapter 5 presents age estimates and the results of line strength measurements of the observed galaxies, and appropriate plots of those line

strengths against  $\log(\sigma)$ . What these plots may indicate is discussed, in regards to intercomparison of different Hubble types at low  $\sigma$ . The galaxy age estimates are also discussed.

In Chapter 6 the results and conclusions of the thesis are summarised and discussed. A speculative discussion regarding which galaxy formation model the results seem to support is included. Lastly suggestions for future work are given.

## Chapter 2

### **Initial GCE Modelling Studies (WHT Data)**

Initial studies of the GCE model are detailed, where significant results were found, such as those pertaining to the fineness of parameter space when comparing SSP and GCE modelling (section 2.7). This section discusses supernovae (section 2.3 and subsection 2.10.2) and delayed feedback (section 2.2).

#### **2.1 Galactic Chemical Evolution (GCE) Modelling**

Software has been written, using Fortran 90, on Starlink to model GCE, which will be referred to hereafter as "the GCE code" (Sansom and Proctor 1998 give an early description of the GCE code). The model embodied by the GCE code will be referred to as "the GCE model". The GCE code in this software not only defines the GCE model, but also controls the data processing of the model and data producing the outputs for the user to study. The GCE code essentially fits model parameters and finds best fit indices (otherwise known as best fit "line strengths"); for a single set of model parameters the code finds a solution. The GCE code itself is under continued development (by Dr. A. Sansom). A diagram of the current GCE code is given in Figure 2.1, with more detailed diagrams given in Appendix A.

Overview Block diagram of GCE code.  
30/07/2003

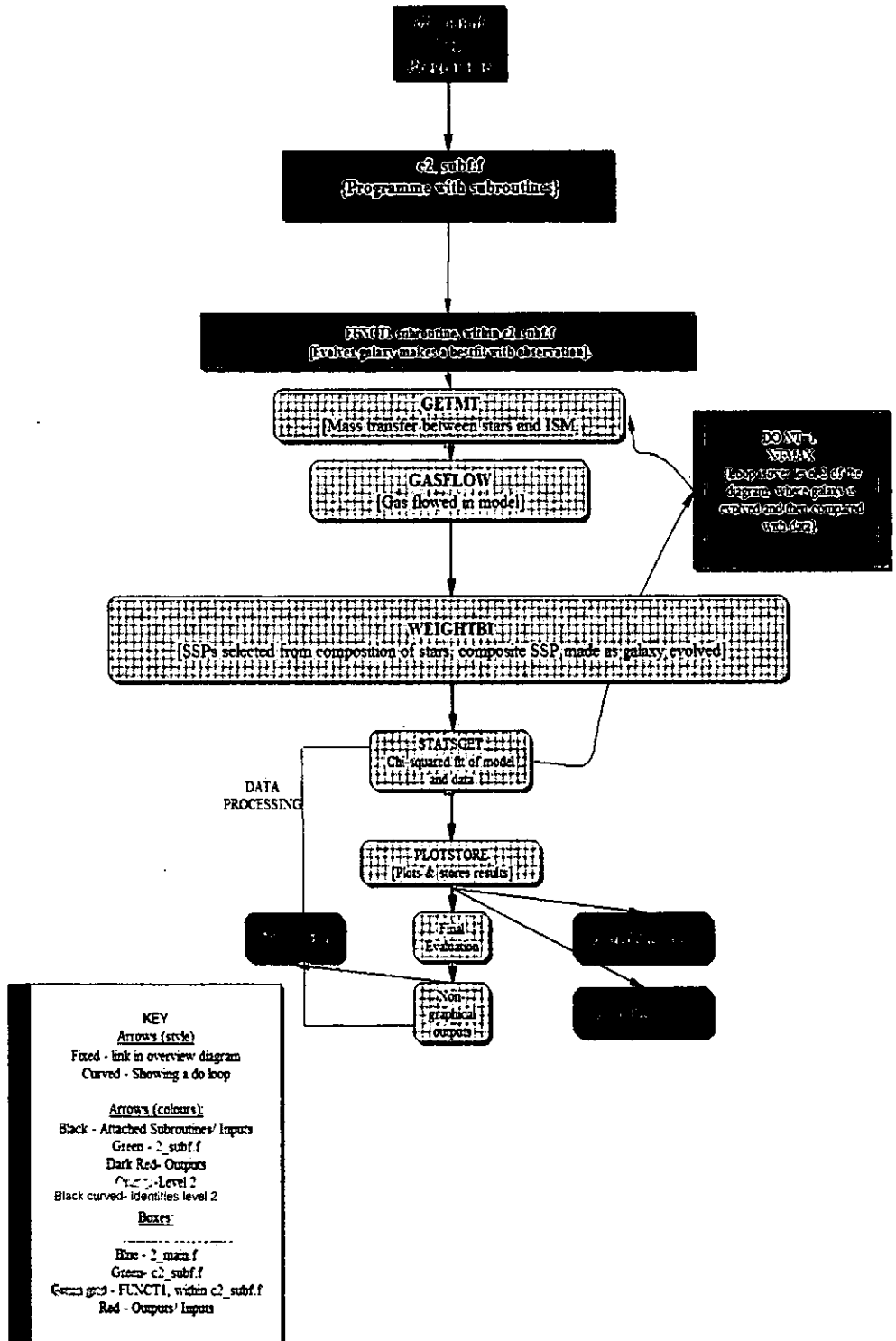


Figure 2.1: An overview block diagram of the GCE code 2003. The NT=1 to NTMAX loop starts within the GETMT block and loops back from within the STATSGET block; see Appendix A for an expansion of this loop.

In Figure 2.1, the main loop (DO N=1 to NTMAX) is completed in every time step, the size of which is the time resolution of the GCE code. DT (in the current version of the GCE code) is the time resolution of the GCE model, the time the model galaxy is evolved divided by the number of steps that the code goes through as it evolves the model galaxy. A typical step size for DT could be 0.1 Gyr. The size of DT is limited by the age of the model galaxy (i.e. currently 17 Gyr) as an upper limit and in its lower limit by the amount of working memory from the hardware used to run the GCE code (currently leading to a DT of no less than about 0.01 Gyr). As an absolute lower limit, DT is also limited by the time stars take to get onto the MS. As the time resolution of the GCE code is increased, the amount of computing time per model run increases factorially with the number of increasing time steps. Where little star formation (SF) is occurring as the model galaxy is formed, larger values of DT could be used to decrease the amount of computing time required for runs of the GCE code. This is an extension to the model completed in 2004 (Sansom, A., private communication).

The user may define certain model input parameters, such as type of Initial Mass Function (IMF), before running the model in either single step or multi-step mode. The single-step mode generates a single SFH (from fixed model input parameters). The multi-step mode tries 4320 SFHs in its search for the best model versus data fit (from fixed and non-fixed model input parameters). Table 2.1 describes the parameters searched by the multi-stepping software, which are some of the key variables characterising a galaxy's SFH. The GCE code tries several discrete values for each searched model input parameter in each run of the model. A four dimensional grid space is thus searched. This grid space shall be referred to in this report as the "parameter space". The SFH may vary greatly by altering one of the key variables, as shown in Figure 2.1.

Searched		
Variables	Short Description	Units
		$\text{Gyr}^{-1}$ (for $\alpha=1$ )
C1	The parameter "C" which serves as the efficiency coefficient of the SF rate (SFR, see Table 2.2).	
F1	Gas inflow rate into the ISM, from the intergalactic medium, or an external galaxy.	$M_{\odot} \text{Gyr}^{-1}$
T1	The 1st discrete time change in the SFH.	Gyr
T2	The 2nd discrete time change in the SFH.	Gyr
Other		
Parameters:	C0=initial efficiency of SFR. C2=final efficiency. F0=initial inflow rate. F2=Final inflow rate. Salpeter IMF is assumed. The SN1a rate is varied. Initial gas mass assumed is $10^6 M_{\odot}$	

Table 2.1: Model input parameters.  $\alpha$  is defined as the power in the equation for Star Formation Rate given in Table 2.2.

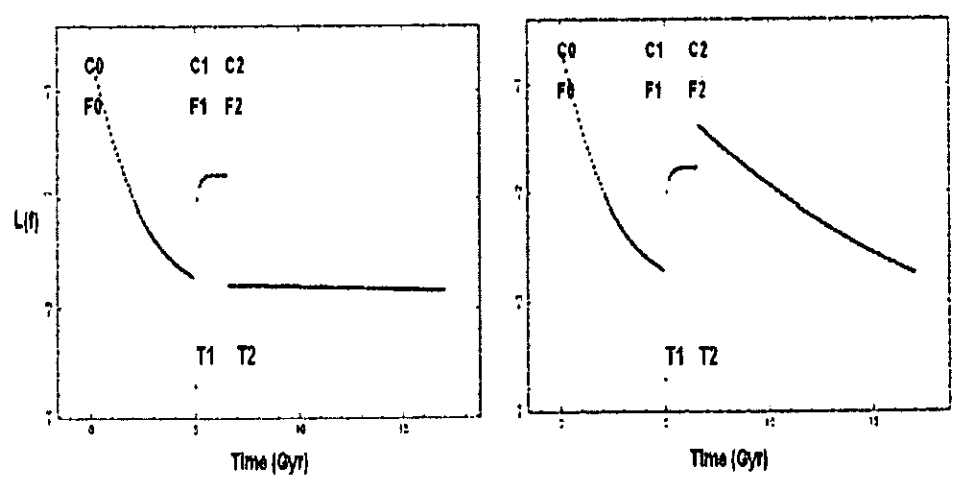


Figure 2.2: Two different SFHs, from the same initial model input parameters, except a C2 of 0.02 on the left and 0.5 on the right. The vertical axis represents the log of the SFR, with  $L(f) \sim 1$  to 4.5. Labels and units of parameters are as given in Table 2.1, units for axes are  $\text{Log}(\text{Gyr}^{-1})$  in the vertical and Gyr in the horizontal.

Parameter	Example Values	Short description
NRR	1	Number of radial ranges
C0	2	Constant (C) in $SFR=C\rho^a$ ( $Gyr^{-1}$ if $AL=1$ )
AL	1	Index in SFR eqn.
RCRIT	0	Critical density for Star Formation
FLOSSLIM	0.1	Fractional limit for significant mass loss ( $M_{\odot}$ )
SNIA RATE	3.80E-05	SN Ia Number ( $M_{\odot}^{-1} Gyr^{-1}$ )
DT	0.1	Time step (Gyr)
F0	0	Inflow ( $M_{\odot}^{-1} Gyr^{-1}$ )
SNH	70	SN II highest mass limit
AM	1.35	Index for IMF (1.35=Salpeter)
TYPIMF	S	S=Single slope IMF M=Modified IMF
SSPDATA	V	SSP data: W=Worthey94 V=Vazdekis99
X0	0.7718	Initial H mass fraction in gas
Y0	0.228	Initial He fraction in gas
M0	0.0002	Initial metal fraction in gas
T1	5	1st discrete time change (Gyr)
C1	0.2	1st changed SFR constant ( $Gyr^{-1}$ )
F1	$1.00 \times 10^7$	1st changed inflow rate ( $M_{\odot}^{-1} Gyr^{-1}$ )
T2	6.575	2nd discrete time change (Gyr)
C2	0.03	2nd changed SFR constant ( $Gyr^{-1}$ )
F2	0	2nd changed inflow rate ( $M_{\odot}^{-1} Gyr^{-1}$ )
RICH	Y	Enriched inflow (Y or N)
BHMASS	6	Mass of CO core for BH formation ( $M_{\odot}$ )
TIME	17	Time since stars started forming (Gyr)

Table 2.2: Example model input parameters used in the GCE code. Parameters in bold are stepped through in the multi-step version of the GCE code. The equation for star formation rate (SFR) is given in the description for C0. M0 is the initial metal mass fraction, which in the GCE code itself is symbolised as Z0. However, Z is used elsewhere for “metallicity”.

Finally, the GCE code has been adapted (using the models of Tripicco & Bell 1995, as described in PS02) to include non-solar abundance ratios in SSP indices; where the GCE code required a non-solar SSP, an appropriate solar SSP was adapted by way of  $\alpha$ -element enhancement following the model of Tripicco & Bell (1995). Throughout this thesis, where the term “non-solar” is applied, the meaning of this term is as used in PS02; the  $[\text{Fe}/\text{H}]$  (defined in equation 2.1) for a non-solar SSP (i.e.  $[\text{Fe}/\text{H}] < 0$ ) is adapted by way of adding the summed enhancement of  $\alpha$ -elements enhanced with respect to Fe peak elements (PS02). In the range  $-1 < [\text{Fe}/\text{H}] < 0$ ,  $[\text{Z}/\text{H}]$  (which is all the elements combined with respect to H) is  $0.63[\text{Fe}/\text{H}]$  (PS02). Since research has shown non-solar ratios predominate in the stellar atmospheres of stars in galaxies, including the Milky Way, modern models of GCE incorporate non-solar abundance ratios (e.g. Trager et al. 2000, PS02 and Thomas, Maraston and Bender 2003b). GCE research centres on modelling Lick indices (e.g. Trager et al. 2005). Lick indices were formulated (originally developed for generating SSP indices) by a number of researchers (e.g. Faber et al., 1985, Worthey 1994). Worthey (1994) generated some indices from optical observations of stellar spectra: CN1, CN2, Ca4227, G4300, Fe4383, Ca4455, Fe4531, Fe4668, H $\beta$ , Fe5015, Mg1, Mg2, Mgb, Fe5270, Fe5335, Fe5406 and the Ca triplet. Worthey & Ottaviani (1997) generated 4 more indices: H $\delta$ A, H $\delta$ F, H $\gamma$ A and H $\gamma$ F.

These 24 Lick Indices include Z sensitive features (such as Fe5015), and age sensitive features (e.g. H $\beta$ , H $\delta$  and G4300), as predicted by the SSP models (Worthey 1994 and Vazdekis et al. 1999). Z is the fraction of metals in the gas of a galaxy/ stellar photosphere where H and He make up the rest of the elements, often written as  $[\text{Z}/\text{H}]$ . Z is often inferred in GCE research from  $[\text{Fe}/\text{H}]$ , such as discussed in relation to the GCE code above. This is the Z that shall be referred to throughout this thesis.  $[\text{Fe}/\text{H}]$  is conventionally taken to be as shown in equation 2.1 (Carroll and Ostlie p. 920, 1996):

$$[\text{Fe}/\text{H}] = \log_{10}(\text{N}_{\text{Fe}}/\text{N}_{\text{H}})_{\text{star}} - \log_{10}(\text{N}_{\text{Fe}}/\text{N}_{\text{H}})_{\odot} \quad (2.1)$$

Where  $N$  refers to the number density of the elements in the relevant suffixes. The more accurately a code predicts these line strengths, the more reliable the model is thought to perhaps be.

Indices are believed dependant upon  $Z$ , and thereby the abundance of Fe (e.g. Puzia et al. 2002). Fe does not however need to relate directly to the abundance of other elements. The Lick indices, as modelled by Tripicco and Bell (1995), are more affected by the abundance of C and Mg than  $Z$ . This effect is modelled and formulated further by Trager et al. (2000) and then as a modification of the GCE code by PS02 (as discussed above in relation to  $[Z/H]$ ). In the GCE model we consider the effect of enhancement of Lick indices ( $i$ ) from their solar abundance ratio (see PS02) values ( $I_i$ ), following the Lick Index prescribed estimate,  $I_i'$ , laid down by Trager et al. (2000):

$$I_i' = I_i [(1 + R_{i,X1})^{E_{X1}/\log 2} (1 + R_{i,X2})^{E_{X2}/\log 2} \dots], \quad (2.2)$$

$I_i'$  (equation 2.2) gives the enhanced index,  $E_X = \Delta[X/H]$  gives the change in the abundance of element  $X$ , and  $R_{i,X}$  is the fractional change in the  $i^{\text{th}}$  index when the abundance of element  $X$  is doubled (given in arrays set out in Tripicco and Bell 1995). Figure 2.3 shows the enhanced  $Mg_b$  index versus the change in  $E_X$  for  $X=Mg$ . In the plot, the  $Mg_b$  solar abundance ratio is for a 13 Gyr SSP, taken from Vazdekis et al. (1999). The plot serves as an example of how other indices behave also, since they obey the same equation but differ by the constants  $I_i$  and  $R_{i,X}$ .

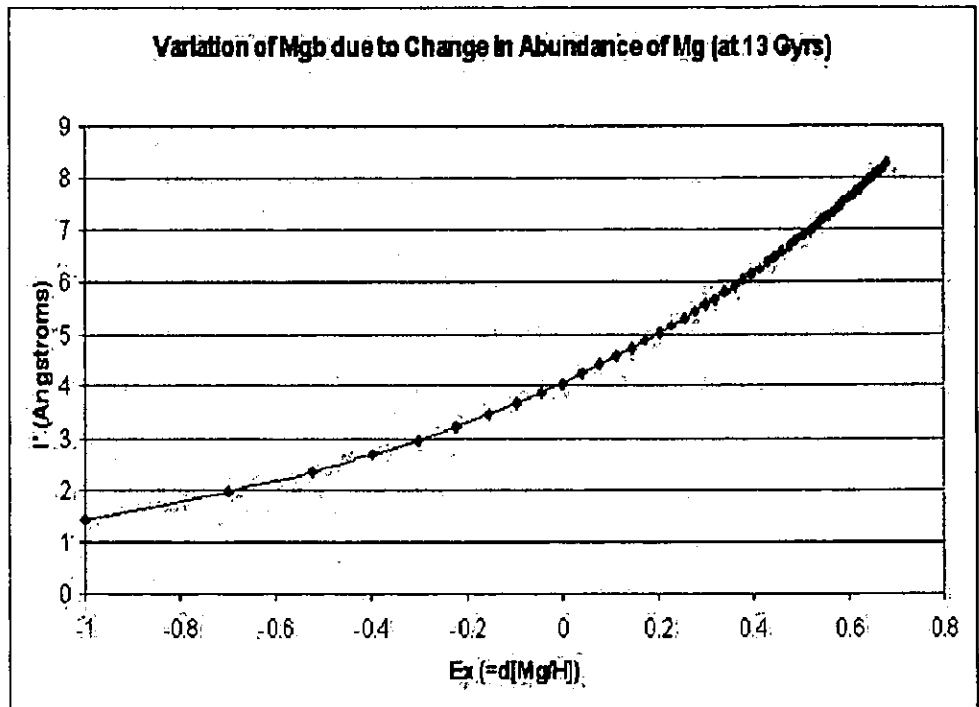


Figure 2.3: Predicted variation of Line Strength of  $Mg_b$  from its solar abundance ratio value (shown at  $E_x=0$ ) as Mg abundance changes. As the Mg abundance increases, the line strength of  $Mg_b$  climbs steeply, as according to the equation for  $I_i$  above.

## 2.2 Mass Loss

Delayed feedback is a term that refers to that mass loss of stars occurring largely at the end of stellar life times which is delayed, due the size of the model time step, from being fed back into the model ISM. Delayed feedback therefore has an effect on how the GCE model handles mass loss for those stars of shorter life span than the step size of the GCE model. Mass loss can be considered to be instantaneous at the end of the MS for a HMS, provided time steps in GCE models are of an order of magnitude greater than  $1 \times 10^5$  years. This is since the  $8 M_{\odot}$  IMS, at the mass boundary between HMSs and IMSs, spend  $4.2 \times 10^5$  years in post-MS (pre-supernova) phase (Woosley, Langer and Weaver 1993). This is following a MS lifetime of  $\sim 55$  Myrs (calculation from Wood 1992, verified from Kauffman, 1988. p.

416). Mass loss from an IMS is far less than from an HMS, as shown by Lamers and Nugis 2002 who model mass loss for different mass stars through Luminous Blue Variable (LBV) and Wolf-Rayet (WR) stages. In the GCE code the pre-WD Initial Mass Final Mass Relation (IMFMR) from Wood (1992) is used. This IMFMR, developed for single star MS lifetimes, was used to compute the range of stars going SNII and the MS lifetime corresponding to the lower mass limit for SNII in the GCE code.

The rate of mass loss varies over the main sequence and in the subsequent LBV then WR stages (Woosley, Langer and Weaver 1993, Garcia-Segura, Low and Langer 1996). LBV and WR stars exist at the end of the MS (with WR possibly being off the MS). LBVs are massive, intrinsically bright and variable stars which represent a very short-lived (perhaps as little as 40,000 years) strongly mass-losing phase, during which they undergo deep erosion of the outer layers before they enter the Wolf-Rayet phase; when they undergo heavy mass loss. Wolf-Rayet stars are extremely rare, reflecting their short lifespan. Due to the short lifespan of stars in the LBV and WR stages, HMSs are reasonably assumed in the GCE model to evolve to supernovae instantaneously having left the MS.

The IMFMR from Wood (1992) was applied to a range of masses, and compared for verification purposes to tabulated MS and post-MS lifetimes; from Kauffman (1994), as shown in Table 2.3, and also Sparke and Gallagher (2001), as shown in Table 2.4, between 0.5 and 60  $M_{\odot}$ . The Wood (1992) IMFMR, which is used in the GCE code, is shown in equation 2.3:

$$M_{\text{star}} = (T_M/10.0)^{-0.4} \quad (2.3)$$

In this equation  $M_{\text{star}}$  is the initial mass of a MS star (in  $M_{\odot}$ );  $T_M$  is the MS lifetime of the star (in Gyr). In the GCE model stars of masses greater than 60  $M_{\odot}$  are rare and contribute (assuming a Salpeter IMF) relatively little to the overall stellar yields, when compared to IMSs and HMSs below this mass. The high mass stars, however, live such relatively short lifetimes on

the MS, before going supernova, that they enrich the ISM with their yields early on in the age of a galaxy (see Table 2.4).

A  $60 M_{\odot}$  star lasts only  $\sim 0.36$  Myrs on the MS, a  $25 M_{\odot} \sim 2.2$  Myrs, a  $9 M_{\odot} \sim 0.041$  Gyr, a  $5 M_{\odot} \sim 0.179$  Gyr and a  $1 M_{\odot}$  lasts  $\sim 10$  Gyr. Assuming a Salpeter IMF, the mass fraction of stars at and above  $60 M_{\odot}$  is  $\sim 0.147$ . This is a very small fraction of the mass used to form the stars in a galaxy.

The IMFMR of Wood (1992) was verified from empirical data up to at least  $25 M_{\odot}$  (see Table 2.3 which shows insignificant differences in evolutionary times for MS stellar masses  $> 1 M_{\odot}$ ). At higher masses, the empirical data from Sparke and Gallagher (2001) produced noticeably different MS lifetimes, but at this point the timescale considered is on the order of Myrs, about a tenth of the time resolution of the GCE code used in current experiments (of  $\geq 0.01$  Gyr). On this scale of time, the differences between the empirical MS lifetimes in Sparke and Gallagher (2001) and the computed MS lifetimes using the IMFMR of Wood (1992) were thought to be currently negligible.

$M_{\text{star}} (M_{\odot})$	Wood 1992 t (Gyr)	Kauffman 1994 t (Gyr)
0.5	56.569	200
0.75	20.528	15
1	10	10
1.5	3.629	3
3	0.642	0.5
15	0.011	0.015
25	0.003	0.003

Table 2.3: Comparison of times on MS for IMFMR from Wood (1992) and Kauffman (1994). Initial MS masses in the first column and MS life times in the adjacent columns. The Wood (1992) IMFMR is validated with observational data on stellar MS lifetimes from Kauffman, 1994, ed. 3, Chapter 21.

$M_{\odot}$	Wood 1992 t (Gyr)	Sparke and Gallagher 2001 t (Gyr)	t AGB (Gyr)
0.8	17.469	25	-
1	10	9.8	3.2
1.25	5.724	3.9	1.65
1.5	3.629	2.7	0.9
2	1.768	1.1	0.32
3	0.642	0.35	0.086
5	0.179	0.094	0.014
9	0.041	0.026	0.017
25	0.0032	0.0064	0.00064
40	0.000989	0.0043	0.00047
60	0.000359	0.0034	0.00043

Table 2.4: Mass dependant stellar MS lifetimes and MS to WD lifetimes. The 1st column gives initial masses on the MS, the 2nd MS to WD lifetimes from Wood (1992), the 3rd gives empirical MS lifetimes from Sparke and Gallagher (2001) page 10, Table 2.1 and 4th the Asymptotic Giant Branch (AGB, end of MS for stars less than  $\sim 9 M_{\odot}$ , pre-planetary nebulae) lifetimes - Sparke and Gallagher (2001).

### 2.3 Supernovae Ia Rates

Here are discussed results from compilations of SN observations and from theoretical predictions of SN rates from the literature. Supernovae rates remain under question (see Woosley and Weaver 1995 and also Marigo 2001). Chemical abundances provide important clues to the evolution of galaxies and these are greatly affected by supernovae (Shifields 2002). Supernova rates evolve with redshift (see below) and vary with galaxy type (Sullivan et al. 2003), as found in observations. SN rates at redshift  $< 0.05$

(i.e. within the local Universe) were examined from the literature, since this is most relevant to the galaxies studied in this thesis.

The supernovae at higher redshift, of newly forming galaxies for example, are also of interest to constrain the SFHs searched by the GCE code. Supernovae type Ia (SNIa) rates and mass limits for type II supernovae (SNII) are model inputs to the GCE code. The lower mass limit for Type II SN may be  $\geq 8 M_{\odot}$  (Regaly 2001), where the core collapse of stars greater than  $25 M_{\odot}$  (or any star with a stellar core mass greater than  $5 M_{\odot}$ ) produces a black hole (Carroll and Ostlie 1996, p. 514). Stars of MS masses less than  $25 M_{\odot}$  may result in a neutron star/ pulsar (Carroll and Ostlie 1996). In the GCE code SNII are dealt with by using the theoretical stellar yields of HMSs.

Mass loss, such as post-MS stellar winds (SWs), from IMSs and HMSs plays an important role in the cosmic cycle. IMSs are important to GCE due to their mass loss via SWs and (in close binaries) SNIa; enhancing the Z (with Carbon, lines from which may be linked to Fe lines, and Fe peak nuclides - Carroll and Ostlie 1996, p. 722) of the ISM. An example of observed SN rates (for various galaxy Hubble types) at non-cosmological redshifts from the results of Navasardyan et al. (2001), are given in Table 2.5. The values found for supernovae were converted from Supernova Units (SNU) assuming a value of  $7.4 \times 10^{10} M_{\odot}$  and calculated from a luminous mass-to-light ratio of 3.4 and B band Luminosity total ( $L_{B,tot}$ ) of  $2.3 \times 10^{10} L_{\odot}$  for the Milky Way galaxy bulge (Carroll and Ostlie 1996).

The calculation started with the rate in SNU, which is the number of SN per century per  $10^{10}$  solar luminosities in the rest-frame B band, often used for low redshift SN detections. The value in SNU was multiplied by  $10^7$  to find in terms of per Gyr (as oppose to per century), divided by  $10^{10} L_B$  (to find as a number per Gyr per B band solar luminosity,  $L_B$ ) and then divided by the mass-to-light ratio. The luminous Galaxy mass includes the bulge, thin and thick disc, and dust and gas. This resulted in rates with units of  $\text{Gyr}^{-1} M_{\odot}^{-1}$ , and is converted for tables, for ease of displaying results, to  $10^{-5}$ .

SN type	Galaxies	Paired	Error	Grouped	Error	Cappellaro et al (1999)	Error
Ia	4.12	8.53	3.24	6.47	1.76	5.88	1.76
II + Ib	8.24	19.41	9.12	10.88	5	14.12	5.59
ALL	12.35	27.94	9.41	17.35	5.29	20.00	5.88

Table 2.5: Observational SN Rates ( $\text{Gyr}^{-1} \text{M}_{\odot}^{-1} \times 10^{-5}$ ) based on studies of various galaxy types - Navasardyan et al. (2001). The 2nd column gives supernova rates for isolated galaxies, for which no errors were given; the 3rd column gives rates for paired galaxies, followed by errors in the 4th column. Finally, rates and errors for grouped galaxies and then as found by Cappellaro et al. (1999), are given.

Navasardyan et al. (2001) observed that SNIa are less common than Ib/c or II in late-type (i.e. spiral) galaxies. Data in Table 2.5 were derived from the combined archives of three SN searches, based on photographic surveys. These searches by Navasardyan et al. (2001) were cross correlated, to study isolated, paired and grouped galaxies in the local Universe (at  $z < 0.05$ ); for instance from the Garcia (1993) catalogue of nearby galaxies and Reduzzi and Rampazzo (1995) catalogue of isolated galaxies. No errors are given for the first column of Table 2.5 above, since the observations in those cases were of only one or two supernovae.

Matteucci and Recchi (2001) calculated SNIa rates in E and spiral galaxies from a number of models by different researchers. Table 2.6 presents some of the rates from these various models. Interestingly the SNIa rates in Table 2.5 compare well with the 2nd and 3rd models represented in Table 2.6.

The models in Table 2.6 (plotted in Figure 2.4) were distinguished by their different parameters, such as whether infall was allowed for in gas flow and the choice of stellar yields (e.g. RV81 for Renzini and Voli 1981 and MBC for Marigo, Bressan & Chiosi 1996). The present-time SNIa rates in the final column were compared with an observational one, for the Es and SOs, of about  $5 \text{ Gyr}^{-1} \text{M}_{\odot}^{-1} \times 10^{-5}$  given in the final row of Table 2.6. The second column indicates whether the chemical evolution model, where applied to our Galaxy, for the solar neighbourhood had one or two infall episodes. The third column shows the efficiency of star-formation “C” (i.e., the constant in

the SFR, expressed in units of  $\text{Gyr}^{-1}$ ). The constant  $C$  is given in the equation in Table 2.2, but in the models above was given only one value to adopt (unlike in the GCE model which has values  $C1$ ,  $C2$  and  $C0$ ). The fourth column gives the adopted timescale (in Gyr) for the formation of the disk in the solar region. The fifth column indicates if a threshold in the gas density for the SFR has been adopted or not. The sixth column shows the assumed prescriptions for the SNIa progenitors in the various models. The seventh column contains the values for  $A$ , the fraction of binary systems in the IMF that lead to a SNIa explosion. The eighth and ninth columns contain the IMF (Salpeter being defined in the range  $0.05\text{-}50 M_{\odot}$ ), and the  $M_i\text{-}M_{\text{WD}}$  (initial stellar mass evolved through to the white dwarf mass) relation adopted, respectively.

Mod	Inf.	$C$	$t$	Th	SNIa	$A$	IMF	$M_i\text{-}M_{\text{WD}}$	Rate1	Rate2
M1	1	0.37	5	No	KTN	0.05 WD	Salpeter	RV81	0.03	0.74
						MS,0.02				
M2	2	2,1	8	Yes	WD+R,	0.05	Scalo	RV81	0.17	5.06
					C97					
M3	1	0.5	4	No	C97	0.05	Scalo	RV81	0.19	5.68
M4	1	0.5	4	No	G96	0.05	Scalo	I91	0.04	1.15
M5	1	0.5	4	No	G96	0.05	Scalo	MBC	0.02	0.68
OBS.									0.18	5.29

Table 2.6: Model Parameters and Predicted SNIa Rates from Matteucci and Recchi (2001) in  $\text{SNu}$  (Rate 1) and then  $\text{Gyr}^{-1} M_{\odot}^{-1} \times 10^{-5}$  (Rate 2). Model 2 is the best fit model to observations (Matteucci and Recchi 2001). A luminous Galaxy mass of  $7.9 \times 10^{10} M_{\odot}$  was assumed (Carroll and Ostlie 1996, Table 22.1 and p. 933). The observed rate (OBS.) of “5.29” is of SNIa in E-SO galaxies from Cappellaro et al. (1999), with  $H_0$  of  $75 \text{ km s}^{-1} \text{ Mpc}^{-1}$ . This OBS. rate differs from the value of 5.88 formulated by Navasardyan et al. in Table 2.5. The difference is due to (it seems) rounding errors made by those authors when converting units; Cappellaro et al. had used a  $H_0$  of  $60 \text{ km s}^{-1} \text{ Mpc}^{-1}$  to find their intrinsic SNIa rates, and Navasardyan et al. had  $H_0$  of  $75 \text{ km s}^{-1} \text{ Mpc}^{-1}$  for their intrinsic SNIa rates.

In table 2.6, models assume an upper limit of  $50 M_{\odot}$  for the mass of MS stars whose yields may affect the SNIa rate, as oppose to the usual Salpeter upper limit value of  $120 M_{\odot}$  (Salpeter 1955). The last two columns have units of  $\times 10^{-5} \text{ Gyr}^{-1} M_{\odot}^{-1}$ . The yields adopted in most of the models were the same: Renzini and Voli (1981) for low and intermediate-mass stars and Woosley and Weaver (1995) for massive stars. These stellar yields are also currently used in the GCE code.

Matteucci and Recchi (2001) showed that the peak in the SNIa rate in a newly formed galaxy was at  $\sim 1 \text{ Gyr}$ . Matteucci and Recchi (2001) claim this 1 Gyr was just the time at which, in the solar neighbourhood, the Fe production from SNIa started to become important and not the time at which SNIa started to explode. In other research (Samland 1998), modelling SNIa rates in the MW Galaxy, SNIa rates as high as  $11.83 \text{ Gyr}^{-1} M_{\odot}^{-1} \times 10^{-5}$  were found.

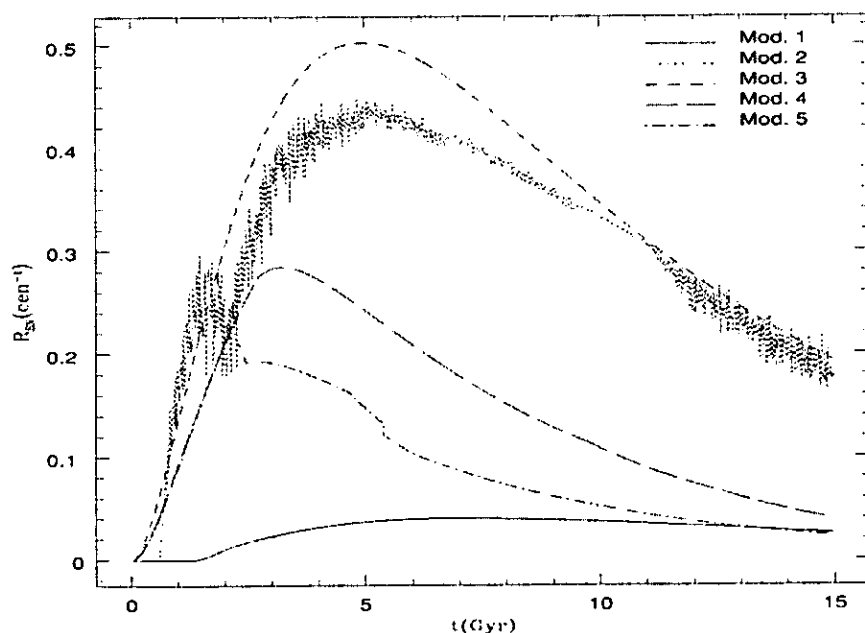


Figure 2.4: Supernovae rate variation over time, for an instantaneous burst of star-formation. Model 5 is for the rate predicted for an elliptical galaxy. Model 2 assumes a threshold in the gas density for the star formation. From Matteucci and Recchi (2001), their Figure 4. For models, refer to Table 2.6. Model 2 can be seen to have a great rate of variation.

In summary, SNIa, which dominate supernovae events in early-type galaxies, appear in models and observations to have a similar rate of between about 4 (Navasardyan et al., 2001) and  $12 \text{ Gyr}^{-1} M_{\odot}^{-1} \times 10^{-5}$  (Samland 1998). This range encompasses the best fit from models shown in Table 2.6. The SNIa rate was varied in experiments with the GCE model, based on these rates from the literature.

Three SNIa rates were tried, spanning the range supported by the literature; 3.8 (a lower limit, from Sansom and Proctor 1998, who derived this value from models of Timmes, Woosley and Weaver (1995), assuming a galaxy mass of  $1.4 \times 10^{11} M_{\odot}$ ), 6.5 (from the best fit for NGC 2831) and 12 (from Samland 1998, as an upper limit), all with the units of  $\times 10^{-5} M_{\odot}^{-1} \text{ Gyr}^{-1}$ . The main outcomes of these experiments of SNIa rate modelling with a sample galaxy are given in section 2.4.

## 2.4 Sample Galaxy NGC 2831

The sample galaxy was chosen for the purpose of experimenting with the limits of the model input parameters (for example flowrates) and to test, for example, SNIa rates. NGC 2831 was chosen as a sample galaxy from the data set described in subsection 2.10.1. NGC 2831 was selected due to the principal reasoning that compared to most galaxies in the WHT data set, NGC 2831 had relatively good SSP reduced chi-squared ( $\chi^2_{\nu}$ ) of 2.35. Other reasons besides these principal reasons for NGC 2831 being chosen were:

- NGC 2831 is an E galaxy, useful to test single zone GCE models, as a spheroidal galaxy with a centralized distribution of SF, which is relatively simple to model compared to that of spiral galaxies.
- NGC 2831 is not a strong emission line galaxy (PS02).

- The individual line strengths of NGC 2831 contributed evenly in the overall statistical fit of the galaxy to SSP models. This meant that the fit was not being unbalanced by any single line strength; a single line with very poor chi-squared ( $\chi^2$ ) did not make the overall fit appear significantly worse than the other indices alone did.
- There exists good S/N data, for 19 optical line-strengths, for this galaxy (PS02).

However, NGC 2831 (like the cD galaxy nearest to NGC2831, NGC 2832) was at such a redshift that a coincidence with telluric lines, originating from the Earth's atmosphere, reduced the number of indices that could be fitted to 19 from 20. Furthermore, NGC 2831 and NGC 2832, following the experiments described in this Chapter, upon inspection of their optical images appeared to not be isolated but close and possibly interacting. In Figure 2.5 NGC 2831 is shown with the larger cD galaxy, NGC 2832.

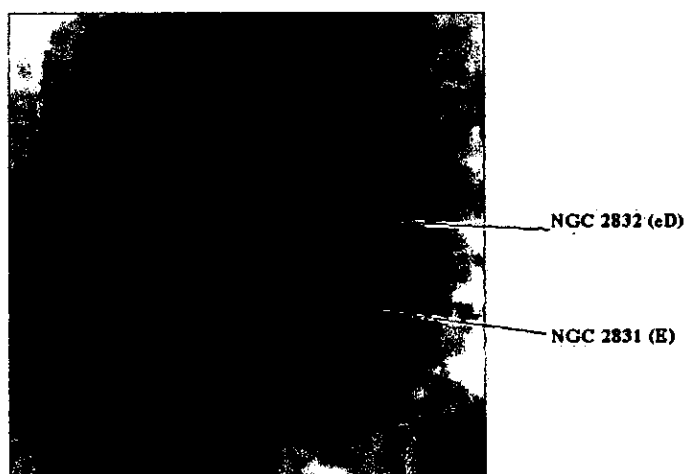


Figure 2.5: The E galaxy NGC 2831 is shown with the larger cD galaxy, NGC 2832. NGC 2832 is center and NGC 2831 the spheroidal is below to the right, in this image of 1.5 by 1.5 arcminutes. DSS image from Hypercat archive (<http://www-obs.univ-lyon1.fr/hypercat>), with colours inverted.

Various experiments with the sample galaxy were performed. Firstly, there were those regarding the SNIa rates from the literature review (see Table 2.7). There were then those experiments performed with solar versus non-solar abundance ratios (more fully investigated in section 2.8). There were also GCE model runs completed to test the effects of tripling the error on one index with an error value (for Ca4227). This testing was done since the error value for Ca4227 had been put into doubt (as having been significantly underestimated in PS02). This doubt arose from finding Ca4227 was particularly poorly fitted by GCE model runs. Following this, notes made in PS02 regarding a suspected underestimation of error for Ca4227 were identified. A significantly underestimated error value may cause an effectively incorrect  $\chi^2$  in the best fit.

The best fit on NGC 2831 was achieved with non-solar abundance ratios, tripled error for Ca4227, and a low but non-zero SNIa rate (of about  $4 \times 10^{-5} \text{ Gyr}^{-1} \text{ M}_{\odot}^{-1}$ ) which is within the observational limits found in the literature review. The hard limits set by the (theoretical) supernovae data sets which the GCE model drew upon were explored in these trials (see Table 2.7), for experimental completeness. This had little effect on the best fit for NGC 2831.

The model input values and results for this best fit are given in the model summary (see section 2.9), and were presented as part of a poster presentation at the National Astronomical Meeting 2003, held in Dublin and also at the SPS03 in Garching. The results of some different SNIa rates (between  $\sim 4$  and  $12 \times 10^{-5} \text{ Gyr}^{-1} \text{ M}_{\odot}^{-1}$ ) are given in Table 2.7, with that of zero as a control (to test the importance of having no SNIa at all). The table shows that varying the SNIa rate had little effect on the  $\chi^2_{\nu}$ , though for this sample galaxy lower rates produced the lowest  $\chi^2_{\nu}$ ; with the exception of a SNIa rate of 0, which produced the poorest fit of all. Here  $\nu$  is the number of degrees of freedom, defined for the  $\chi^2_{\nu}$  formulae as the number of fitted observations (i.e. 20 or 19 Lick indices) less the number of model parameters searched in parameter space (i.e. C1, T1, D1 and F1 in the GCE multi-stepping software). A  $\nu$  of 15 in the  $\chi^2$  occurs where there were 19

indices fitted with the 4 searched model parameters of the GCE model multi-step code.

Rate (SNIa)	T1 (Gyr)	C1 (Gyr <sup>-1</sup> )	{F1 (M <sub>⊙</sub> Gyr <sup>-1</sup> )	T2 (Gyr)	χ <sup>2</sup> <sub>v</sub>
0	1	0.2	1.00E+07	6.58	9.45
3.8	5	0.2	1.00E+07	6.58	5.72
6.5	4	0.4	1.00E+07	4.864	6.3
8	3	0.2	1.00E+07	3.864	6.15
12	3	0.2	1.00E+07	3.864	6.23

Table 2.7: NGC 2831 best fit model parameters for various SNIa rates, including that of zero as a control. In χ<sup>2</sup><sub>v</sub>, v, which is the degrees of freedom, equals 15. Fixed model input parameters were: C0=2, C2=0.03, F0 and F2 zero and non-solar abundance ratios; that is a initially high SFR, with no significant inflow or outflow of gas, and a low end SFR.

Interestingly, in Table 2.7, as the SNIa rate is increased a pattern in the best fit model parameters emerges. The values for C1 and F1 do not much change, but those of T1 and T2 become earlier as the SNIa rate is increased. What this indicates, is that the higher end SNIa rates require starburst events to take place earlier in the age of a galaxy. A simple reason for this would be that were the higher end SNIa rates to be present at a later time, galaxies would require different line strengths (e.g. due to more Fe from SNIa) to the ones that they do have. Another way of interpreting this result is to realise that knowing alone the SNIa rate accurately for a given galaxy may help unravel more confidently the SFH.

## 2.5 Pseudo Galaxies

In this section, experiments on simulated data are described. These were run as control experiments to test the validity of using the GCE code and the robustness of the GCE code in reproducing SFHs.

## 2.5.1 Test for a Perfect Match

The best fit ( $\chi^2_v = 5.72$ ) SFH found for NGC 2831 by the GCE software was used to mimic a "pseudo" galaxy (for which the SFH is exactly known, see near top of Table 2.7 for parameter values). A run of the GCE multi-step code with such a pseudo galaxy should produce a perfect fit of model versus "data" (i.e. of a pseudo galaxy). This is since the values are on a grid point in searched parameter space. The pseudo galaxy consists of the Lick indices output by the model. The GCE model, using the pseudo galaxy, was able to fully recover the SFH model input parameters originally found for NGC 2831. Indices recovered were also as for the original modelled NGC 2831. Further, the model achieved a  $\chi^2$  of  $4.1 \times 10^{-6}$ , which is essentially zero, within the rounding errors of the software.

## 2.5.2 The Perturbed Case

Three perturbed pseudo galaxies were created (using the single model GCE code), by moving all model input parameters (i.e. model parameters given in the first half of Table 2.7) outward in parameter grid space between adjacent grid points and then running the GCE multi-step code to output best fit SFH values for each perturbed pseudo galaxy in individual experiments.

Perturbing all the pseudo galaxy model parameters by 10 % of the space between the grid point original values and the adjacent grid point caused an increase in  $\chi^2_v$  of  $\sim 0.114$ . For a 20 % perturbation of all model input parameters  $\chi^2_v$  increased by  $\sim 0.456$  (see Table 2.8). Perturbing all the model parameters between grid points in parameter space by 50 % (i.e. to mid way between grid points) caused an increase in  $\chi^2_v$  of  $\sim 2.128$ , whilst the original unperturbed SFH model parameters were fully recovered once more. Since the perturbed flowrate was moved inward within grid space in this third experiment, this experiment served as a control and showed that a systematic effect of the model to find the lower values in grid space was not apparent. However, this increase in  $\chi^2_v$  due to a 50% perturbation implies that the grid spacing is too coarse. In all three experiments, the unperturbed model parameters were recovered by the best fits, thereby increasing

confidence in the GCE code. However, line strengths deviated slightly, as discussed below. The fixed model parameters should fully define the line strengths (as they did for the pseudo galaxy). However, the indices produced by the perturbed pseudo galaxies were not, being perturbed, from the original fixed model parameters.

Experiment	10 % Perturbed	20 % Perturbed	50 % Perturbed
$\chi^2$	0.114	0.456	2.128

Table 2.8: Perturbed Pseudo Galaxy Runs best fit  $\chi^2$ .

Index and units	Pseudo Galaxy Index (I)	10 % Perturbation $\Delta I$	20 % Perturbation $\Delta I$	50 % Perturbation $\Delta I$
H $\delta_A$ (Å)	-2.855	0.003	0.025	0.028
H $\delta_F$ (Å)	0.021	-0.244	-0.463	-0.089
CN1 (mag)	0.035	-0.026	0.003	-0.092
CN2(mag)	0.078	-0.006	0.004	-0.019
Ca4227 (Å)	2.012	0.007	0.023	0.04
G4300 (Å)	5.841	-0.002	-0.001	-0.006
H $\gamma_A$ (Å)	-6.089	0.002	0.013	0.016
H $\gamma_F$ (Å)	-1.406	0.006	0.032	0.045
Fe4383 (Å)	4.947	0.003	0.014	0.02
Ca4455 (Å)	1.912	-0.001	0.005	0.001
Fe4531 (Å)	3.285	0.001	0.008	0.009
Fe4668 (Å)	6.359	-0.008	-0.01	-0.036
H $\beta$ (Å)	1.793	-0.004	-0.013	-0.024
Fe5015 (Å)	5.718	0	0.006	0.004
Mg $_1$ (mag)	0.13	-0.004	-0.002	-0.014
Mg $_2$ (mag)	0.27	-0.001	0.004	-0.001
Mg $_b$ (Å)	4.298	-0.003	0.001	-0.008
Fe5270 (Å)	2.96	0.003	0.01	0.014
Fe5335 (Å)	2.639	0.005	0.017	0.029

Table 2.9: Pseudo line strengths and changes in pseudo line strengths. Sample original pseudo galaxy line strengths are shown, with their deviations (to 3.s.f.) in the three perturbation experiments, with negative signs indicating decreases.

As shown in Table 2.9, the line strengths were only slightly perturbed. Almost all indices differed in the three perturbation experiments by amounts of less than 2 % of the original pseudo galaxy line strengths. The exceptions

were  $H\delta F$ , for the 10 and 20 % perturbations, and CN1 for the 10 % perturbation. Why the values for  $H\delta F$  and CN1 varied so much is uncertain. However the error for CN1 is very high in relation to the observed index in comparison to the other indices and their respective errors. The line strengths seemed perturbed, but not in any systematic way related to the degree of perturbation. The recovery of the unperturbed model parameters was as expected; The GCE code is designed to find the best fit model to the data from a set of fixed models. Any recovered SFH values will lie on one of the grid points in searched parameter space, regardless of the degree of perturbation (up to 50 %). The deviations found give errors to axes denoting line strengths (in plots versus Z, age and so forth) For  $H\delta F$ , CN1 and CN2 in particular, there are potentially significant model errors. However, the indices of the unperturbed pseudo galaxy were error free, suggesting the GCE model may accurately reproduce line strengths; provided the model input parameters fall onto grid points within parameter space. The importance of searching parameter space on a sufficiently fine grid is highlighted by this final result.

## 2.6 Testing Small Time Step (DT)

The amount of time used to run the GCE model increases as the time step size is decreased. Small time steps may be favourable at certain points in a model galaxy SFH (for example at a time of high SFR) and unnecessary at other times in the model SFH (i.e. at a time of low SFR). Therefore a variable time step was thought a useful modification to the GCE code, so as to obtain the most efficiency out of the computing time needed to run the GCE code. These modifications were carried out by Dr. A. Sansom. With the GCE code modified to handle delayed feedback, tests of small time steps were completed. The availability of the code to access small times steps where needed, though making minor improvement to computation time, did not significantly improve fits of model versus data.

## **2.7 Comparing Fineness of Parameter Space Searches by SSP and GCE Models**

Adding parameters to models, to extend them from relatively simple SSP models to self-consistent GCE models, has thus far yielded poorer best fits in GCE models. A possible reason for this is that SSP models (Proctor, R., 2002) make a much finer search of parameter space, albeit with fewer parameters (Sansom, A., private communication, 2002).

Searching more discrete values of variable model input parameters (T1, C1, F1 and D1) could improve GCE model versus data fits. Currently, the SSP software (Proctor, R., 2002) searches 85 discrete steps of age to select SSPs from the arrays of Vazdekis et al. 1999 with adjustments from Tripicco and Bell 1995. The software also searches 81 of Z and steps through 37 possible enhancements (i.e. 37 enhancements to produce abundances different than solar abundance). This produces a search of 254745 possible combinations of age (from 1.5 to 16.8 Gyr), Z (0.01 to 5.6 times solar) and enhancement (about 0.5 to 4 times solar abundance). From the recent WMAP results, the age range used is to be updated in the code to 13.7 Gyr, but versions of the SSP and GCE models used here were up to the age 17 Gyr. Currently, the GCE model only searches about 1.7 % of this size of parameter space (4320); from 15 discrete variables for T1, 4 for C1, 6 for F1 and 12 for D1 being tried in a run of the multi-step GCE code (see Table 2.1 and Figure 2.2 for definitions of these searched parameters describing the SFH). Careful experiments with pseudo galaxies to test the effect of perturbing individual model parameters may be considered. These could act as a guide to which model parameters to first increase the number of searched discrete model parameters in the GCE code for. Such experiments will need to consider different SFHs. For example, in the GCE model C1 is more important to the chemical evolution of a model galaxy for a T1 of 8 Gyr than a T1 of 16 Gyr, since it plays a role in the SFH for a

greater duration of the SFH. Therefore, for example, testing C1 and F1 should be done at low value for T1.

## **2.8 Comparing Solar versus Non-solar Abundance Ratios**

Abundances of elements in the ISM from which stars are born play an important role in GCE, since this ultimately affects the spectra of stars that compose the light of galaxies and, further, affects the stellar yields of the stars. Initial studies of GCE used solar abundance ratios (from studies of the Sun's photospheric spectra). Wallerstein (1962) and Wallerstein et al. (1963) were the first to find conclusive evidence of a non-solar mixture of Fe-peak elements (from G type field stars in the 1962 paper and in the 1963 paper three field stars resembling giant, metal-poor globular cluster stars). Wallerstein (1962) and Wallerstein et al. (1963) thereby on observational grounds greatly extended the complexity of GCE research. Modern GCE research, theoretical and observational, often involves non-solar abundance ratios (see Trager et al 2000, PS02 and Marmol-Queralto et al., 2006). The SSPs used by the GCE model are those of Vazdekis et al. (1999) and Worthey et al. (1994), as detailed in PS02. Non-solar abundance ratios were estimated by the GCE model, by way of enhancements to solar abundance ratio SSPs (Proctor 2002), as discussed above in section 2.1. In this section, experiments were made so as to compare the  $\chi^2$  contour plots and indices produced by runs of the GCE model. This was with the mid SNIa rate of 6.5 and appropriate best fit parameters from Table 2.7.  $\chi^2_{\nu}$  for the solar abundance ratio case was about 6, only 0.6 higher than for the case allowing for non-solar abundance ratios.

## 2.8.1 Contour Plots and Output Indices

Contour plots provide a graphical means of interpreting the spread of  $\chi^2$  (within 3 sigma of the best fit) resulting from a run of the multi-stepping GCE code. The contour plots provide aid to determine if the best fits from a model run are well confined in parameter space and further which discrete values for searched model input parameters are most often identified (or avoided) by model outputs. Contour plots in this section are generated as a composite of individual contour plots, each in a square grid containing points of model galaxies with  $\chi^2$  within 3 sigma of the best fit (each of these fitted SFHs is represented by a single point on the contour plot). Each individual square grid has a horizontal axis of T1 and vertical axis of D1 (see Table 2.1 for a description of T1, D1 and other model input parameters), and each box represents a discrete, searched value of either C1 (horizontal axis) or F1 (vertical axis); so for example, the first square grid in the top left hand corner of a contour plot represents the first, and lowest, searched values of C1 and F1, with any point placed in that square representing a model galaxy with T1 and D1 at the loci of that point.

The output indices from the best fits on a sample galaxy, NGC 2831 (see section 2.4) using solar and non-solar ratio models (see Table 2.10) were examined. The comparison was made so as to begin to investigate what trends the solar and non-solar abundance ratios may produce.

For the non-solar ratio models, the contour plots showed a sharp and deep drop in  $\chi^2$  for a small region of  $\chi^2$  space, whereas the solar ratio models have a broader, less confined, distribution of dips in  $\chi^2$  for the same confidence levels above the best fit. This result indicates that the GCE model can distinguish between solar and non-solar ratio models, since the distribution of  $\chi^2$  in the plots finds different favoured points in parameter space and (as mentioned above) different types of distribution. Further, non-solar ratio models may more convincingly produce SFHs than do solar ratio models, because the SFHs are more confined.

Index and units	NS MODEL	S MODEL	S-NS MODEL	NS $\chi^2$	S $\chi^2$	
CN1 (mag)	0.022	0.054	0.032	1.57	0.08	
CN2 (mag)	0.072	0.09	0.018	1.2	0.2	
Ca4227(Angstroms)	1.982	1.695	-0.287	18.15	10.29	
G4300 (Angstroms)	5.814	5.374	-0.44	0.55	0	
Fe4383 (Angstroms)	4.894	5.997	1.103	0.1	1.03	
Ca4455 (Angstroms)	1.855	1.826	-0.029	0.77	0.78	
Fe4531 (Angstroms)	3.22	3.675	0.455	0.69	0	
Fe4668 (Angstroms)	6.202	6.557	0.355	11.05	1.58	
Hb (Angstroms)	1.772	1.636	-0.136	2.46	0.54	
Fe5015 (Angstroms)	5.594	5.851	0.257	0.04	2.83	
Mg <sub>1</sub> (mag)	0.13	0.128	-0.002	9.83	9.37	
Mg <sub>2</sub> (mag)	0.27	0.279	0.009	12.3	0.53	
Mg <sub>b</sub> (Angstroms)	4.146	4.127	-0.019	4	3.44	
Fe5270 (Angstroms)	2.932	3.252	0.32	7.56	35.32	
Fe5335 (Angstroms)	2.628	3.134	0.506	0.22	14.23	
H $\delta_A$ (Angstroms)	-2.726	-2.912	-0.186	7.51	9.41	
H $\gamma_A$ (Angstroms)	-5.968	-6.19	-0.222	9.81	11.37	
H $\delta_F$ (Angstroms)	0.065	-0.022	-0.087	5.34	7.92	
H $\gamma_F$ (Angstroms)	-1.37	-1.488	-0.118	1.38	1.71	
				Total $\chi^2$ :	94.56	96.4
				Total $\chi^2_v$ :	5.91	6.03

Table 2.10: Differences in line strengths between solar and non-solar abundance ratio best fits, for NGC 2831. SNIa rates are of  $6.5 \times 10^{-5} \text{ Gyr}^{-1} \text{ M}_\odot^{-1}$ , C0 of 2 and C2 of 0.03. Columns described in text below.

In Table 2.10 the 1st column gives the names of indices and their units. The 2nd and 3rd columns give the fitted line strengths for Non-Solar Ratio

(NS) and Solar Ratio (S) abundances respectively. The fourth column of Table 2.10 gives the difference in line strength between NS and S, with negative indicating a lesser line strength in the S case than the NS case. The last two columns give individual  $\chi^2$  for indices, for the NS and S cases, for comparative purposes. The H $\delta$ , H $\gamma$  and Ca triplet (near infra-red) lines in Table 2.10 are excluded, since these are not altered from solar abundance ratios in the non-solar abundance ratio model run.

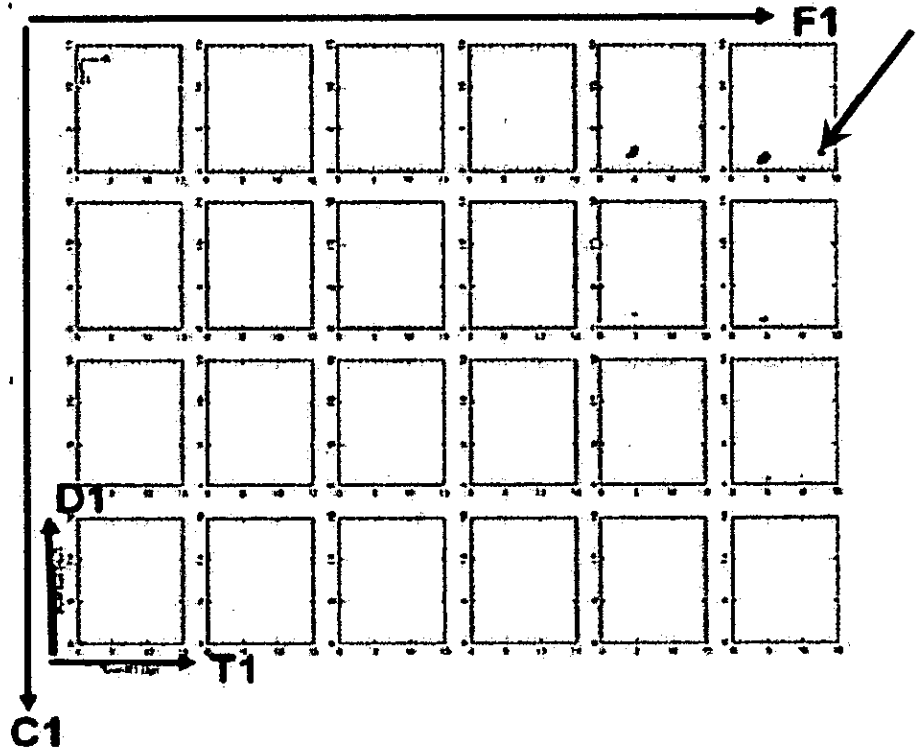


Figure 2.6a: Example contour plot of non-solar model run on sample galaxy NGC 2831, with SNIa rate of  $6.5 \times 10^{-5} \text{ Gyr}^{-1} \text{ M}_{\odot}^{-1}$ , C0 of 2, C2 of 0.03. The best fit is located in the top right of the plot, as in Figure 2.6b. The best fit is indicated by a red dot and green arrow. Each contour plot box has its vertical (time step, D1) and horizontal (T1) axis scaled from 0 to 15 Gyr. C1 is advanced in discrete values searched moving vertically down the plots. F1 is advance moving horizontally from left to right.

In the case of NGC 2831 a slightly lower  $\chi^2$  resulting from a non-solar abundance ratio also made the corresponding SFH more convincing than in the solar abundance ratio model. The unbroken lines represented by the contours about the minima in the contour plots indicate that further minima within 3 sigma of the

minimum best fit  $\chi^2$  are not present. The results of this experiment were later used to design experiments on the full WHT data set (see section 2.10). In regard to the Fe output indices, the values in Table 2.10 do appear to distinguish a pattern in differences between the solar and non-solar model, from variation in model line strengths or  $\chi^2$ . The Fe indices are systematically lower for non-solar than solar fits (see Table 2.10). This finding may suggest, for example, that galaxies with close to solar abundances have undergone more SNIa events than the E galaxy NGC 2831. It could be that as the GCE model develops and improves in the future, more patterns in differences will become apparent.

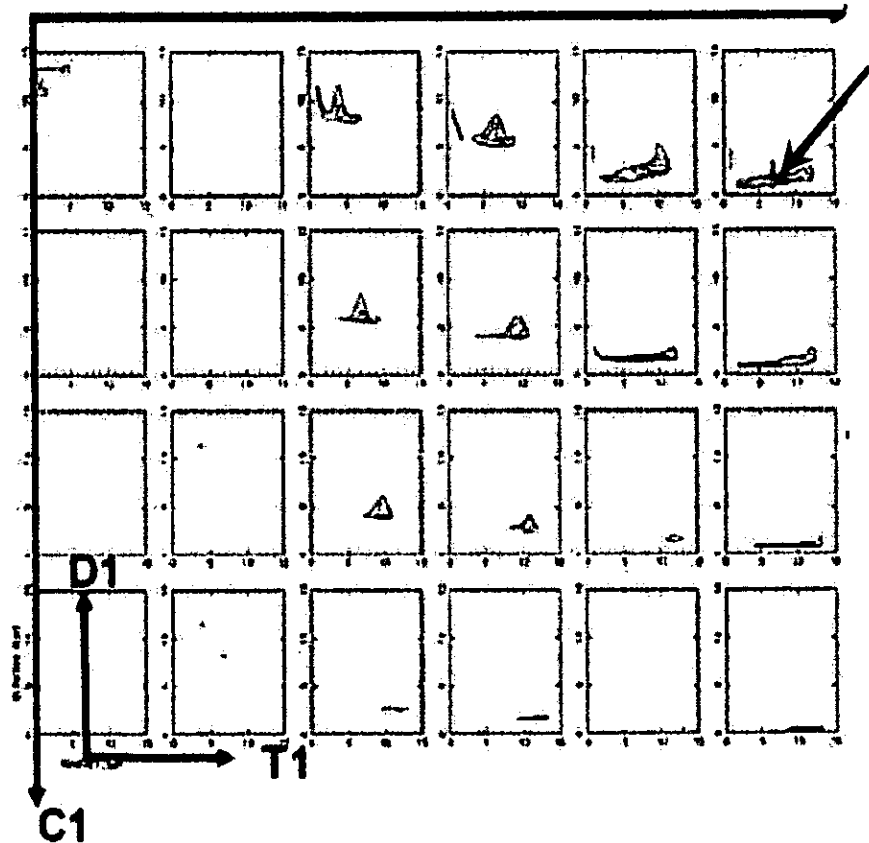


Figure 2.6b: Example contour plots of solar ratio model run on sample galaxy NGC 2831. Axes and identification of location of best fit are as described in the caption for Figure 2.6a.

## 2.9 Summary of Experiments on Sample Galaxy

The previous Sections of this chapter describe findings on experiments involving a sample galaxy. The effects of delayed feedback and studied SN rates were discussed, the choice of NGC 2831 as a sample galaxy was justified. Comparison of solar versus non-solar abundance ratios and testing of the GCE model with pseudo sample galaxies were described. The best fit for the sample galaxy so far is given in the second row of Table 2.7. The findings of the experiments on the sample galaxy are summarized here:

- The contour plots showed that the GCE code appears to constrain the SFH when non-solar abundance ratios are allowed for, far more than in the case of solar ratios.
- A high inflow rate was found in all best fits, implying perhaps that starburst inducing merger events are important (Mihos & Hernquist 1996).
- Variation of the SNIa rate, within observational limits, had little effect on  $\chi^2$  (see Table 2.7). The  $\chi^2_{\nu}$  varied by no more than  $\sim 0.5$ . Additionally, zero SNIa rate produced much poorer fits.
- The pseudo galaxy experiment demonstrated the GCE model can reproduce model parameters for a pseudo galaxy. The error in this result is negligible, the  $\chi^2$  produced being almost the theoretical value of zero (i.e.  $4.1 \times 10^{-6}$ ).
- Displacing model parameters for a pseudo galaxy by 10, 20 or 50 % of the space between sampled values does not prevent recovery of the original pseudo galaxy parameters, but fitted line strengths are slightly perturbed (in an apparently unsystematic manner).

- One reason for the apparent continued relevant “success” of SSP model fits compared to that of GCE appears to be the difference in fineness of parameter space searched by the two methods.

The experiments with the sample galaxy yielded a quite poor best fit  $\chi^2_v$  of 5.72 (compared to an SSP  $\chi^2_v$  for the same galaxy of 5.01). This suggests that the GCE model, as with the SSP model, does not yet adequately fit the SFH. The sample galaxy's best fit (see values in Table 2.7) is next used to provide a starting point for initial experiments on the larger WHT data set.

## 2.10 All Galaxies

The best fit model parameters (see Table 2.7) for the sample galaxy were used as a “starting point” for experiments with the WHT data set. The WHT data set is discussed more fully in section 2.10.1. There were 20 modelled indices for each galaxy, except NGC 2831 and NGC 2832 (19 indices, see subsection 2.10.1). To run the experiments efficiently, a shell script (written on the Redhat Linux system) was coded to systematically create all formatted input data files of individual galaxies for the multi-step GCE code to read and also to systematically run the GCE code and store output files. In this way, experiments that run the GCE code on large samples could be automated for this and future experiments.

In the experiments described below, the best fit GCE model  $\chi^2_v$  found for each galaxy of the experiments described in this Chapter were compared with their corresponding best fit enhanced (Proctor, 2002) SSP model  $\chi^2_v$ . In both the SSP and GCE model, 20 indices were to be fit for each galaxy in the WHT data set except NGC 2831 and NGC 2832 (for which there were only 19).

The SSP model had age,  $Z$  and enhancement to fit, producing a  $v$  of 17 or 16. The GCE model had 4 parameters (C0, C1, F1 and T1) to fit, producing a  $v$  of 16 or else 15. Observed average counts from the WHT data were

found using Starlink data reduction software (i.e. KAPPA), to help identify those galaxies with high or low S/N; If the error values of indices are too great, the data fails to distinguish between different models. From comparisons of SSP and GCE best fits, NGC 5353 (an S0), and some Sb galaxies, NGC 3769, NGC 4157 and NGC 4217 were considered for future exclusion from analyses. This was since each was found to have been effectively fit by its SSP best fit (achieving  $\chi^2_v$  of 0.87, 0.54, 0.66 and 0.25 respectively, calculated from SSP  $\chi^2$  values in Table 2.11).

Most of the Es and SOs had  $\chi^2_v > 2$ , so may have scope for GCE fitting that may lead to  $\chi^2_v$  better than that achieved with SSP fits. The following subsections discuss the experiments with supernova rate and abundance ratios that were first tried with the sample galaxy NGC 2831.

### **2.10.1 Observed Galaxies: existing data**

The WHT data set provided by PS02, used for experiments using the GCE model, is discussed here. This sample consisted of 32 spheroidal and spiral (S) galaxies of the local Universe, observed with the WHT, and referred to in this report as the "WHT data". Observations of spirals concentrated upon the bulges of those galaxies. These galaxy observations produced spectra, from which 24 Lick indices were measured (PS02). The errors that were calculated in the reduction of the raw data are important in the statistical calculation of  $\chi^2$ ; for example errors that are too large lead to degeneracy in the data, as models can then too easily fit the data.

### **2.10.2 Variation of Supernovae rate**

Experiments with different supernovae Ia rates on sample galaxy NGC 2831 had not much differed in the resultant  $\chi^2_v$  for the sample galaxy (see Table 2.11). This result was unexpected, since supernovae form such a distinct part of the cosmic cycle. Therefore the SNIa rate was chosen first to experiment upon all 32 galaxies in the WHT data, so as to investigate

further this unexpected result. Three SNIa rates were tried, as done with the sample galaxy.

Apart from the SNIa rate and the four fitted parameters, all other model input parameters were kept constant, with non-solar abundance ratios in effect. The results of varied SNIa rates on GCE model best fits of all 32 galaxies in the WHT data are outlined in Table 2.11.

Type	(NGC)	SSP $\chi^2$	SN3.8 GCE $\chi^2$	SN6.5 GCE $\chi^2$	< SN3.8?	SN12 GCE $\chi^2$	< SN3.8?	< SN6.5?
E	2831	44.88	85.88	94.53	0	93.42	0	1
E	3226	118.1	180.58	185.5	0	171.2	1	1
E	3608	50.43	182.52	153.08	1	176.32	1	0
E	4291	49.97	105.92	105.86	1	119.76	0	0
E	4365	55.77	239.62	211.96	1	173.06	1	1
E	4374	51.82	129.18	126.84	1	137.74	0	0
E	4552	92.57	382.46	297.92	1	305.68	1	0
E	4636	27.82	141.14	110	1	123.22	1	0
E	5322	21.42	106.92	87.84	1	90.96	1	0
E	4697	32.46	183.3	138.96	1	108.2	1	1
E(cD)	2832	80.15	183.58	150.1	1	171.55	1	0
Mean:		56.85	174.65	166.26	9 Of 11	151.92	8 Of 11	4 Of 11
S0	2549	45.74	417.44	301.16	1	259.18	1	1
S0	3607	30.76	202.62	178.48	1	139.1	1	1
S0	4203	71.53	250.84	203.3	1	220.86	1	0
S0	4526	84.72	255.32	201.98	1	170.52	1	1
S0	5354	28.63	58.86	54.72	1	66.48	0	0
S0	5353	14.78	241.2	195.68	1	181.34	1	1
S0a	3301	59.4	252.66	311.34	0	309.44	0	1
Mean:		47.94	239.85	206.67	6 Of 7	192.42	5 Of 7	5 Of 7

Sa	3623	24.05	137.86	101.38	1	92.74	1	1
Sa	4419	66.88	206.66	229.8	0	245.76	0	0
Sab	4192	31.88	158.02	159.6	0	183.2	0	0
Sab	4312	18.42	61.02	57.98	1	54.68	1	1
Sab	4313	30.35	197.4	238.78	0	246.28	0	0
Mean:	34.32	152.19	157.51	2 of 5	164.53	2 of 5	2 of 5	
Sb	2683	32.6	77.04	87.06	0	93.04	0	0
Sb	3769	9.2	197.02	188.74	1	180.42	1	1
Sb	4157	11.29	60.14	59.8	1	61.04	0	0
Sb	4216	46.41	463.72	360.42	1	273.7	1	1
Sb	4217	4.18	10.34	10.56	0	11.64	0	0
Sb	5746	34.39	94.46	81.64	1	76.94	1	1
Sb	5908	36.41	96.68	113.18	0	121.32	0	0
Sb	5987	27.44	110.46	99.72	1	95.96	1	1
Sbc	3254	35.75	165	141.65	0	212.16	0	0
Mean:	26.41	141.65	126.97	5 of 9	125.14	4 of 9	4 of 9	
T Mean:	41.38	177.08	164.35	22 of 32	158.50	19 of 32	15 of 32	

Table 2.11:  $\chi^2$  for full WHT sample, for the three SNIa rates discussed in the text and non-solar ratios. The third column gives SSP  $\chi^2$ , the 4th, 5th and 7th columns give GCE  $\chi^2$  for the smallest, mid and largest SNIa rates considered. In columns 6, 8 and 9 the 1 means "yes" the  $\chi^2$  in the GCE  $\chi^2$  column next on the left is indeed less than the  $\chi^2$  next further on the left, for the SNIa rate indicated in the column heading. A "0" indicates a higher  $\chi^2$ . T.Mean is the mean of all the means in a column.

The means and total means in Table 2.11 show the same story as a tally of the number of galaxies which have improved  $\chi^2$  as the SNIa rate increases. The mid and then highest SNIa rate tried generally produced the smallest  $\chi^2$  for Es and SOs. For Sa type galaxies, as the SNIa rate is increased, the  $\chi^2$

increases, with the exception of NGC 3623 (an Sa) and NGC 4312 (an Sab), which follow the opposite trend. In the case of Sb galaxies, the best  $\chi^2$  came from the mid and then smallest SNIa rates. The results indicate that E and SO galaxies favour higher end SNIa rates in their SFH, and that spiral galaxy bulges favour lower end SNIa rates in their SFHs.

### 2.10.3 Solar Ratio versus Non-Solar Ratio

#### Experiments Using WHT data

To extend earlier experiments with NGC 2831 comparing solar and non-solar ratios, the experiment described in section 2.8 was run on all the galaxies in the WHT data. This experiment was run with a medium supernovae Ia rate of  $6.5 \times 10^{-5} M_{\odot}^{-1} \text{ Gyr}^{-1}$ . The results are outlined in Table 2.12.

Type (NGC)		SN6.5	SN6.5	< Solar?
		solar	non-solar	
		GCE $\chi^2$	GCE $\chi^2$	
E	Mean:	251.87	151.14	10 of 11
SO	Mean:	163.09	206.67	3 of 7
Sa	Mean:	109.36	157.51	0 of 5
Sb	Mean:	96.66	133.47	1 of 9
Total				
Mean:		182.91	175.42	14 of 32

Table 2.12:  $\chi^2$  for different galaxy types, for solar and non-solar ratios, with SNIa rate of  $6.5 \times 10^{-5} M_{\odot} \text{ Gyr}^{-1}$ . The final column gives the number of galaxies of the total of a given type in the WHT data, which had smaller  $\chi^2$  in the non-solar abundance ratio case.

Table 2.12 shows that a non-solar abundance ratio model generally produces the lowest  $\chi^2$  for E type galaxies (with the mid SNIa rate applied and C0 of 2, C2 of 0.03). However, the opposite is true for other galaxy types. Thus, from the comparison of  $\chi^2$  the SO, Sa and Sb galaxies are generally better fit with solar like abundance ratios fixed in the models.

However, such a conclusion is not complete, since there remains the possibility that the choice of SFH (guided by an E sample galaxy) may be poor for these cases; a more thorough search of parameter space is needed to assess this. The solar abundance contour plots, though achieving a better  $\chi^2$ , indicate this is the case (see for example Figure 2.6a and Figure 2.6b). This is since the SFHs are not well constrained by the solar abundance ratio model despite the lower  $\chi^2$  achieved. A comparison of solar and non-solar abundance ratio contour plots for S0, Sa and Sb galaxies produces the same story as given summaratively at the end of section 2.10.2. Early analysis of these experiments, within the ranges tested, indicates:

- The SNIa rate of  $6.5 \times 10^{-5} \text{ Gyr}^{-1} M_{\odot}^{-1}$  gave the best fits for Es. The SNIa rate of  $12 \times 10^{-5} \text{ Gyr}^{-1} M_{\odot}^{-1}$  gave the best fits for SOs.
- For most Sa type galaxies, the best  $\chi^2$  were achieved for the mid SNIa rate of  $6.5 \times 10^{-5} \text{ Gyr}^{-1} M_{\odot}^{-1}$ .
- For Sbs, the best  $\chi^2$  were achieved when the SNIa rate was decreased, with most Sb types achieving their best fits with a SNIa rate of  $\sim 4 \times 10^{-5} \text{ Gyr}^{-1} M_{\odot}^{-1}$  and poorest best fits with a rate of  $\sim 12 \times 10^{-5} \text{ Gyr}^{-1} M_{\odot}^{-1}$ .
- Non-solar abundance ratio  $\chi^2$  led to well confined SFHs in parameter space compared to those of solar abundance ratios.
- For Es, better  $\chi^2$  were found with non-solar abundance ratios than solar ratios (see Table 2.12).

Considering the above findings, some (speculative) comparisons can be made with the work of other researchers (particularly as tabulated in Table 2.5 and Table 2.6). The SNIa rates for local Universe E-SO galaxies in Cappellaro et al. (1999) were at about  $5.29 \times 10^{-5} \text{ Gyr}^{-1} M_{\odot}^{-1}$  (or  $5.88 \times 10^{-5} \text{ Gyr}^{-1} M_{\odot}^{-1}$  as formulated by Navasardyan et. al 2001). This rate is close to

the mid SNIa rate found for the E type galaxies in the WHT data set; which was in itself closely matched by the observation for grouped galaxies found by Navasardyan et al. (2001). However, the GCE model best fits for SOs occurred preferentially with the high end SNIa rate.

Since observed rates are based on catalogued local Universe observations (i.e. Reduzzi and Rampazzo 1995), similar ages for the WHT sample of galaxies to those used to find SNIa rates by Cappellaro et al. (1999) could be assumed. Assuming that ages of SO galaxies in the WHT data set do not differ widely from those in Cappellaro et al. (1999), the only possibilities remaining are that either Cappellaro et al. (1999) observed far more E than SO galaxies from which to compile an overall SNIa rate, or that the GCE model fails to achieve good SNIa rates for SO type galaxies. The first of these possibilities seems difficult to test, since galaxies in the WHT data set were not found to have also been observed by Cappellaro et al. (1999), and since the identification of galaxy morphology is often called into doubt with regards to the distinction between an E and SO.

Matteucci and Recchi (2001) in models of SNIa rates (see Table 2.6 and Figure 2.4) produce for E type galaxies (in model 5) an overall SNIa rate of only  $0.68 \times 10^{-5} \text{ Gyr}^{-1} M_{\odot}^{-1}$ . Models 2 and 3 of Matteucci and Recchi (2001) however, which are not optimised for early-type galaxies, produce SNIa rates (5.06 in model 2 and  $5.68 \times 10^{-5} \text{ Gyr}^{-1} M_{\odot}^{-1}$  in model 3 respectively) far more likely for Es as found in best fits using the GCE model. Examining the model constraints for models 2, 3 and 5 (see Table 2.6), model 2 appears to have more similarity to the GCE model input parameters than model 5 (or indeed model 3) constraints. Threshold limits were not reached by runs of the GCE model or those shown in Figure 2.4, so are not included in this comparison of GCE model input parameters to Matteucci and Recchi (2001) model constraints. As to the fraction of binary star systems that result in SNIa, this is of no consequence in these comparisons; the GCE model's assumed SNIa rate does away with any model assumptions concerning the fraction of binary systems or the fraction of binary systems that result in SNIa.

That model 2 agrees more with the GCE model for Es than model 5 suggests that the stellar yields, or else the IMF, play an important role in the SNIa rate required for the best fit SFH of Es. That one model uses a Scalo IMF and another a Salpeter IMF is thought to be not significant (see Kroupa 2001 and Bolzonella et al. 2000 for relevant IMF discussions). However to answer the question that rises from this speculation of a significant connection between SNIa rates and stellar yields would require work beyond the scope of this thesis; for the sake of consistency, changing IMS stellar yields (i.e. from RV81 as used in model 3 to the model 5 MBC yields) in the GCE code, and re-running experiments on SNIa rates for the WHT early-types.

The WHT late-types had predominantly low end SNIa rates in best fits with the GCE model, comparable to the lowest observational value of Navasardyan et al. (2001). The low end SNIa rate for spiral bulges differed markedly to the high,  $11.83 \times 10^{-5} \text{ Gyr}^{-1} \text{ M}_{\odot}^{-1}$  found by Samland (1998) for our own spiral galaxy. The work of Samland (1998) dealt with SNIa observations away from the center of the Milky Way Galaxy, whilst the WHT data set late-types consisted of observations of spiral bulges. Most star formation occurs in the spiral arms of spiral galaxies (Carroll & Ostlie 1996, p. 1013), and the spiral arms form quite early on in the formation of such galaxies (Carroll & Ostlie 1996, p.1015). Why the overall SNIa rate is not nearly so high in the GCE model (or those of Table 2.6) as in Samland (1998) seems to have only two plausible answers; that the SNIa rate in the Milky Way is unusually high at this time, or that the value quoted in Samland (1998) is somehow an over estimate. The discussion given above concerning the comparison between GCE model input parameters used for Es and the model 2 constraints applies here also for Sbs.

Suggestions for further testing of the GCE model, to distinguish between different galaxy types and increase confidence in the results from the GCE model, are discussed in section 6.3.

## Chapter 3

# Observations and Initial Data Reductions of LLEs

In this chapter the preparation for new observations to produce a data set, besides the WHT data, to investigate galaxy formation scenarios is described. The motivation for these observations is described in section 1.3, with the appropriate motivational point recalled in section 3.1. Following the observation descriptions, the observations themselves are summarised by Table 3.1 and Table 3.2. The data reduction methodology is then given, from initial data handling to flux calibrations. The last section of this chapter details the initial handling of data for measurements of kinematics in IRAF.

### 3.1 Preparations for Observations with EMMI on the NTT

An observing run (mentioned in subsection 1.3.1) was successfully sought at the ESO NTT. These observations were to serve the purpose of providing some of the data and training for the PhD, so a "visitor mode" was therefore applied for. In visitor mode, as oppose to service mode, astronomers work on site to undertake the observations they have applied for. Initially about 20 local Universe LLEs in the southern hemisphere were selected for observation. These were selected for being LLEs of low or else unknown  $\sigma$ , distance ( $\leq 20$  Mpc), and B band Magnitude ( $M_B > -19$ , with the exception of NGC 2784).

NGC 2784 was chosen as a control, with a mid-range  $\sigma$ , from the WHT data set. NGC 2784 (see Figure 5.2 and Table 4.5) had errors comparable to those in the WHT data set. As a control, NGC 2784 showed that the NTT and WHT data sets, after the reductions and calibrations described here and in Chapter 4 on the NTT data, remain comparable.

Only 3 of the requested 5 nights observing were granted. For this reason galaxies had to be further sub-selected. The study of LLEs using the NTT was proposed, with the intention of achieving high enough signal-to-noise, to measure accurately their Lick indices, including age indicators (e.g. H $\beta$ , H $\gamma$  and H $\delta$ ). Further, accurate  $\sigma$  values were sought, in some cases of galaxies that had not had their  $\sigma$  measured before.

In PS02 trends of Lick Indices versus  $\sigma$  for the WHT data (Es, SOs and spiral bulges) were found. However, the WHT data lacked observations of LLEs, though galaxy formation models should be supported by observations of galaxies of all observable masses. The trends plotted lacked in particular points for low  $\sigma$  (i.e. below about 79 km s<sup>-1</sup> less than which only one data point was plotted). Therefore, in seeking a new data set, LLEs, particularly at low  $\sigma$ , were selected to observe.

Preparation for observations was done in part using information available from the European Southern Observatory (ESO) web site:

“<http://www.ls.eso.org/lasilla/sciops/ntt/emmi/>” (hereafter EW).

The wavelength range was chosen to include the same Lick indices as in the WHT data, to enable direct comparison of data sets. The Lick Indices were discussed in section 2.1. The red arm of the EMMI instrument (see Figure 3.1) was chosen, so that the available wavelength range, could cover all of the Lick indices. By design, observations in EMMI are done in REMD (Red Medium Dispersion Spectroscopy mode) for  $\lambda > 400$  nm and BLMD (Blue Medium Dispersion) for  $\lambda < 500$  nm (from the EW web site extension “/emmiGeneralDescription.html”). In the region of overlap, REMD gives larger lambda coverage and better spatial sampling, while BLMD gives better image throughput.

Before wavelength calibrations could be completed (see section 3.3) regions of strong vignetting (about 29 Å from the red end) had to be

excluded from the data. Following the wavelength calibrations described in section 3.3, the identified wavelength range observed is from 405.2 to 559.7 nm. This wavelength range was carefully checked by way of the line identifications of the wavelength calibration process. A discrepancy was identified between the measured wavelength range and the wavelength range from EW, believed to probably be due to unaccounted for estimations of vignetting on EW. The EW website no longer quotes the wavelength range specifically.

Information on the galaxies selected for observing has been catalogued in “The Third Reference Catalogue of Bright Galaxies” (de Vaucouleurs et al. 1991), hereafter RC3.

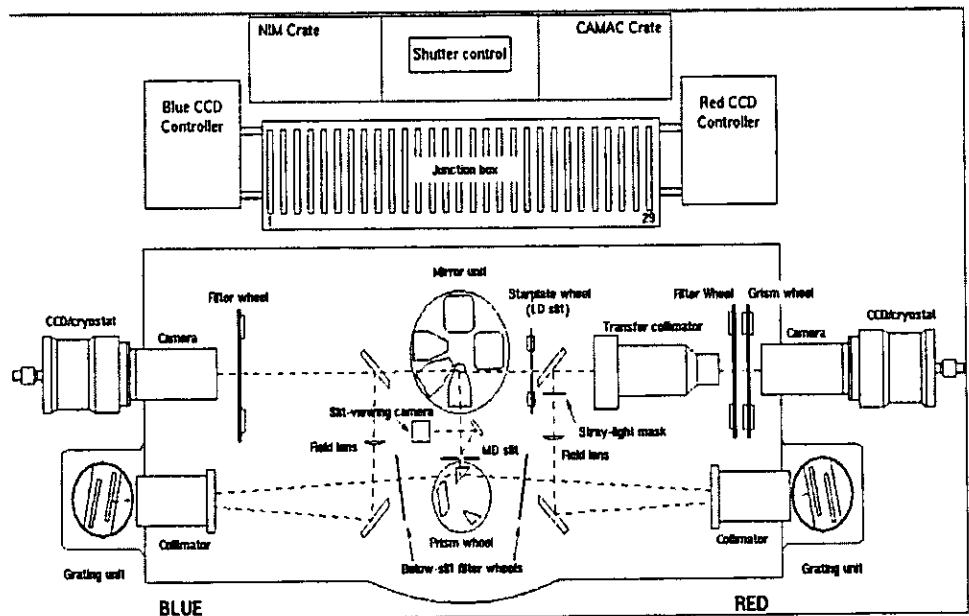


Figure 3.1: EMMI optical layout (from EW, extension “/EMMIlayout.gif”). In the REMD mode used, the light path is from the shutter control (top of this Figure), to the mirror unit, then to the prism wheel, and from there to the RED collimator and then grating unit. The light dispersed at the grating unit is reflected back past the collimator, to a 45° flat mirror, to the field lens, stray-light mask, to another 45° flat mirror, then to the transfer collimator. The filter wheel and grism wheel were not needed for the chosen wavelength range. Finally, the light passes into the camera and then reaches the detector within the CCD cryostat.

Information about EMMI was retrieved from the EMMI web pages. The EMMI instrument has a pixel scale of 0.166" per pixel (EW, extension "/emmiDetectors.html"). The dimensions of the detector are 4152 x 4110 pixels (spread equally over four chips) for the red CCD. The resolving power achievable with EMMI, using grating 7, is 2600 (EW, extension "/emmiGeneralDescription.html"). At a central wavelength of about 500 nm, this gives a spectral resolution of 0.192 nm FWHM. For the wavelength range used (about 405 to 560 nm across 3754 pixels) a dispersion of 0.041 nm per detector pixel was derived. A slit was selected of dimensions 1" by 300" (in the wavelength and spatial directions respectively) to detect light from across a galaxy and from neighbouring sky.

To aid the choice of science objects to observe and also acquisition of chosen galaxies during observations, finding charts were produced of the entire sample of galaxies and stars to be observed. Data, including images, for finding charts, were taken from the Nasa Extragalactic Database (NED). A finding chart sheet is given as an example in Figure 3.2. In Figure 3.2, "T" is for "Type" which refers to the Hubble type based on the RC3 mean numerical galaxy type.

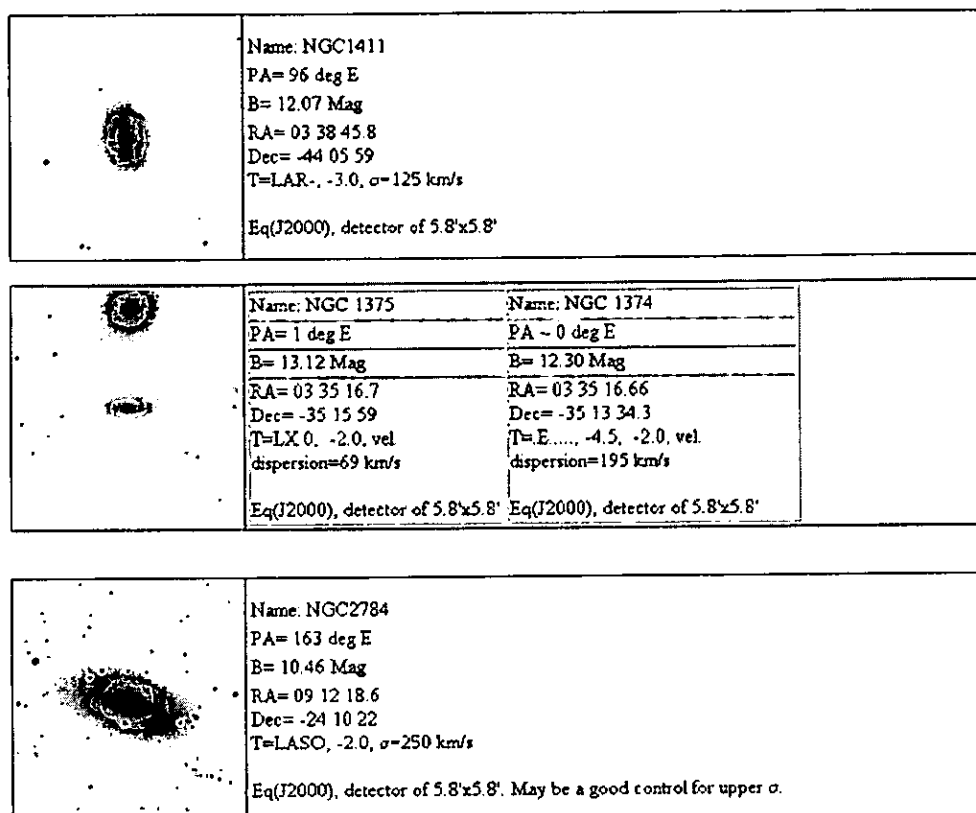


Figure 3.2: Sample finding charts, with images taken from NED. NGC 1375 and NGC 1374 are shown in the middle finding chart, NGC 1375 being placed centrally within this chart. The position angles (PA) are for identifying the position of the minor axis of galaxies, against which the length of the slit was aligned. North is up and East is left on the charts. Where the symbol  $\sigma$  is used, this is for velocity dispersion.

Flux calibration stars were selected from lists of standard stars given on the NTT web site (EW, extension “/observing/calplan/calplan.html”). Flux standard stars were chosen for having stable spectra that are relatively smooth, in the wavelength range observed, compared to other stars. This is important so as to be able to calibrate for flux in a wavelength dependant manner without introducing features from spectral lines into the calibrations. Therefore, selected flux calibration stars (as shown in Table 3.2) are bright O or B type stars. For calibration to the Lick standard system stars were chosen from Faber et al. (1985) and Worthey et al. (1994) by Sansom (private communication, 2003). These stars are lower temperature stars than the flux calibration stars; as such they have more complex spectra.

A link was found off the EW URL to the on-line Exposure Time Calculator (from “<http://www.eso.org/observing/etc/bin/gen/form?>”), which was used to check for saturation at integration times at least several multiples of the telescope shutter speed. Part of the formal preparation for use of the NTT instrument was the production and submission of Observing Blocks. An example is given in the EMMI manual (issue 4.6).

## 3.2 Observations

Observations were carried out on the nights of the 25<sup>th</sup>- 27<sup>th</sup> November 2003. The finding charts proved very useful in the final choice of galaxies. For example, identifying from finding charts the opportunity to line-up the centre of two spheroidals in the slit (NGC 1375 and NGC 1374) was useful for the purpose of increasing the sample of observed galaxies.

Twelve galaxies were observed, with the slit running along the minor axis of each spheroid in turn. The position angle of NGC 1374 is nearly zero and not significantly out of alignment with the minor axis of NGC 1375 (see Figure 3.2); therefore a PA of 0 degrees was used. Two to six exposures of approximately twenty minutes each were made for each galaxy (dependant upon brightness of the object).

Flux and Lick calibration stars were observed, totalling 3 flux and 17 Lick standard stars. A few of the observed galaxies have spectra dominated by emission lines. One emission line example is ESO 118-34, which appears to have been misclassified as not being emission line dominated from notes read on the NASA Extragalactic Database, (NED). A subsequent paper search revealed its identification as a HII emission galaxy (Brosch et al., 2000). Relevant characteristics of galaxies and stars are noted in Table 3.1 and Table 3.2. Calibration images (such as biases and flat-fields) were generated largely during the day, or else near twilight along with the star exposures. Several calibration arc images were taken at various rotation angles, on the advice of support astronomers. This was since it was expected

the wavelength scale would shift across the detector, for different rotation angles. Short exposure arcs were taken after the last exposure of each galaxy or star. These arcs, taken after final science object exposures, were to track any time dependant variability in the effect of rotation angle (see subsection 3.3).

There were some instrumental difficulties during the observing run. During the second night, a problem with the Helium-Argon arc lamp meant the loss of Helium spectra from arcs in some exposures. Argon lines remained identifiable and numerous enough for wavelength calibrations. During the first night the dome flat lamp failed, so that no dome flat calibration images could be taken that night. Further, a mechanical failure with the prism wheel meant observations were temporarily (for about 1 hour) on hold during the second night. Heavy cloud cover over the first night (with humidity near to the telescope “dew point”), and partial cloud cover over the second, resulted in lower photon-counting statistics than would have been achieved in some exposures (particularly those of NGC 59).

Galaxy	Type	T	Hubble Type	Bm	Bmc Ab.	$r_e$ (")	Exp (sec)	Air Mass Range
NGC 1411	.LAR-*	-3.0	Lenticular	12.07	-17.94	13.71	7200	1.036-1.0605
NGC 2784	.LASO*	-2.0	Lenticular	10.46	-19.16	26.74	2400	1.0795-1.1185
NGC 59	.LAT-*	-2.5	Lenticular	13.04	-	21.73	7200	1.0115-1.074
ESO 118-34	.L..OP*s	-2.0	Lenticular	13.49	-17.07	6.27	7200	1.168-1.287
NGC 1331	.E.2.*.R	-5.0	Elliptical	14.22	-16.69	9.27	7200	1.0515-1.2655
NGC 1375	.LX.0*/	-2.0	Lenticular	13.12	-16.34	16.49	7200	1.008-1.054
NGC 1374	.E...	-4.5	Elliptical	12	-19.10	24.38	7200	1.008-1.054
NGC 3125	.E...?	-5.0	Elliptical	13.11	-17.54	7.89	2400	1.1115-1.158
ESO 157-30	.E.4.*.	-5.0	Elliptical	14.52	-16.70	-	9000	1.112-1.209
NGC 2328	E-SO	-2.8	Lenticular	13.23	-17.74	-	7200	1.028-1.046
ESO 358-59	.LX.-.	-3.0	Lenticular	13.99	-16.25	12.51	7200	1.009-1.0355
NGC 1373	.E+.*.	-4.3	Elliptical	14.08	-	-	3816	1.035-1.274

Table 3.1: Galaxies observed with NTT, November 2003. Type, T Type and half light radii ( $r_e$ ) are from RC3. Bolometric apparent magnitudes (5<sup>th</sup> column) are from HyperLeda. In the 6<sup>th</sup> column are absolute magnitudes from HyperLeda. The Missing values are shown as “-”. Air mass range is derived from the smallest and largest mean air mass for each set of exposures (Exp) taken for each galaxy, and from the headers of FITS files handed down from the telescope.

Stars	Spectral Type	V Mag	Exposure Time (secs)	Air Mass Range
<b>Flux Calibrators:</b>				
HR8634	B8V	3.40	10	1.32-1.34
HD49798	sdO6p	8.27	10 to 50	1.07 to 1.11
HR3454	B3V	4.27	10 to 30	1.19 to 1.20
<b>Lick Calibrators:</b>				
HR3845	K2.5III	3.90	2 to 5	1.23
HR8841	K0III	4.21	10	1.07
HR72	G0V	6.40	10 to 30	1.10
HR203	G2V	6.15	30	30
HR3994	K0III	3.61	5	1.18
HR296	K0III	5.40	10	1.18 to 1.19
HR8924	K3III	6.30	10	1.11
HD211038	K0/K1V	6.54	10	1.09
HR509	G8V	3.50	5	1.18
HD219617	F8IV	8.16	50 to 100	1.05
HR2574	K4III	4.08	5	1.14
HR2701	K0III	4.92	10	1.2
HR2970	G9III	3.93	10	1.09
HR695	G2V	5.19	10	1.24
HR1136	K0IV	3.51	5	1.26
HD064606	G8V	7.44	100	1.14
HR4287	K1III	4.07	10	1.23

Table 3.2: Calibration stars observed with NTT, November 2003. Where the same air mass was found in exposures or only one short exposure was made of a star, air mass range is single valued. In other cases, were two or more exposures were taken and each was found to have a different air mass, a range is given.

### 3.3 Data reductions

Basic data reductions were carried out using Starlink and IRAF software packages. Propagation of errors was not supported by many individual programs within each package. For this reason error propagation often had to be processed “in parallel” with reductions carried out on the data. Error propagation of this kind relied chiefly on the KAPPA:CREOBJ and COPOBJ commands. These commands can be used to make array envelopes and then copy variances into them for processing (and then back into the relevant emptied variance array). Where the handling of errors mainly occurred non-parallel to the data, this is mentioned in the text below. The

main Starlink package used for detector characteristic removal, wavelength calibrations, sky subtraction and flux calibrations was FIGARO. Example commands within FIGARO used are BCLEAN (for cosmic ray removal), ARC (for identifying lines in arcs) and POLYSKY (for sky subtraction). The other main Starlink packages used were KAPPA (for image transformations) and CCDPACK (for image mosaicing). These programmes were used within C-Shell scripts (see appendix B).

Data from the NTT comes in a 4 frame, separate image FITS format, with one frame for each EMMI CCD chip. These FITS files were transformed into single image SDFs (Single Data Formats). Chips are conventionally labelled as D, C, B and A, going from left to right across the detector. Frames were aligned using image header information and KAPPA world co-ordinate system subroutines adapted to provide an AXIS based co-ordinate system directly onto images. Images could then be aligned (using KAPPA) and mosaiced (using CCDPACK). Once the four frames were mosaiced into single frame images, the slit extent was used to subset the data in each image. The area of each image that represented the slit extent was then used as individual data subsets, on which all subsequent data reductions were performed. This was required because the CCD chips had different bias levels, both between each other and from going from within to outside the slit extent within the area of a chip. Since bias strips were designed to be used for calibrations within the slit extent, subsetting the slit was a prerequisite to bias subtraction and subsequent removal of the bias offset (see below). Figure 3.3 shows the EMMI CCD detector with the slit extent and other notable detector characteristics indicated (see caption for details).

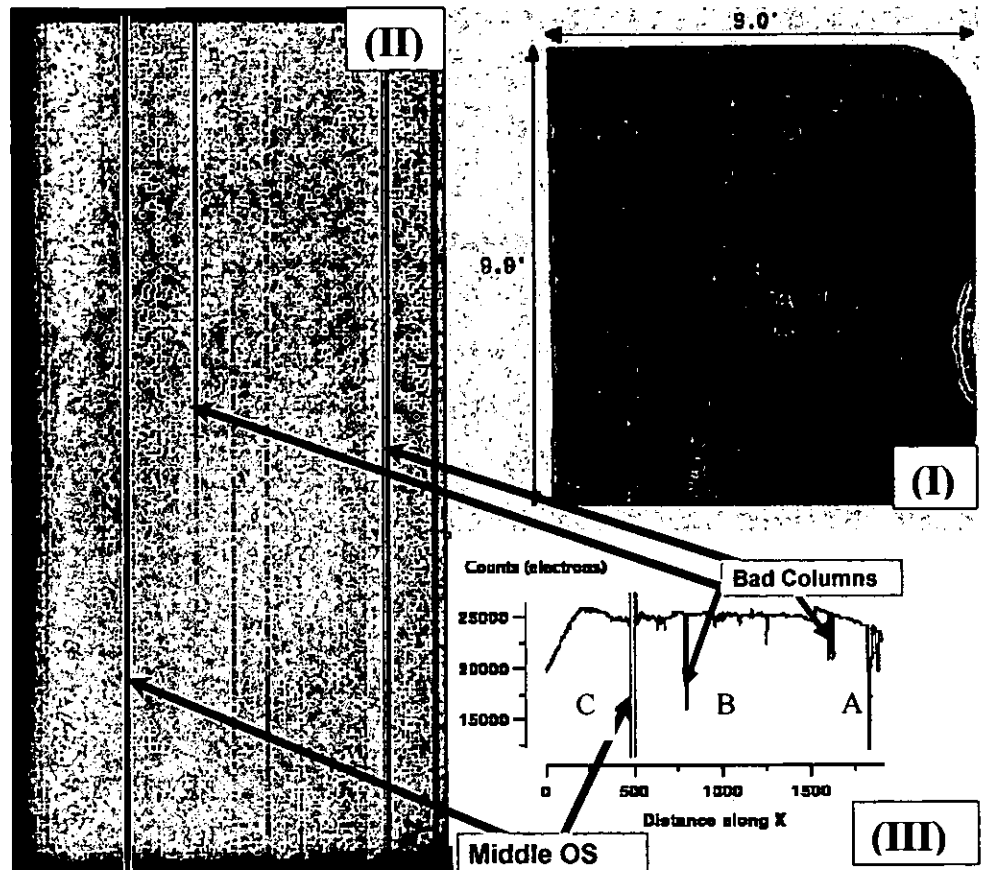


Figure 3.3: CCD frames: Zeus (master chip, on right of CCD gap) and Michelle (slave chip, on the left of CCD gap). Image (I) in its original form is from the EMMI web site (EW, extension "/emmiDetectors.html"). Image (II) represents the chosen extent in a debiased dome flat image, showing structure in the CCD. For example, vignetting can be seen at the left side and bottom edge of image (II). Image (III) gives the mean spatial profile, showing the middle over scan region (OS) and bad columns. The red box overlaid on the (I) dome flat image indicates approximately the area illuminated by the chosen slit, which was subsetting for data reduction purposes. The chosen extent includes all of chip B and parts of chips A and C. These are noted on (III), where C is left of the mid OS and A is right of the pixel spatial position of 1534.

Initial cosmic ray cleaning was carried out using FIGARO:BCLEAN, by searching for the number of sigma deviations from the mean value of nearest neighbours. However, the extended nature of many cosmic rays (CRs) prevented the process from being entirely successful. Further, BCLEAN is sensitive to the difference between the background count level

and the count level of CRs. The greater the difference, the more easily BCLEAN isolates and cleans CRs.

After debiasing a significant difference between the background level of counts in science data area and the level of counts in cosmic rays was identified. This difference was significant when compared to the difference in level of counts between background and science data. The process with BCLEAN was therefore repeated after debiasing, when the effect of this difference in aiding isolation of cosmic ray pixels from data could be optimised. The effectiveness of cleaning at this stage is shown qualitatively in Figure 3.4. Cosmic rays were further removed in later stages of data reduction from the master bias, dome flat and, after wavelength calibrations, combined galaxy images. This was done by way of stacking repeat exposure images using a sigma clipped mean for overlapping pixels.

Debiasing was designed so as to account for the different bias levels and bias structure in each chip of the CCD. The mean of the bias level of each master bias frame's overscan region was subtracted from each pixel in each corresponding calibration frame and science frame. An offset between the mean bias level in the data and the mean bias level in the bias strip for each frame was found in the master bias. This offset was also removed from the science data of each frame as appropriate. Figure 3.5 shows the unbiased mean spatial profile, for a galaxy image. Figure 3.6 shows the remaining step (about half a count) between frames A and B in a reduced galaxy image.

After debiasing, the error remaining in the images was assumed to be dominated by Poisson statistics. There were also possible slight systematic differences, between bias images, resulting in a bias deviation. Such a bias deviation could be found by testing for possible deviation of an individual bias mean greater than the mean bias standard deviation. Algorithms were scripted to test for such a bias deviation in individual debiased bias frames. A small bias deviation was found. Variance arrays were introduced into the 2-d files. This error due to the bias deviation was later deemed negligible, when compared to the Poisson noise in both science and calibration images.

Master dome flats were made by stacking the dome flats for a given night, using CCDPACK:MAKEMOS. Each pixel of the stacked image was an

error weighted mean. This master dome flat was then calibrated to counter the spectral response of the detector due to the dome flat lamp, using chiefly FIGARO:MCFIT. This was achieved by taking the unflattened spectrum of the master dome flat, dividing it by the number of columns in the spatial direction, and fitting a spline. Too few points in the spline produces a poor fit, whereas too many removes small scale features from the spectrum. Therefore the number of points was chosen carefully, through trial and error. The given numbers of points are equally placed in the spectrum. Then at each point the mean of the surrounding points is taken and a new spectrum is formed by interpolating between the mean values. The result is a smoothed spectrum, which represents the spectral gradient due to the dome flat lamp. This smoothed spectrum could then be used to divide out the spectral gradient in the master dome flat. The middle overscan region was omitted from this procedure. The spline failed to fit the very edges of the data where the spectral shape varied rapidly, due to vignetting in the spectral direction. Therefore, the extent of images (other than bias frames) was reselected prior to spectral calibration of the master flat. Since MCFIT did not successfully handle error propagation, errors were estimated from a comparison of the output of MCFIT and the original spectrum; the error being taken as the difference in the continuum level of the two spectra. The command ISXDIV was used to divide the stacked dome flat by the spline fitted spectral calibration image. ISXDIV failed to handle error propagation correctly, to which a correction was calculated and mathematically applied using chiefly ICMULT. The error equation used on each element of the variance array was then as appropriate for division of two values each with their own error. Calibration and science data were divided directly by the normalised, mean (of all dome-flat images in a given night), master flatfield.

Support astronomers had advised that rotation angle may affect arcs significantly. Therefore, relative rotation angles of each arc per science exposure were investigated, within and between nights. Comparison of the shift in wavelength direction (from running FIGARO:SCROSS) with rotation angle, relative to a reference arc from the first night, revealed a significant variation in shift between nights and at larger relative rotation angles (see Figure 3.7). Since the rotation angle varied from the start to the

end of exposures, mean rotation angles for each exposure were used to make the graphs given in Figure 3.7. As is shown in Figure 3.7, rotation angle has a significant effect, which varies between nights. Arcs of exposure times much less than 300 seconds, mostly made after science object exposures, were excluded from wavelength calibrations. This was due to the weak lines of these arcs, which were found to lead to poor line positioning. The choice of arcs to achieve wavelength calibrations was therefore made by matching each science exposure to an arc of the nearest relative rotation angle, within a night, for arc exposures of about 300 seconds.

The position of the peak count in 1D spatial plots of each galaxy image was located, so that overall galaxy images could be shifted into alignment and then stacked to form single exposure images for each galaxy. Wavelength calibration was done using chiefly FIGARO:ARC, IARC and ISCRUNCH. Prior to running ISCRUNCH, mid overscan regions in arcs and science exposures were reduced to zero, so as to allow better fitting by ISCRUNCH. Arc lines in 1D arc spectra were matched using ARC which used line positions given in FIGARO line lists. Drawing upon ARC outputs, IARC was used to generate a row by row wavelength scale file for each science exposure. ISCRUNCH was then used to scrunch 2D science spectra to wavelength scales appropriately. Variance arrays were scrunched in parallel to data arrays for each science object. The resulting calibrations were checked by visualising the calibrated science 2D images in GAIA and 1D spectra in splot. The RMS in position of the centroid of a major sky line (OII forbidden line at 551.7 nm) was investigated across each calibrated image as a wavelength calibration check. This was done using FIGARO:IMAGE, ICUR, IMPOS and CENTERS.

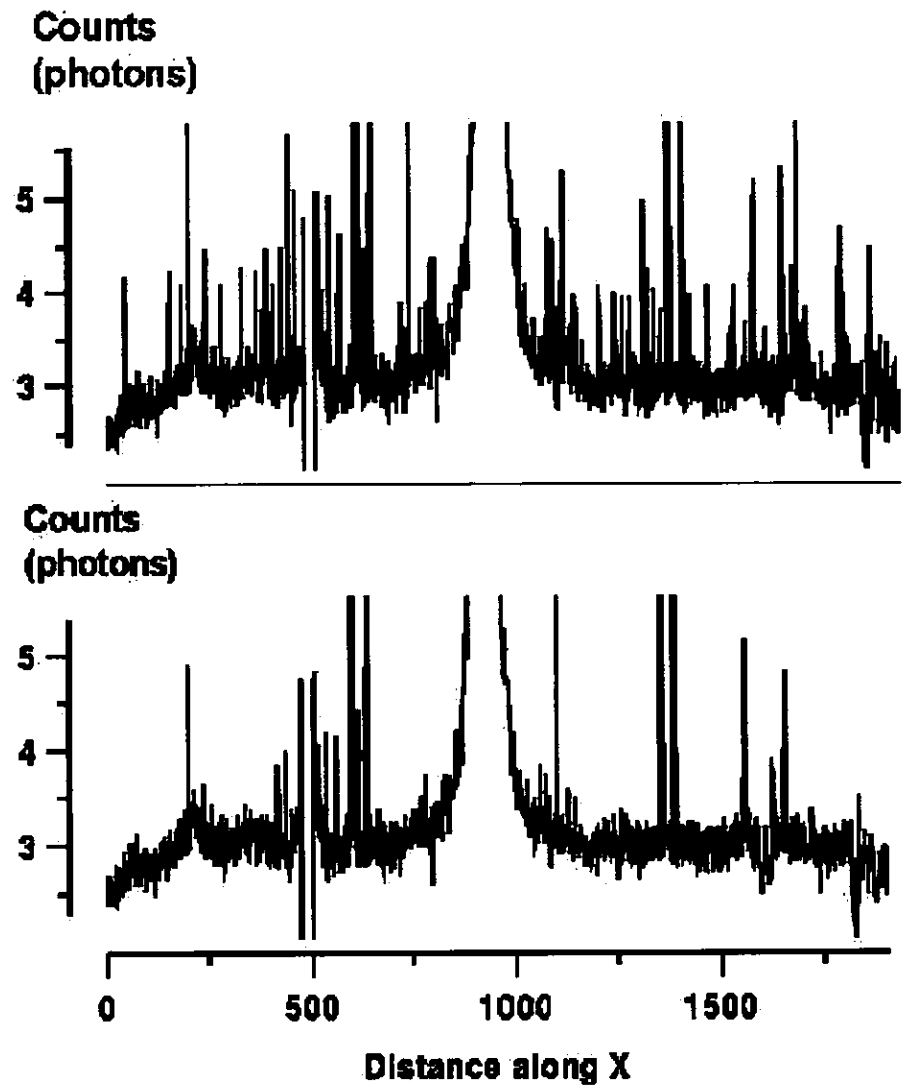


Figure 3.4: A debiased galaxy exposure mean spatial ( $x$ ) profile before (top) and after (bottom) initial cosmic ray cleaning.

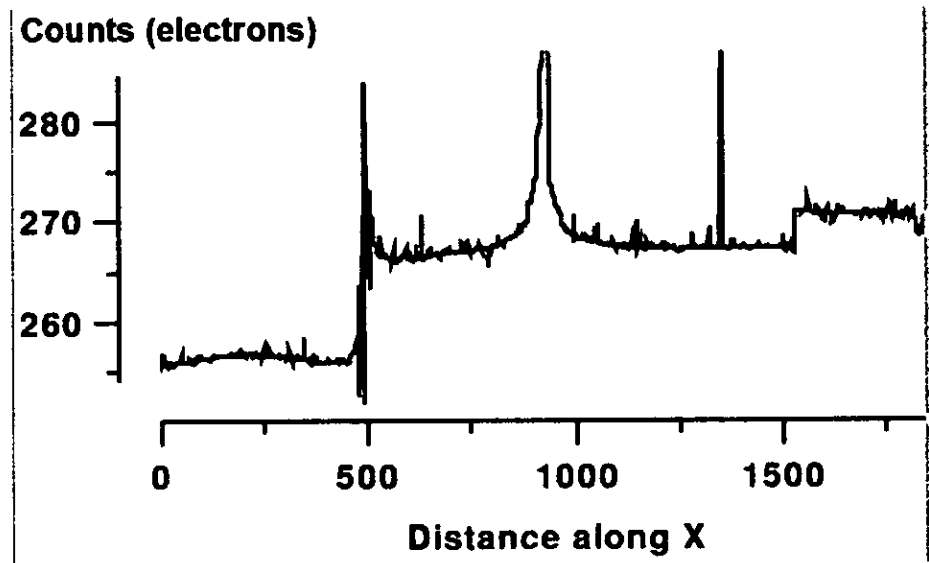


Figure 3.5: The bias offsets, before being removed by debiasing. This is before the final run of BCLEAN. Shown is the mean spatial profile taken from the first exposure made of NGC 59. Steps at CCD chip boundaries are of size 5 to 10 (electron) counts. Pixel to pixel variations due to noise or other detector variations are typically far less than this step size, as can be seen in the plot.

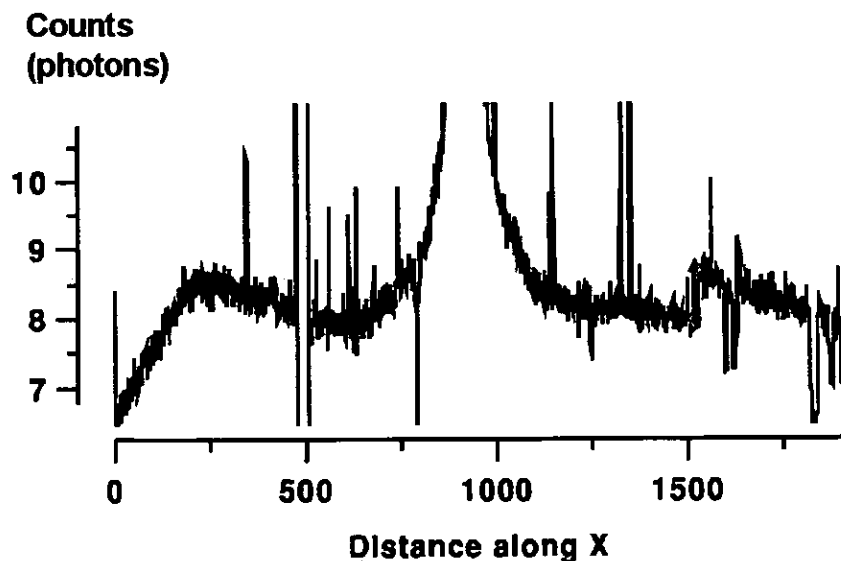


Figure 3.6: Residual step between frames after debiasing. A small step in the bias level remains between chips in this debiased galaxy image. The largest step, at just over half a (mean photon) count, is indicated by the red arrow. This mean spatial profile is of the same exposure of NGC 59, as used in Figure 3.5. The conversion factor between electron and photon counts varied from chip to chip, but was about 1.4 electrons per ADU (Analogue Digital Unit).

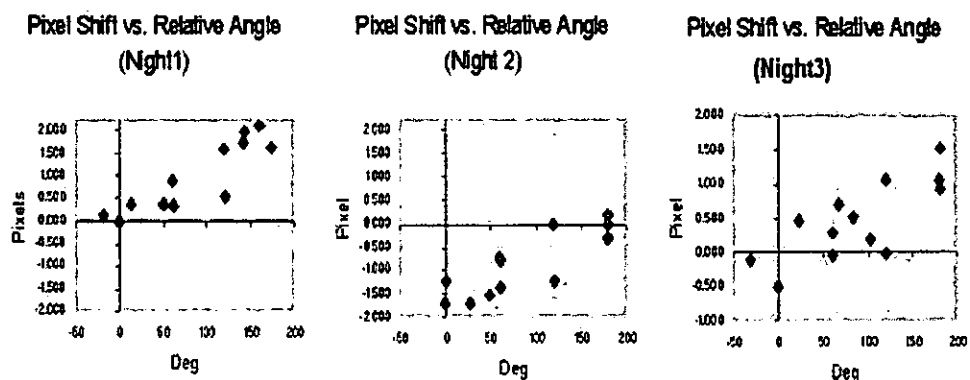


Figure 3.7: Correlation in the shift found in cross-correlations of arcs to a reference arc (the first arc taken during the three night's observing), is shown here. Variation in the shift of spectral lines is rotation angle dependant (seen within a night). Variation also appears to be time dependant, on the scale of night to night variation (as seen in the different plots).

So as to align galaxy images, the location of galaxies in each exposure was first determined (using chiefly FIGARO:ISTAT). The co-ordinate origins of each exposure were set to the same value relative to the location of each galaxy within its independent image (using KAPPA:SETORIGIN). Alignment could then be achieved by stacking images using MAKEMOS. MAKEMOS was used so as to find the median of individual stacked pixels. This method helped to remove left over contamination from CRs, whilst correctly handling the data and variance arrays of images.

Sky background was subtracted (using FIGARO:POLYSKY) before extinction corrections and flux calibrations. Regions of sky for subtraction were selected from either side of science objects, taking care to avoid any areas of images where remaining CRs or/and bad columns might produce an inaccurate subtraction. Since POLYSKY did not handle error propagation, errors were merely copied from the pre sky-subtraction images as appropriate. To analyse the effect of a different selection of sky for subtraction, sky subtraction was re-run with a new sky region selected using the same criterion as before. Reductions of observed galaxies of different sky selection were done in parallel. This was so that error resulting from the choice of sky could be calculated appropriately from the mean difference

between measurements of Lick Indices in the galaxy spectra of different sky selection (see section 4.4).

FIGARO:EXTIN was used to extinction correct all science objects. Atmospheric extinction coefficients had not been taken at the time of observing. The extinction coefficients last recorded at La Silla were measured in 1997. However, these coefficients covered only a few positions in wavelength, so a more complete tabulation of relevant extinction coefficients was sought. Extinction corrections using coefficients from other years than that observed in were not expected to be any less valid (Burki et al. 1995). The most complete list of extinction coefficients for La Silla found was that from the ESO Manual 1993 and so this was used. This list of coefficients was turned into an extinction calibration spectrum using FIGARO:GSPIKE for a spiketrum and then SPIFIT to fit a 3<sup>rd</sup> order polynomial (selected through by trial and error qualitatively) to the spiketrum.

Air masses for exposures were taken as the mean air mass for any given exposure or combined image. In an earlier test of extinction corrections on individual galaxy exposures pre-combination had yielded the same result (i.e. with no discerned difference) as extinction correcting the combined galaxy exposure images. The extinction corrections were calculated by EXTIN using the Kasten (1989) formula (equation 3.2), which required airmass ( $\alpha$ , calculated using the Kasten (1966) formula, equation 3.1) and zenith angle ( $Z_e$ , in degrees) as inputs:

$$\alpha = (\cos(90-Z_e) + 0.15*(93.885-(90-Z_e))^{-1.253})^{-1} \quad \text{(Equation 3.1)}$$

$$ED(i) = SD(i)*10^{(0.4*CD(i)*\alpha)} \quad \text{(Equation 3.2)}$$

In equation 3.1, the elevation angle is used (90- $Z_e$ ). In equation 3.2,  $ED(i)$  and  $SD(i)$  are the  $i$ th elements of extinction corrected and non-extinction corrected science data respectively.  $CD(i)$  is the  $i$ th element of the extinction calibration spectrum, or in other words the  $i$ th extinction coefficient. Mean zenith angles calculated from start, mid and end zenith angles was not possible. This was since only the start zenith angles were handed down from the telescope. Variance arrays were recalculated by simply running the EXTIN programme twice on the original variance arrays ( $SD_{vo}$ ) separately,

before returning them to images as appropriate. This handling of variance arrays was designed after considering equation 3.2 and the standard laboratory error equation (see equation 3.3). Equation 3.4 gives the new variance (SDv) for each  $i$ th element.

$$\text{If } x = p \cdot q, \text{ then } \sigma_x = x \cdot (\sigma_p/p)^2 + (\sigma_q/q)^2 + \dots)^{1/2} \quad (\text{Equation 3.3})$$

Where  $\sigma_x$ ,  $\sigma_p$  and  $\sigma_q$  are the errors for  $x$ ,  $p$  and  $q$  respectively. To arrive at equation 3.4, some substitutions were made from equation 3.2 into equation 3.3. From equation 3.2,  $x$  is  $ED(i)$ ,  $p$  is  $SD(i)$  and  $q$  is  $10^{(0.4 \cdot CD(i) \cdot \alpha)}$ . For the variances,  $\sigma_x^2$  is  $SDv(i)$ ,  $\sigma_p^2$  is  $SDvo(i)$  and  $\sigma_q^2$  is taken as zero (as error in calibration spectrum was unknown).

$$SDv(i) = SDvo(i) \cdot 10^{[(0.4 \cdot CD(i) \cdot \alpha) \cdot (0.4 \cdot CD(i) \cdot \alpha)]} \quad (\text{Equation 3.4})$$

For flux calibrations, FIGARO was used. The 2D observed Lick star spectra were collapsed to 1D spectra using FIGARO:EXTRACT. The absorption regions in the flux star standard calibration spectrum needed to be removed. This was so that the absorption regions did not affect the calculated instrumental response. To achieve this, template spiketra were created that excluded fully the absorption lines. These template spiketra could then be used to generate absorption line free observed spiketra (using FIGARO:GSPIKE), from which smoothed interpolation spectra could be made. To optimise fits to spiketra near the edges of data so as to form spiketrums, various polynomials and also linear interpolation were tried. Using FIGARO:SPIFIT, which gave the best fits using a 4<sup>th</sup> order polynomial, the smoothed interpolation spectra were then generated.

FIGARO:CSPIKE calculates the instrumental response for the tabulated points found in the appropriate calibration spiketra for an observed star spectrum. The differing bandwidths used by the standard star spiketrum and observed flux spectrum did not lead to error. This was since CSPIKE is designed to appropriately resample the observed flux spectrum or spiketrum using the wavelength positions used in the standard flux spiketrum.

Flux calibration tests were carried out. Only model data could be found in part of the required wavelength range for a standard flux spectrum of HD 49798. For this reason, HD 49798 was only included in this analysis for comparative purposes. Flux calibration star spectra were then divided into the relevant standard flux calibration spectrum (from URL:<http://eso.org/observing/standards/spectra/stanlis.html>) following appropriate normalisations to account for exposure time. An example division is given below in Figure 3.8, which shows the method worked well (mean of  $\sim 1.004$ , standard deviation of  $\sim 3\%$ ) except very near the edges of the data.

Following this, the reproducibility of the shape of the instrumental response was investigated, by way of qualitatively examining plots of instrumental responses. These instrumental responses were first appropriately normalised by their individual means. The shapes of the instrumental plots showed the least variation for HR 8634. The small variations apparent in the red and blue ends of the HR 8634 instrumental response were only a few percent (see Figure 3.9). For the first two nights, HR 3454 also produced instrumental responses that were fairly similar. From Table 3.3 it can be seen that the mean absolute values varied on a night to night basis least of all for HR 8634. In the case of HR 3454, it is thought that the flux varied more strongly due to more varied atmospheric conditions. From the normalised instrumental response derived using HR 8634 and HR 3454, there was no evidence of any nightly dependence in the instrument response.

Flux calibrations of galaxy images and Lick star spectra were performed using a single mean instrumental response. This was constructed from the first and second night HR 8634 and HR 3454 exposures from the above analysis. Each instrumental response was normalised to unity, by way of division by the appropriate mean absolute value. The normalisation was performed since absolute values for instrumental responses varied from exposure to exposure unpredictably. This was thought a likely result of variable cloud cover (such as was noted during observing). Normalisation also served the purpose of removing the units of the flux calibration, so that flux calibrated objects maintained their units of photon counts per second.

Signal-to-noise ratios (S/N) were checked, using FIGARO:SPLIT to view debiased galaxy spectra. Measurements were on sections of continuum at both ends of each spectrum as well as the middle of each spectrum. The S/N, as calculated by SPLIT, is averaged per pixel, which is per logged wavelength bin (i.e. the log of the dispersion). The S/N was found to typically have an average as good as  $\sim 75$  per pixel at about the middle wavelength of 500 nm. The S/N though was somewhat low in NGC 59. NGC 59, which has the observation attributed to it thought to be through more cloud cover than any of the other individual galaxy observations, was found to have an S/N of  $\sim 36$ .

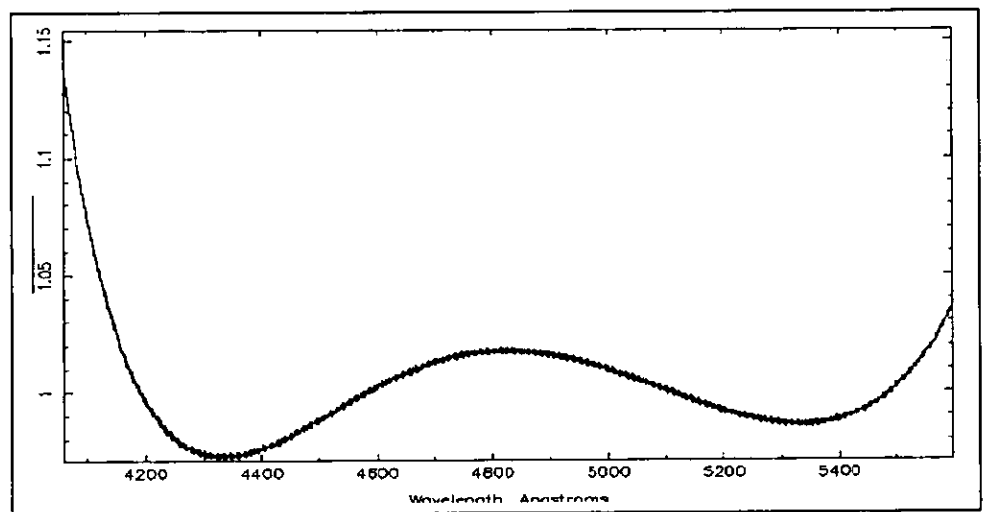


Figure 3.8: Division of normalised smooth interpolations of two spectra; that of the standard flux calibration spectrum of HR 8634 by that of the observed flux calibrated spectrum of HR 8634, giving the wavelength (horizontal axis, in Å) dependant ratio (vertical axis).

Star	Night 1	Night 2	Night 3	S.t.d. (%)
<b>ABSOLUTE</b>				
HR 8634	12.51	19.74	21.47	27
HR 3454	11.07	5.3	N/A	50
<b>NORMALISED</b>				
HR 8634	0.61	0.63	0.63	2
HR 3454	0.64	0.65	N/A	1

Table 3.3: Mean absolute and normalised values for flux calibration stars. Absolute magnitudes have mJy per count, normalised values have no units. The normalised values are from the normalisation of the relevant spectra. The final column is the standard deviation for a given star from night to night, as a percentage.

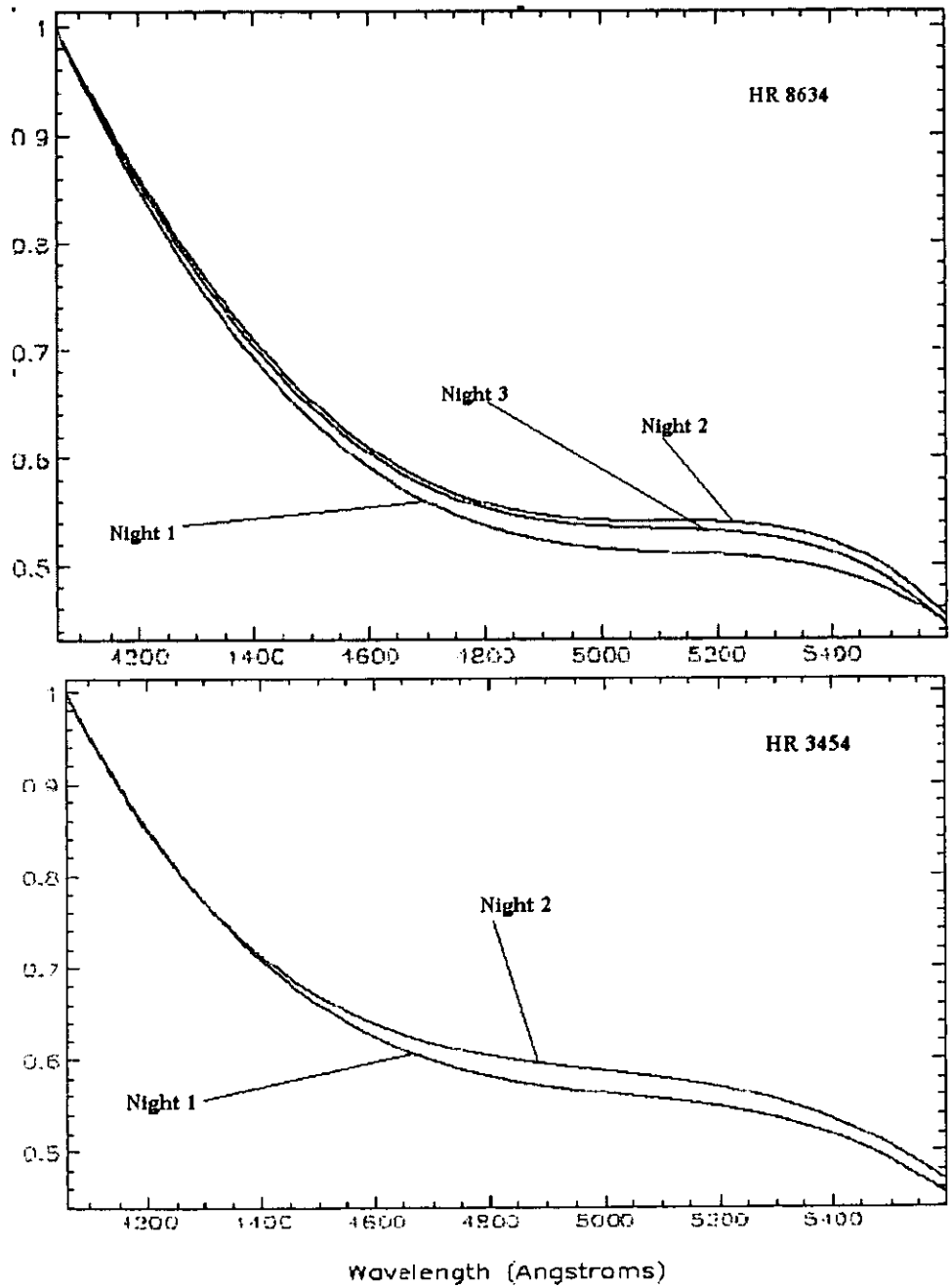


Figure 3.9: Nightly instrumental (normalised by mean) response, for HR 8634 (top) and HR 3454 (bottom), for each night. The instrumental response of each night is labeled. The vertical axis values are unitless.

### 3.4 Preparatory Steps for Measurement of Kinematics

The flux calibrated 2D galaxy spectra contained emission lines in some galaxies. These emission lines were found to impede correct running of velocity dispersion extraction software. The interactive programme FIGARO:CLEAN was used to manually remove emission lines (plus any obvious data reduction artefacts such as CRs) from galaxy images. Figure 3.10 shows the effect of using CLEAN on the spectra of one of the galaxies which most suffered from emission lines.

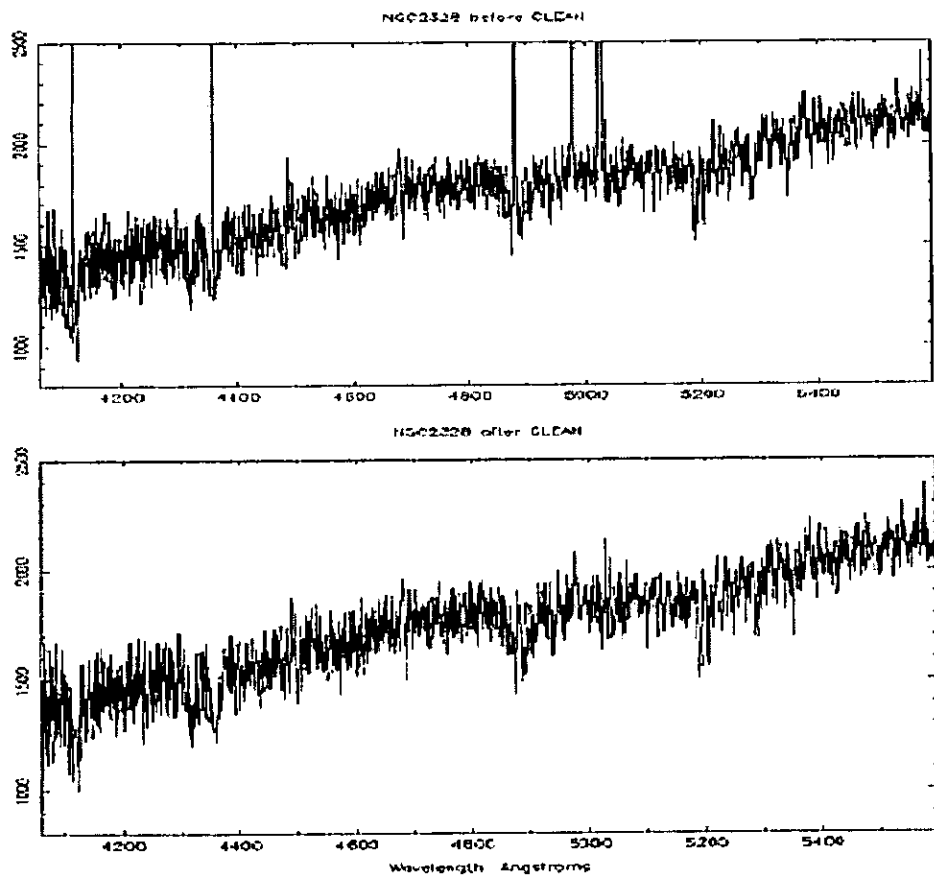


Figure 3.10: Counts (photons) versus wavelength ( $\text{\AA}$ ). Before (top) and after (bottom) using CLEAN (i.e. on NGC 2328) to remove emission lines and residual CRs. In both plots, the vertical axis displays the range from 1000 to 2500 counts, whilst the horizontal axis ranges from 4000 to 5500  $\text{\AA}$ .

A study of IRAF documentation suggested STSDAS:FQUOT, XCOR and also RVSAO:XCSAO as viable programmes for velocity dispersion ( $\sigma$ ) and also redshift ( $z$ ) extraction. Initial data handling of galaxy and Lick star data for this purpose required generation of spectra. For galaxies, this was accomplished by first finding the luminosity weighted positions, about which to extract spectra. The regions of galaxies from which to extract spectra were chosen so as to be consistent with the WHT data set (PS02). This was a region of 3.6'' in the spatial direction of each galaxy image. Galaxy and Lick star spectra were converted from SDF into FITS files using KAPPA:NDF2FITS. Following this, these FITS files were further processed by way of entering their log start wavelength and log wavelengths per pixel (all in Angstroms) into relevant file headers. This was done using IRAF:HSEL and IRAF:HEDIT. This was necessary since the wavelength axis of each image would be lost during format conversion from SDF to IRAF:STSDAS FITS. The wavelength axis of each relevant spectrum was reconstituted by the STSDAS command STRFITS. STRFITS recreates the wavelength axis using the start and end wavelength as noted in the header. Spectra were transformed first to IRAF FITS using IRAF:RFITS then to STSDAS FITS format using STRFITS. Finally, measurement of  $\sigma$  and radial velocities could be attempted, as discussed in section 4.1.

## Chapter 4

# Derivation of Galaxy Kinematics, Line Strengths and Ages

Measurements of galaxy kinematics were necessary for three principal reasons. Firstly, as described in this chapter, so that line strength measurements could then proceed with correct conversion to Lick indices. Secondly, since the galaxy  $\sigma$  (and line strengths measured using  $\sigma$ ) was needed so as to investigate possible correlations between line strength and  $\sigma$ . Lastly, since the line strength measurements could be used as input to galaxy age determining software (written by Proctor, R., 2002, as mentioned in section 2.7, modified by Sansom, A., 2006).

Wherever line strength measurements were made, as discussed in this chapter, the BANSI software was used. This software was initially written by the research supervisor and expanded by Robert Proctor during his PhD. The BANSI software principally measures pseudo equivalent widths, as well as appropriately handling flux calibrations to Lick,  $\sigma$  corrections and errors.

Before galaxy kinematics could be measured (see subsection 4.1.2), the radial velocities of the Lick calibration stars were determined (see subsection 4.1.1). Calibrations to the common scale Lick/IDS system are described in section 4.2. Emission corrections are described in section 4.3. Calibrations to the Lick/IDS system and emission corrections were performed in accordance with the recipe for those processes laid out in PS02.

## **4.1 Measurements of Kinematics**

### **4.1.1 Lick Calibration Star Radial Velocity Measurements**

The calibration to Lick (discussed in section 4.2) required radial velocities of all calibration stars. From experiments with different radial velocity measurement programmes, HCROSS was found to have a relative robustness and consistency in results. HCROSS was therefore selected as the main programme for establishing radial velocities for Lick stars. Barycentric corrections (bc), for comparison to published values, were made using the IRAF programme SkyCalc.

A template star spectrum and the corresponding measured radial velocity were used by HCROSS to set the absolute scale to which the radial velocities of the Lick stars could be determined. The radial velocity of the template star was determined from the mean Doppler shift between expected wavelength positions of atomic lines and measured positions.

The measured positions were found using Gaussian fitting techniques in IRAF:SPLIT, with a standard deviation of about  $4 \text{ km s}^{-1}$ . In comparison to published data, results from HCROSS produced an overall mean difference of about  $-4 \text{ km s}^{-1}$  with a standard deviation of about  $28 \text{ km}^{-1}$ .

The results are shown in Table 4.1. For the Lick stars, published radial velocities were often somewhat dated, being archived in catalogues compiled in the 1950s and 1970s. SIMBAD was found to not give convincing errors for these old data, with values of 1 or 2 in the usual place for errors. The catalogues themselves could not be retrieved by the usual means (such as through the NASA ADS). However, experience with manually finding the position of atomic absorption lines in stellar spectra using IRAF:SPLIT suggests the measurement errors in the published data are not likely to be less than the error in the values found with HCROSS.

Stars	HCROSS (no bc)	HCROSS (bc)	SIMBAD	Difference
HR8841	8.0	-21.4	-26.4	5.0
HR72	-21.7	4.7	-10.7	15.4
HR3845	-3.7	25.5	23.2	2.3
HR203	11.7	-12.9	-12.8	-0.1
HR3994	-4.9	23.2	19.4	3.8
HR4287	26.7	53.5	46.8	6.7
HD219617	95.7	66.2	10.1	56.1
HR296	64.0	40.7	15.3	25.4
HR8924	-17.9	-46.9	-25.0	-21.9
HD211038	26.2	-4.0	11.9	-15.9
HR509	-14.3	-34.1	-16.4	-17.7
HR2574	24.7	40.8	97.3	-56.5
HR2701	16.5	35.3	78.8	-43.5
HR695	28.3	12.1	18.4	-6.3
HR1136	-30.3	-37.5	-6.1	-31.4
HD064606	88.3	111.2	93.4	17.8
			Mean:	-3.8
			S.t.d:	27.5

Table 4.1: Radial velocity measurements of Lick calibration stars compared with published values in SIMBAD. All values have units of  $\text{kms}^{-1}$ . The 2<sup>nd</sup> column is for raw radial velocity measurements. The 3<sup>rd</sup> is after barycentric corrections. Errors on HCROSS measurements are typically of the order of about  $4 \text{ kms}^{-1}$ . No reliable errors are available for the value adopted from SIMBAD.

### 4.1.2 Measurement of Galaxy Kinematics

The radial velocities and velocity dispersions of galaxies were next measured using FQUOT. This programme was selected for a number of reasons. Firstly, because FQUOT achieved results more often than other programmes tried, which tended to produce run time errors or spurious results; for more of the galaxy spectra than FQUOT. FQUOT also usually produced more believable results, closer to published values, than other programmes tried. NGC 1373 had spectra too noisy for FQUOT to successfully extract results. NGC 3125 appeared to have similar problems, though persistency with cleaning spectra may yield results with this galaxy. NGC 1375, as can be seen in Table 4.2, had a particularly large discrepancy measured between  $\sigma$  and the published  $\sigma$  value. The reason for this is unknown. However there is a wide spread of measured  $\sigma$ , measured by

different researchers (i.e.  $56 \text{ km s}^{-1}$  by K000 and  $80 \text{ km s}^{-1}$  by D’Onofrio et al. 1995). This is much greater than associated reported errors (i.e. about 10 sigma). This may simply indicate that reported errors underestimate the true scatter of possible results, about a true mean. Or it may for example indicate systematic differences in measurement techniques. The  $\sigma$  reported in HyperLeda are most often averages, weighted by reported errors. In Table 4.2, redshift ( $z$ ) from SIMBAD and  $\sigma$  from HyperLeda are compared where possible to values measured using FQUOT.

Galaxy	Observed		Published			
	$\sigma$	$z$	$\sigma$	$z$	$\Delta\sigma$	$\Delta z$
NGC 1411	154 (1)	1033 (14)	144 (1)	994 (32)	-10	-39
NGC 2784	236 (2)	704 (3)	225 (9)	704 (6)	-11	0
NGC 59	37 (2)	377 (4)	-	367 (11)	-	-10
ESO 118-34	52 (1)	1118 (3)	-	1164 (23)	-	46
NGC 1331	57 (3)	1204 (20)	55 (5)	1315 (99)	-2	111
NGC 1375	48 (1)	761 (52)	70 (2)	732 (44)	22	-29
NGC1374	160(2)	1360 (21)	178 (5)	1332 (36)	18	-28
ESO 157-30	56 (9)	1537 (15)	44 (11)	1481 (91)	-12	-56
NGC 2328	33 (5)	1127 (2)	-	1159 (-)	-	32
ESO 358-59	51 (4)	1030 (14)	46 (5)	1015 (26)	-5	-15
Mean:					0	1

Table 4.2:  $\sigma$  and  $z$ , as measured for NTT data set, compared where possible with values from HyperLeda and SIMBAD respectively. Units of  $\text{km s}^{-1}$  throughout. Errors are given in brackets. For measured values, the data and errors are as given by FQUOT. The last two columns represent the difference between published and observed values. The mean differences are given on the last row.

The mean differences between observed and published values in Table 4.2 do not show any obvious systematics affecting the observed kinematics. The reason for the difference between published and observed kinematics appears to be simply due to a scatter of results about a true mean. The FQUOT programme uses the “Fourier Quotient Technique” to extract velocity dispersions, as described in Sargent et al. (1977). All descriptions of the methodology of FQUOT given in the following paragraph are based on a study of Sargent et al. (1977).

FQUOT treats the galaxy spectrum as being the convolution of a broadening function and an appropriate template stellar spectrum. The

broadening function is treated as being a Gaussian dispersion, described by a function dependant upon  $\sigma$  and  $z$ . The stellar spectrum is chosen as one which is expected to probably approximate to the galaxy spectrum if the broadening effect of the velocity dispersion in the galaxy spectrum is appropriately accounted for. The velocity dispersion, assuming an accurate redshift estimate, ought then to be solvable by appropriate application of the convolution theorem and solving the broadening function for  $\sigma$ . However, this solution for  $\sigma$  has inherent flaws, due to the assumptions used. The principle flaw is thought to be that the galaxy and star spectrum can not be a perfect match; the broadening function is not then perfectly extracted from the convolution of the galaxy spectrum and the broadening function. The galaxy and star spectrum may have been sampled over finite (and slightly different) ranges, so that a continuous Fourier transform is not possible; a discrete one must be applied. A redshift estimate for the galaxy spectrum is also necessary, which requires in itself a good line match between star and galaxy spectra. FQUOT manipulates the data to make the galaxy and star spectrum as much alike as can be reasonably done, and so that discontinuities in the sampling of spectra may be accounted for.

In short, FQUOT takes discrete Fourier transforms of the (modified) galaxy and star spectra, and then fits a quotient to the Fourier transform of the division of these Fourier transforms (i.e. of the broadening function). From this quotient  $\sigma$  may be calculated given (principally) the appropriate logarithmic redshift estimate. FQUOT, among its input parameters, includes an estimate of the factor  $\gamma$  which FQUOT uses to begin a search for a precise  $\gamma$  value. The  $\gamma$  factor is normalization factor designed to be a measure of the strength of lines in the template spectrum to those of the galaxy spectrum (Sargent et al., 1997, page 3).

The results achieved with FQUOT were initially output as mean values as well as weighted mean values. The spectra of individual galaxies were matched by 3 to 8 different star templates by FQUOT. The matching of templates, either G or K types, to galaxy spectra by FQUOT was not found to be preferential to any spectral type of Lick star.

Since there was no information on the FQUOT manual with regards to the normalizing and flattening of spectra, whether FQUOT actually did this was

not known. FQUOT no longer receives user support, and is not an open source. However, there was not any improvement in result by first normalizing relevant spectra or flattening them by dividing by an appropriate polynomial. Comparing relevant spectra qualitatively in SPLOT, the remaining explanation seemed the most logical one; that both a galaxy spectrum and the relevant template spectrum must remain, despite the effects of noise and line blending, similar enough to remain a close match.

## 4.2 Lick Calibrations

The galaxy spectra required calibration to the resolution of the Lick indices and also corrections for velocity dispersion broadening. This was so as to convert measurements of line-strengths to the Lick/IDS system (Lick indices were discussed in subsection 2.4.2.). Object spectra had to be converted to the Lick scale via correction to zero velocity dispersion and also correction to the Lick/IDS spectral resolution.

Before using the BANSI software to make measurements on the calibration Lick stars, radial velocity corrections were performed on them using FIGARO:ISHIFT (and the relevant values in column 2 of Table 4.1). For all measurements on the NTT data using the BANSI software, the correction to the Lick spectral resolution described in subsection 4.2.1 and 4.2.2 was performed.

### 4.2.1 Correction to Lick Spectral Resolution

To correct the NTT observations to the spectral resolution of the LICK/IDS, the BANSI software was adjusted so as to handle the NTT data set appropriately. The dispersion was set to that of the NTT EMMI instrument (about 0.41 Angstroms per pixel), the Lick spectral resolution,  $\sigma_L$  (given in Table 4.3 below) and the instrumental broadening  $\sigma_I$  (measured as  $\sim 1.83$  Angstroms). The value for  $\sigma_I$  was determined from measurements of the

width of spectral lines (in pixels) in the calibration arc lamp spectra. More than one spectral line was measured, and arc lamps from different times, to check for consistency in  $\sigma_l$ . The measured value for  $\sigma_l$  was then converted into Angstroms ( $\text{\AA}$ ). Those galaxies that have  $\sigma$  less than  $\sigma_L$ , which was all except for the control NGC 2784, had their spectra broadened up to the Lick resolution. This was done by convolution with a Gaussian (by IXSMOOTH, invoked via a script generated by BANSI) of width  $\sigma_B$  given by equation 4.1:

$$\sigma_B = (\sigma_L^2 - \sigma^2 - \sigma_l^2)^{1/2}. \quad (\text{Equation 4.1})$$

However, for NGC 2784, the calibration factor  $C_i$  discussed in section 4.2.2 was implemented by the BANSI software, so as to debroaden the galaxy's spectrum to the Lick resolution.

## 4.2.2 Corrections for Velocity Dispersion Broadening

To test the effect of velocity dispersion broadening, where  $\sigma$  is greater than  $\sigma_L$ , the various Lick star spectra were smoothed (using FIGARO:IXSMOOTH) to varying widths in the range of  $\sigma_c = 0$  to  $300 \text{ km s}^{-1}$ , in intervals of  $20 \text{ km s}^{-1}$ . From these smoothed spectra, correction factors  $C_i(\sigma_c)$  could be determined, following the prescription laid down in Appendix A of PS02. For molecular line-strength indices (i.e. those with units of magnitudes) the correction factor was determined as in equation 4.2:

$$C_i(\sigma) = I_{orig} - I_{\sigma}. \quad (\text{Equation 4.2})$$

Where  $I_{orig}$  is the index value at the calibration resolution and  $I_{\sigma}$  is the index value in the measured broadened spectrum.

For the remaining indices, the correction factor was calculated as in equation 4.3:

$$C_i(\sigma) = I_{orig}/I_{\sigma}. \quad (\text{Equation 4.3})$$

For each of the Lick indices measured  $C_i$  versus  $\sigma_c$  was plotted, as demonstrated in sample plots in Figure 4.1. A 3<sup>rd</sup> order polynomial from each plot was used by the BANSI software to correct the NGC 2784 galaxy

spectrum to the Lick resolution. This calibration to the Lick resolution performed by the BANSI software used equation 4.4:

$$C_i = x_0 + x_1\sigma_C + x_2\sigma_C^2 + x_3\sigma_C^3. \quad (\text{Equation 4.4})$$

Where the  $x_0$  and other coefficients to  $\sigma_C$  are given in Table 4.3 for each index. The value  $\sigma_C$  represents the width of the Gaussian convolved with the star spectrum. The correction factor was applied to index measurements by being added to the equivalent width measurement if units of the index are Å. Where the units of the index are magnitudes, the  $C_i$  was multiplied by the equivalent width measurement.

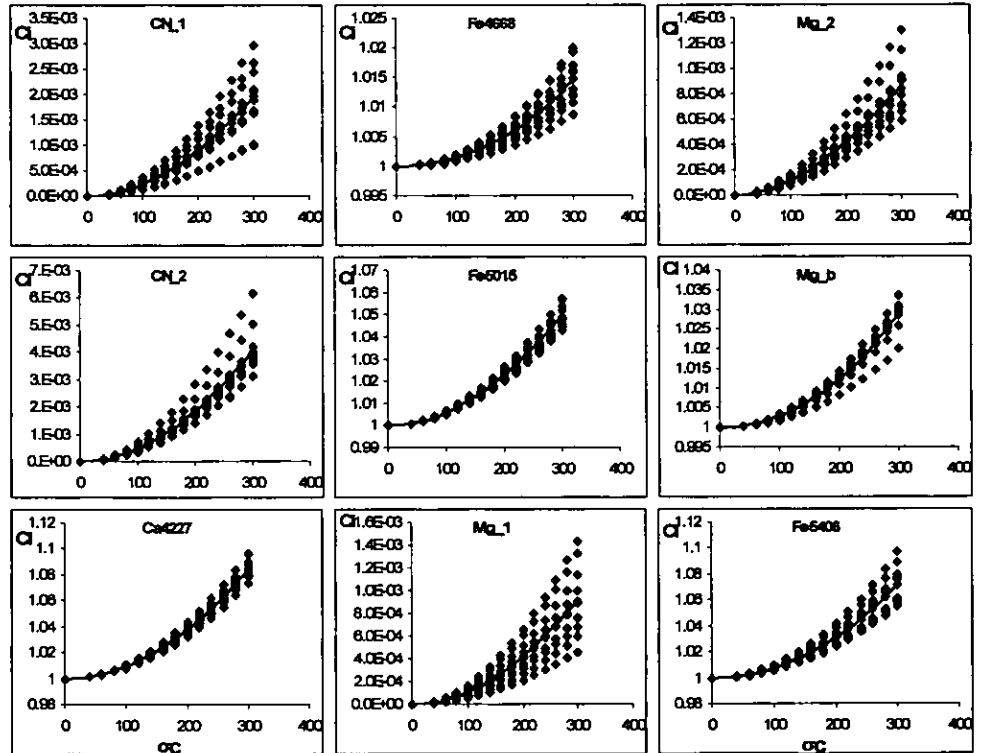


Figure 4.1:  $C_i$  versus  $\sigma_C$ , sample plots. Data points are taken from measurements of  $C_i$  for the Lick star spectra, broadened by different amounts. The best fitting 3<sup>rd</sup> order polynomial for each individual plot can be seen. At  $\sigma_C = 0$   $C_i$  is constrained to 1 or 0, dependant upon how  $C_i$  is to be applied (see main text).

### 4.2.3 Flux-calibration Correction

The published Lick star calibration data set exhibited differences in flux calibration to the NTT data set. This difference between measured and

published values needed to be determined, so as to then perform appropriate corrections for each Index to the Lick flux scale. The BANSI software was run, with the flux-calibration corrections turned off on the calibration Lick star spectra. The result of this run of the BANSI software was to produce the Lick indices of the calibration Lick star spectra, for comparison to published Lick standards to obtain the off-sets. The measured Lick indices were compared to the indices measured by Worthey et al. (1994) and Worthey & Ottaviani (1997) for the same calibration stars. Mean Lick index differences (dl) between the two data sets were calculated for each Lick star spectrum (see Table 4.3). For each Lick index, the BANSI software (with appropriate corrections turned on) performs the flux calibration correction by adding the appropriate dl to the measured equivalent width. The root mean square (RMS) of the differences between measured and published values for each index is given in the final column of Table 4.3, and was used to calculate the error in the calibration to the Lick flux scale (see section 4.4).

Index	$\sigma_L$	$x_0$	$x_1$	$x_2$	$x_3$	dl	RMS
H $\delta$ F	4.64	0	2.81E-05	-2.01E-07	6.69E-10	-0.047	0.446
CN1	4.51	0	-9.97E-08	2.33E-08	-1.27E-11	0.01	0.036
CN2	4.51	0	-1.43E-07	5.02E-08	-1.55E-11	0.013	0.032
Ca4227	4.34	1	-1.07E-06	1.01E-06	-1.23E-10	-0.082	0.316
G4300	4.17	1	-6.71E-07	1.99E-07	-7.84E-11	-0.092	0.394
H $\gamma$ A	4.04	0	-7.81E-10	6.53E-07	-6.64E-06	-0.077	0.934
H $\gamma$ F	4.04	0	3.51E-06	-6.62E-07	3.66E-10	0.12	0.558
Fe4383	3.91	1	-3.29E-07	3.98E-07	4.17E-12	0.207	0.631
Ca4455	3.87	1	-1.07E-06	1.01E-06	-1.23E-10	-0.196	0.284
Fe4531	3.83	1	-5.19E-07	3.69E-07	-8.13E-11	0.434	0.529
Fe4668	3.74	1	6.43E-07	1.44E-07	1.08E-10	-0.001	0.513
H $\beta$	3.61	1	-6.71E-07	1.99E-07	-7.84E-11	0.086	0.17
Fe5015	3.57	1	-1.88E-06	6.27E-07	-2.25E-10	0.105	0.408
Mg1	3.57	0	-3.43E-08	1.15E-08	-3.95E-12	0.005	0.015
Mg2	3.57	0	-6.26E-08	1.21E-08	-9.98E-12	0.002	0.011
Mgb	3.57	1	1.03E-06	2.72E-07	1.68E-10	0.037	0.176
Fe5270	3.57	1	-1.22E-06	5.19E-07	-1.24E-10	0.006	0.204
Fe5335	3.57	1	3.23E-07	8.79E-07	5.35E-11	0.115	0.29
Fe5406	3.57	1	2.22E-06	7.68E-07	2.56E-10	0.08	0.257

Table 4.3: Values for calibration to Lick resolution,  $\sigma_L$ , given for each Lick Index.

Table columns as described in main text.

In Table 4.3, values for  $\sigma_L$  are from Table 2 of PS02. For all indices, the average offset (dl) is given between 13 observed Lick calibration stars and

the corresponding published index values (Worthey et al. 1994 and Worthey & Ottaviani 1997). Units for  $\sigma_L$  and dI and are in Å, except for Mg1, Mg2 and CN1 and CN2 and the Hydrogen indices (which are in mag). The middle 4 columns give the unitless coefficients discussed in subsection 4.2.2. The final column of Table 4.3 is the RMS (in Å), as described in the main text.

### 4.3 Emission Corrections

All of the galaxies in the NTT data set from which kinematics were successfully measured were seen to exhibit some amount of emission. Emission of [OIII]5007 results in line filling in Fe5015. Also, the H $\beta$ , H $\gamma$  and H $\delta$  indices suffer from line filling in galaxies that have emission. To account for this, following the procedure in PS02, each galaxy was divided in turn by individual template star spectra, which were first prepared as described below.

To prepare these templates the Lick star spectra were first, after redshifting with ISHIFT as described in section 4.2, broadened to the  $\sigma$  of individual galaxies (using IXSMOOTH). The templates were normalised to the count level of each galaxy spectrum in turn. The division of galaxy spectra by template spectra was so as to remove the spectral absorption features around the [OIII] line, before measuring the line strength of the [OIII] line.

The [OIII] line's equivalent width was measured appropriately in each galaxy's individual template divided spectrum using the BANSI software. The band definitions as supplied in PS02 were used for this purpose. For each galaxy a mean [OIII] line equivalent width, from the various measurements linked to different template stars, was then calculated. The error pertaining to this [OIII] average was later folded into the error in appropriate line strength measurements of galaxies.

The Lick indices affected by line emission were corrected following the relation proposed by Gonzalez (1993), as was also done in PS02. The

[OIII]5007 emission corrections applied to the Lick indices in question were thus as follows:

$$\text{Fe5015} = -[\text{OIII}], \text{H}\beta = -0.7[\text{OIII}], \text{H}\gamma = -0.7[\text{OIII}], \text{H}\delta = -0.35[\text{OIII}].$$

#### 4.4 Line Measurements and Errors

The BANSI software was set to incorporate the adjustments for calibration to Lick of the NTT data discussed above in section 4.2. The BANSI software was then run on the NTT galaxy data set. Following this the emission corrections were then applied to appropriate indices (in the manner discussed in section 4.3). A sample of errors for these results is given in Table 4.4. The results of the Lick index measurements are detailed in Table 4.5.

Galaxy	CN1	Sky Error	DRError	Lick Error	Combined Error
NGC 2784	0.14	0.07	2.65E-03	0.04	0.08
NGC 59	-0.07	0.07	3.92E-03	0.04	0.08

Galaxy	Fe4668	Sky Error	DRError	Lick Error	Combined Error
NGC 2784	8.84	0.10	0.09	0.04	0.14
NGC 59	0.16	0.10	0.19	0.04	0.22

Galaxy	Mg2	Sky Error	DR Error	Lick Error	Combined Error
NGC 2784	0.340	1.46E-03	9.34E-04	9.17E-04	1.96E-03
NGC 59	0.030	1.46E-03	1.87E-03	9.17E-04	2.55E-03

Table 4.4: Lick Index sample errors corresponding to measurements given in Table 4.5. The 2<sup>nd</sup> column is line strengths; the 3<sup>rd</sup> is error estimated from the sky background subtraction. The 4<sup>th</sup> column is the errors in data after data reductions (aside from sky error). Data reduction errors (column headed “DRError”) are those processes discussed in section 3.2 and 3.3. These are dominated by Poisson noise. The 5<sup>th</sup> column is the standard error in the Lick star data (described further in main text). The last column is the error as a result of all these errors added together in quadrature. Units are in Å for line strength and errors, except for Mg2 which is in mag units throughout.

In Table 4.4, the sky error (as a mean value) and standard error (an RMS value) only differ for Lick indices where some indices are in Angstroms and some in mags. The sky error is a mean value of galaxy Lick index

differences found between index values resulting from different sky selections. The standard error was computed as the  $\text{rms}/[(N-1)^{1/2}]$  (as computed in PS02) where N is the number of Lick calibration stars used, i.e. 13. This final error, calculated from plots of published versus measured line strengths, incorporates error and scatter from both published and measured data sets.

The errors due to Poisson noise appeared to be consistent with the signal to noise estimates previously made for the galaxy spectra. However, the systematic effect of the standard error and sky error led to significant combined errors for the NTT data set (as can be seen in Table 4.5). In some cases, for some galaxies errors were about as large as the measurements. This is markedly so in the low line strength index measurements where systematics may have a more significant affect. This includes the CN1, CN2, Ca4227 and Fe lines (except Fe5335) in particular. The effect of these errors on those indices measured to investigate the thesis motivational questions can be seen Figure 5.1a and Figure 5.1b and Figure 5.2. The effect, if any, on trends discovered or confirmed is part of the discussionary text in Chapter 5.

## **4.5 Galaxy Age Estimates**

In the final stage of this thesis, work was done to estimate galaxy ages. The ages of galaxies in the NTT data set were estimated using the age determining SSP programme (written by Proctor, R., 2002, see section 2.7), modified to handle the NTT data set (private communication Sansom, A., 2006). The NTT data set line strengths were used as inputs to this SSP programme, in accordance with the “Fe-” method in PS02. To evaluate errors, the original line strengths were altered by way of either subtraction or addition of their individual errors. The results stored as error files, one for added error and one for subtracted error. The error files were then used as inputs to the SSP programme. From the deviations from the first set of results with these later two set of outputs, the error in the age estimates for the galaxies was then evaluated. The results are given in section 5.2.

Galaxy	Hdelta_F (A)	CN_1 (mag)	CN_2 (mag)	Ca4227 (A)	G4300 (A)	Hgamma_A (A)	Hgamma_F (A)	Fe4383 (A)	Ca4455 (A)	Fe4531 (A)	Fe4668 (A)	H_beta (A)	Fe5015 (A)	Mg_1 (mag)
ESO 118-34	4.799	-0.1195	-0.077	0.082	-0.153	4.703	4.151	1.347	-0.084	1.807	-0.284	3.139	1.686	0.0227
	0.869	0.0827	0.045	0.158	0.186	0.74	0.871	3.335	0.196	2.471	0.201	0.252	0.419	0.0021
ESO 157-30	2.149	-0.05	-0.0098	0.298	1.607	1.942	2.302	0.315	0.255	2.073	1.504	3.27	2.744	0.0194
	0.877	0.0828	0.0453	0.174	0.186	0.749	0.874	3.339	0.196	2.473	0.247	0.257	0.426	0.0024
ESO 358-59	0.574	-0.0227	0.0198	0.874	4.251	-3.591	-0.191	3.155	0.431	4.275	3.726	2.213	4.503	0.0575
	0.872	0.0827	0.0451	0.163	0.186	0.744	0.871	3.335	0.196	2.471	0.186	0.246	0.405	0.002
NGC1331	1.332	0.0101	0.0513	1.327	5.323	-4.09	0.456	5.274	0.903	3.648	5.338	2.109	5.971	0.0749
	0.877	0.0828	0.0453	0.171	0.186	0.749	0.873	3.336	0.196	2.472	0.205	0.249	0.411	0.0022
NGC 1374	0.376	0.143	0.1875	1.158	6.351	-6.805	-1.747	5.449	1.475	3.982	7.471	1.66	6.467	0.1699
	0.87	0.0826	0.0449	0.153	0.186	0.739	0.871	3.332	0.196	2.469	0.126	0.246	0.393	0.0016
NGC 1375	1.088	-0.0307	0.0023	1.218	4.632	-4.01	-0.493	4.428	1.131	4.175	4.378	2.574	5.463	0.0607
	0.879	0.0828	0.0453	0.17	0.186	0.75	0.874	3.336	0.196	2.471	0.2	0.251	0.408	0.0021
NGC 1411	0.164	0.0988	0.138	1.066	5.479	-5.905	-1.371	5.494	1.236	3.786	7.141	1.806	5.229	0.1272
	0.868	0.0826	0.0449	0.152	0.186	0.737	0.869	3.332	0.196	2.469	0.122	0.24	0.388	0.0016
NGC 2328	2.086	-0.052	-0.0298	0.148	0.888	1.441	2.138	0.984	-0.056	1.728	0.193	1.31	2.532	0.0308
	0.869	0.0827	0.0449	0.156	0.186	0.739	0.87	3.334	0.196	2.47	0.172	0.246	0.402	0.0019
NGC 2784	-0.386	0.1436	0.192	1.462	5.69	-7.146	-2.175	6.362	1.502	4.201	8.84	1.833	5.583	0.1749
	0.871	0.0827	0.045	0.156	0.186	0.742	0.872	3.333	0.196	2.47	0.143	0.247	0.396	0.0017
NGC 59	3.602	-0.0737	-0.0487	0.108	-0.308	3.361	3.176	1.25	-0.36	1.328	0.156	1.946	0.857	0.0258
	0.873	0.0827	0.0451	0.166	0.186	0.745	0.873	3.336	0.196	2.472	0.221	0.259	0.449	0.0023

Galaxy	Mg_2 (mag)	Mg_b (A)	Fe5270 (A)	Fe5335 (A)	Fe5406 (A)	OIII (A)
ESO 118-34	0.0639	1.139	0.912	0.799	0.674	-0.159
	0.0024	0.097	0.094	0.095	0.512	-0.006
ESO 157-30	0.0679	1.009	1.245	0.692	1.158	-0.407
	0.0027	0.108	0.106	0.108	0.513	-0.035
ESO 358-59	0.1632	2.964	2.551	2.515	1.317	-0.001
	0.0023	0.089	0.081	0.076	0.51	0.007
NGC1331	0.1736	2.71	2.552	2.251	1.677	-0.122
	0.0025	0.096	0.09	0.089	0.511	-0.007
NGC 1374	0.3281	5.069	2.792	2.684	2.224	-0.681
	0.0018	0.071	0.054	0.037	0.508	-0.055
NGC 1375	0.1887	2.799	2.707	2.57	1.682	0.249
	0.0024	0.093	0.085	0.082	0.51	0.044
NGC 1411	0.2579	4.212	2.959	3.093	1.675	0.044
	0.0018	0.07	0.053	0.035	0.508	0.012
NGC 2328	0.0759	1.407	1.342	1.174	0.92	0.021
	0.0022	0.086	0.077	0.072	0.51	0.005
NGC 2784	0.3418	4.992	3.301	2.7	2.064	0.275
	0.002	0.075	0.06	0.047	0.508	0.052
NGC 59	0.032	0.51	0.692	0.703	0.888	0.117
	0.0025	0.101	0.1	0.102	0.512	0.006

Table 4.5: Lick Index Measurements of the NTT data set. Errors are given on the 2<sup>nd</sup> row corresponding to each galaxy. The Fe5015, H $\beta$ , H $\gamma$  and H $\delta$  Lick Index values given here are after the appropriate emission corrections discussed in section 4.3.

# Chapter 5

## Analysis of Results

Measurements of the Lick Indices are here studied in terms of their correlations with  $\sigma$ , as given in tables and shown in plots of Indices versus  $\sigma$  in section 5.1. All measurements of indices are after conversion to the Lick/IDS system (detailed in Chapter 4). In section 5.2 the ages of galaxies are tabulated and briefly discussed. In section 5.3 some conclusions from results and possible implications for galaxy formation scenarios are discussed.

### 5.1 Line Strength versus Velocity Dispersion

This section investigates whether possible correlations between line strengths and  $\sigma$  could be verified by extending the range of  $\sigma$  into low  $\sigma$  in relevant plots. To this end the WHT data was arranged in plots of line strength versus  $\log(\sigma)$  with the NTT data. These plots are shown for predominantly Z sensitive indices versus  $\log(\sigma)$  in Figure 5.1a and Figure 5.1b and for predominantly age-sensitive indices versus  $\log(\sigma)$  in Figure 5.2.

In Figure 5.1a and Figure 5.1b can be seen that one data point in particular, that of NGC 1375, strays often high above the relevant trend lines. However, the spectrum of NGC 1375 was not particularly noisy (S/N of  $\sim 89$ ) nor was it particularly affected by emission. Neither did NGC 1375 appear to be particularly strong (or weak) lined galaxy in comparison to the other galaxies in the NTT data set. Confidence in the trend lines as correlation functions for each of the line-strengths versus  $\log(\sigma)$  in Figure 5.1a and Figure 5.1b and Figure 5.2 is represented by the coefficient of determination ( $R^2$ ) and Pearson's  $r$ . These values are given as appropriate in this Chapter's tables. In Table 5.1 correlations are given for WHT early-type galaxies. In Table 5.3 similar correlations are given for the WHT late-type galaxies. In both of these tables, correlations are made which investigate the

effect on correlations of correlating the NTT data set with the relevant WHT data.

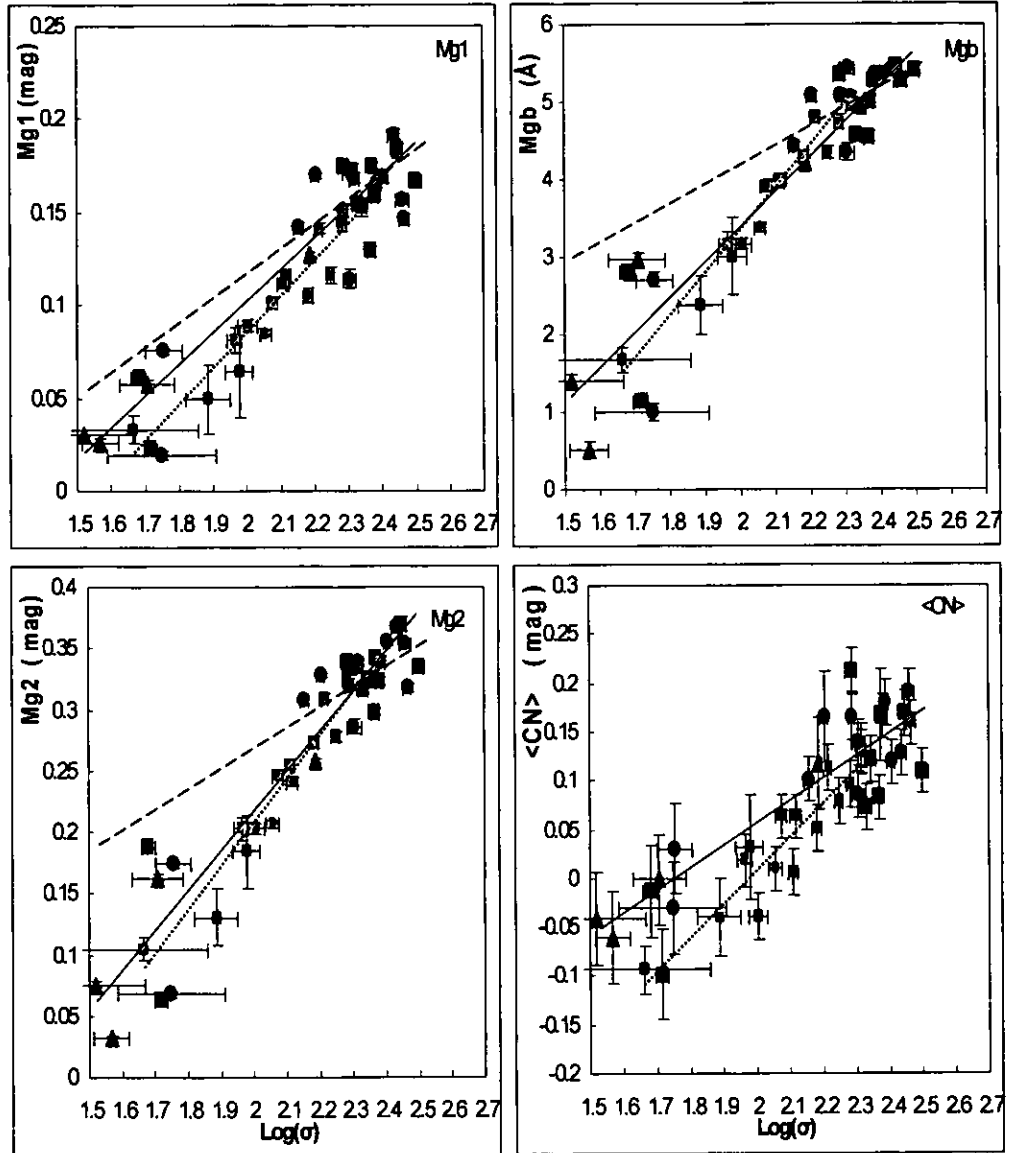


Figure 5.1a: Predominantly Z-sensitive Lick indices plotted against  $\text{log}(\sigma)$ . The units of  $\sigma$  are  $\text{kms}^{-1}$ ; those of the Indices are given on the plots. The black dotted trend lines are fits to the spiral bulge data (all of which are from the WHT data set). The solid lines are fits to the early-type galaxies (WHT + NTT data). The blue data points (circle for E, square for SO, triangle for E-SO) are from the NTT data set. Green data points are early-type galaxies (circle for E, square for SO) from the WHT data set. Red data points are late-type galaxies (circle for SO/a, square for spirals). The dashed blue lines are those for early-types from K000, extended from the original range ( $\sim 79$  to  $\sim 398 \text{ kms}^{-1}$ ) to low velocity dispersions for comparison purposes. In the top right hand corner of each plot, the relevant Lick Index is noted.

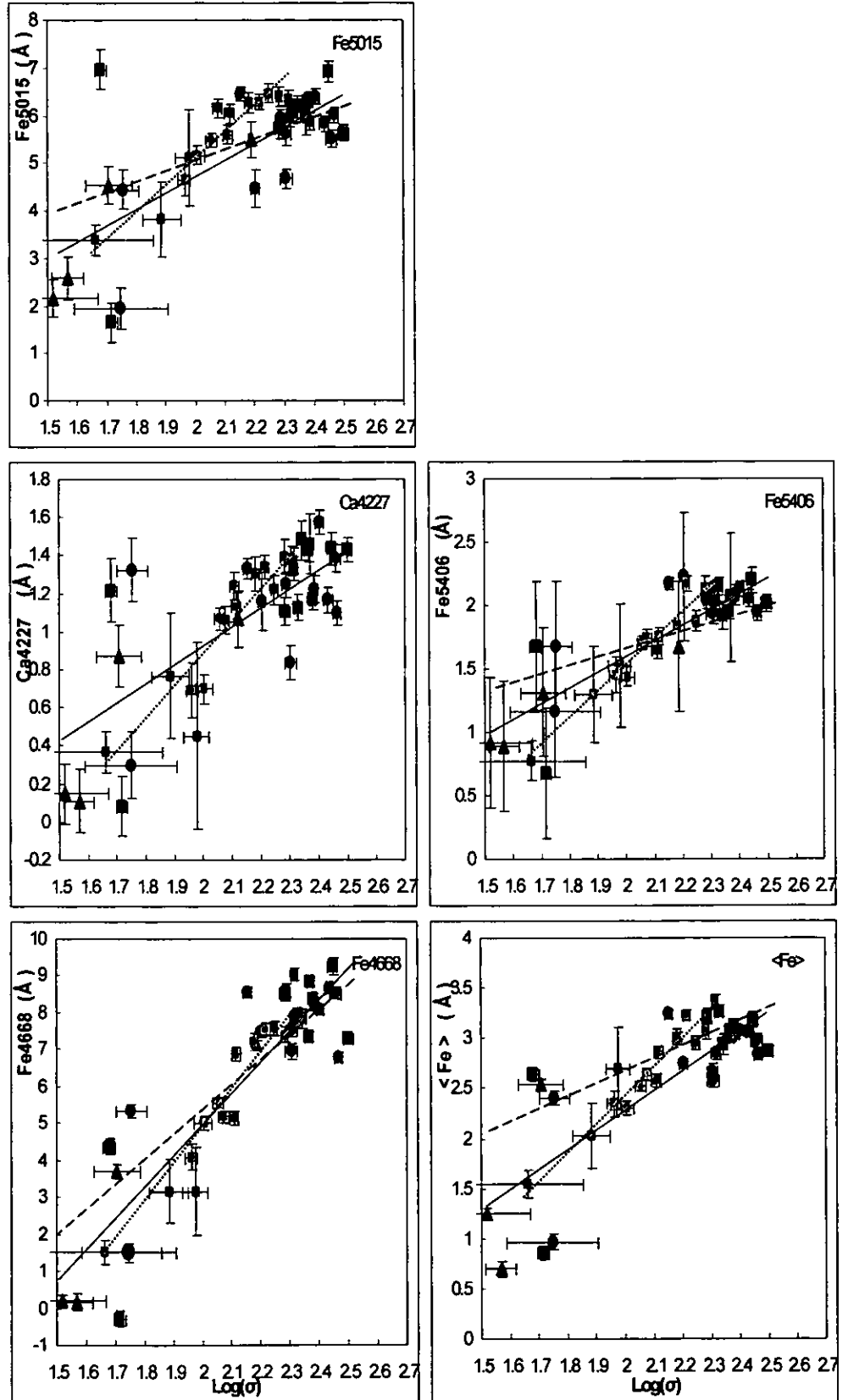


Figure 5.1b: Predominantly Z-sensitive Lick indices plotted against  $\text{log}(\sigma)$ . Trend-lines and data-point symbols are here as described in Figure 5.1

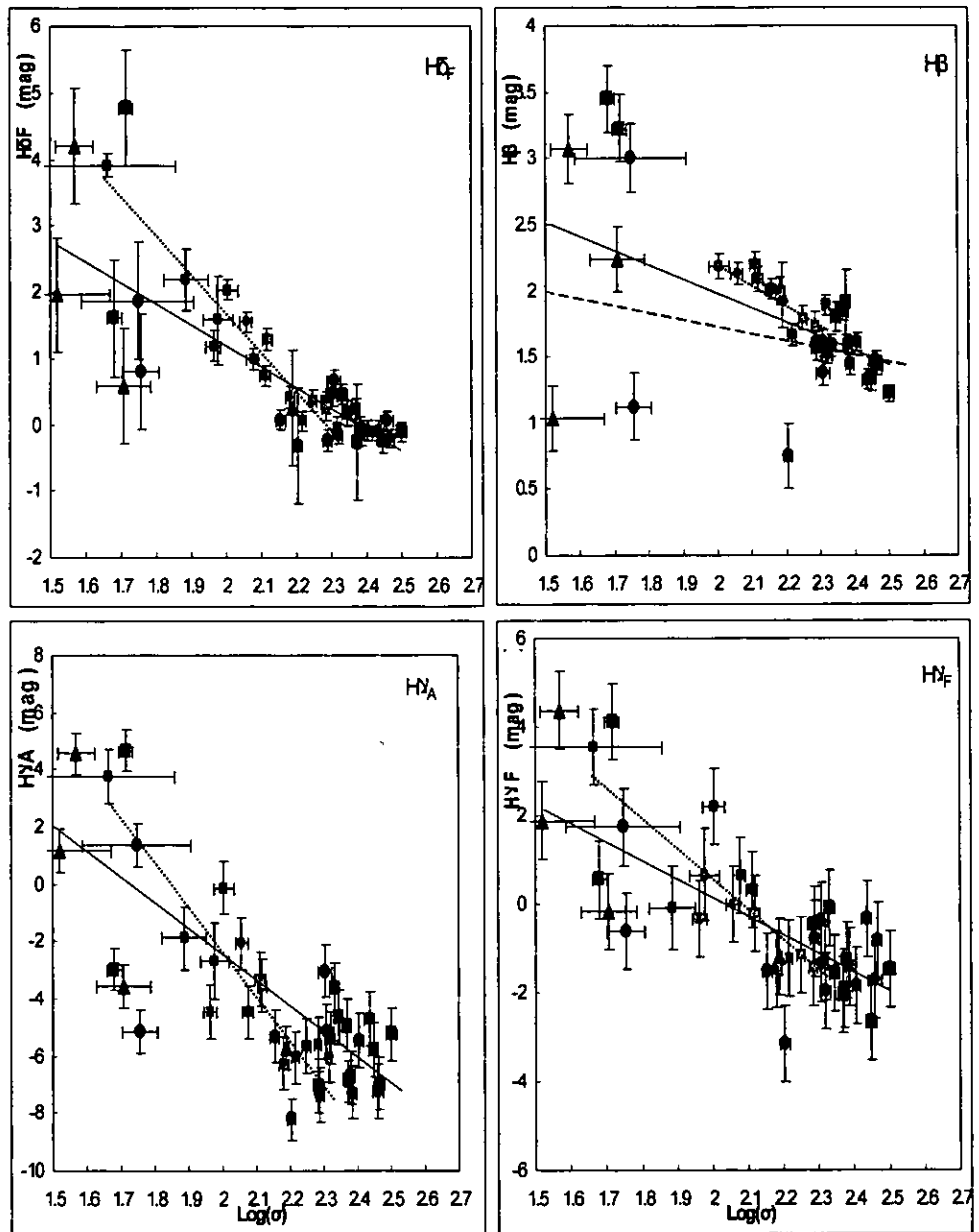


Figure 5.2: Predominantly age sensitive indices versus  $\log(\sigma)$ . Trend-lines and data-point symbols are here as described in Figure 5.1a

Though for simple linear regressions,  $R^2$  is simply the square of Pearson's  $r$ ,  $R^2$  remains such a common measure of goodness of fit in statistics, for such plots as in this Chapter, to be worth inclusion in Table 5.1.  $R^2$  is here the fraction of the varying Lick index axis values that are explained by the

linear regression (from the Annotated SPSS Output Regression Analysis URL; [http://www.ats.ucla.edu/STAT/SPSS/output/reg\\_spss.htm](http://www.ats.ucla.edu/STAT/SPSS/output/reg_spss.htm)).

The Pearson's  $r$  values, such as were used in PS02, are included for completeness and so as to provide the sense of trends. Each correlation is deemed significant where the corresponding Pearson's  $r$  is above the 1% level of significance for a two-tailed test (see Appendix C for table of critical values for Pearson's  $r$ ). The correlations for the late-type galaxies can be found reproduced from PS02 in Table 5.3. Note the Figure 4 from PS02 reproduced in Chapter 1 included NGC 4313, whereas NGC 4313 was not included in correlations in table 5 of PS02. NGC 4313 therefore was excluded here from relevant plots and Table 5.1.  $\chi^2$  was not included in Table 5.1 since the errors in the plots (i.e. Figures 5.1 and 5.2) do not follow a Gaussian distribution (see Sivia, 1996, p.88). In Table 5.2, for completeness of results and separate from Table 5.1 for the sake of clarity, is given Pearson's  $r$  and also  $R^2$  for Lick indices, calculated for the NTT data set only.

Index	m	c	r	$R^2$	r (WHT)	$R^2$ (WHT)
Ca4227	1.04	-1.16	0.75	0.57	0.21	0.04
Fe4668	8.23	-11.4	0.9	0.81	-0.12	0.01
Fe5015	3.44	-2.24	0.73	0.53	0.02	0
<Fe>	1.92	-1.53	0.8	0.64	-0.19	0.04
Fe5406	1.21	-0.8	0.86	0.74	-0.21	0.04
<CN>	0.24	-0.42	0.88	0.78	0.21	0.04
Mg1	0.16	-0.23	0.93	0.87	0.35	0.12
Mg2	0.31	-0.41	0.94	0.89	0.51	0.26
Mgb	4.66	-5.93	0.94	0.88	0.61	0.37
H $\delta$ F	-3.16	7.48	-0.78	0.61	-0.43	0.18
H $\gamma$ A	-8.26	13.64	-0.76	0.58	-0.19	0.04
H $\gamma$ F	-4.37	8.92	-0.76	0.58	-0.21	0.04
H $\beta$	-1.23	4.45	-0.57	0.32	-0.71	0.50

Table 5.1: Correlations between Lick indices and  $\log(\sigma)$ , for the LLEs and WHT early-type galaxies. Number of galaxies used to form these values is 10 from the NTT data set, 17 from the WHT data set. Table columns described in main text.

In Table 5.1 columns are firstly index, gradient and intercept; for combined data sets. The (un-weighted) Pearson's  $r$ , followed by

corresponding  $R^2$ , for the WHT and NTT combined data set follows. Pearson's  $r$  for the WHT data-set alone (from PS02) follows, in the third column of Table 5.1, with corresponding  $R^2$ , in subsequent columns. All correlations are statistically significant (see appendix C); Levels of statistical significance are  $R^2$  of 0.548, 0.412 and 0.323, for the NTT data set, WHT early-type data set and combined data sets respectively.

Index	$r$ NTT only	$R^2$ NTT only
Ca4227	0.68	0.56
Fe4668	0.88	0.81
Fe5015	0.53	0.53
<Fe>	0.71	0.64
Fe5406	0.88	0.74
<CN>	0.93	0.77
Mg1	0.94	0.86
Mg2	0.9	0.88
Mgb	0.88	0.88
H $\delta$ F	-0.68	0.61
H $\gamma$ A	-0.76	0.58
H $\gamma$ F	-0.77	0.58
H $\beta$	-0.36	0.13

Table 5.2: Correlations (Pearson's  $r$  and also  $R^2$ ) for Lick indices, calculated for the NTT data set alone, given here separately to Table 5.1 for clarity. All values are statistically significant ( $R^2 > 0.549$ ) except for that of H $\beta$ .

In Figure 5.1a, Figure 5.1b and Figure 5.2 the lines of best fit are very close to one another. The question of whether the LLEs compare well with the late-type galaxies in the WHT data set was quantitatively investigated. This was by way of performing correlations of  $\sigma$  versus line strength for various Lick indices using the NTT data set combined with the WHT late-type galaxies. The correlations found are given in Table 5.3.

Table 5.3 is similar to Table 5.1, except that the correlations from combining data sets are a result of NTT galaxies fit simultaneously with the WHT late-types. The last two columns of Table 5.3 are for the WHT late-type galaxies only. All correlations in Table 5.3 are statistically significant (i.e.  $R^2$  greater than 0.548, 0.412 and 0.323, for the NTT data set, WHT late-

type data set and combined NTT and WHT early-type data sets respectively).

Index	m	c	r	R <sup>2</sup>	r (WHT)	R <sup>2</sup> (WHT)
Ca4227	1.36	-1.78	0.77	0.59	0.90	0.81
Fe4668	9.89	-14.72	0.91	0.83	0.96	0.92
Fe5015	4.50	-4.02	0.74	0.54	0.95	0.90
<Fe>	2.48	-2.52	0.82	0.68	0.96	0.92
Fe5406	1.51	-1.42	0.86	0.74	0.97	0.94
<CN>	0.25	-0.47	0.85	0.72	0.91	0.83
Mg1	0.18	-0.26	0.92	0.85	0.94	0.88
Mg2	0.34	-0.46	0.93	0.86	0.97	0.94
Mgb	4.95	-6.53	0.93	0.86	0.98	0.96
H $\delta$ F	-4.00	9.25	-0.75	0.56	-0.95	0.90
H $\gamma$ A	-11.28	19.49	-0.78	0.62	-0.88	0.77
H $\gamma$ F	-5.73	11.60	-0.76	0.58	-0.84	0.71
H $\beta$	-1.02	4.13	-0.39	0.16	-0.81	0.66

Table 5.3: Correlations between Lick indices and  $\log(\sigma)$ , for the NTT data set and the 15 late-type WHT galaxies used in PS02 for correlations. Columns as described in text.

## 5.2 Galaxy Ages

The ages of galaxies, estimated using SSP software as described in section 4.5, are given here in Table 5.4. For completeness, the  $[\text{Fe}/\text{H}]$  values for these galaxies from the same SSP software are also included in Table 5.4. For the NTT data, correlations were also made of  $\log(\text{Age})$  and also  $[\text{Fe}/\text{H}]$  against  $\log(\sigma)$ , as given in Table 5.5.

In Figure 5.3, galaxy ages are plotted versus  $\sigma$ , for the NTT and WHT data sets. The ages for the WHT galaxies were taken from Table 10 of PS02. In Figure 5.4,  $[\text{Fe}/\text{H}]$  is plotted against  $\log(\sigma)$ . In Figure 5.5,  $[\text{Fe}/\text{H}]$  is plotted against  $\log(\text{Age})$ .

Galaxy	Log( $\sigma$ )	Log( $\sigma$ ) Error	Log(Age)	Log(age) Error	[Fe/H]	[Fe/H] error
ESO11834	1.716	0.019	0.275	0.025	-1.3	0.075
ESO15730	1.748	0.161	0.65	0.075	-1.25	0.125
ESO35859	1.708	0.078	0.7	0.1	-0.25	0.1
NGC1331	1.756	0.053	0.4	0.056	0.2	0.075
NGC1374	2.204	0.013	1	0.006	0.15	0.0
NGC1375	1.681	0.021	0.4125	0.056	0.15	0.075
NGC1411	2.121	0.006	0.6	0.0	0.25	0.0
NGC2328	1.519	0.152	1.225	0.263	-1.4	0.075
NGC2784	2.373	0.008	0.8	0.13	0.325	0.013
NGC59ef	1.568	0.054	0.6375	0.044	-2	0.1

Table 5.4: NTT data set ages, and [Fe/H]. Units are  $\text{kms}^{-1}$  for  $\sigma$  and Gyr for Age.

	m	c	r	R <sup>2</sup>
Log(Age)	0.148	0.397	0.148	0.0220
[Fe/H]	2.086	-4.349	0.686	0.471

Table 5.5: Correlations with  $\log(\sigma)$  against  $\log(\text{Age})$  and also [Fe/H], for NTT data set. Only the  $\log(\sigma)$  versus [Fe/H] correlation is significant. Units for Age, as relevant to the 3<sup>rd</sup> column, are Gyr.

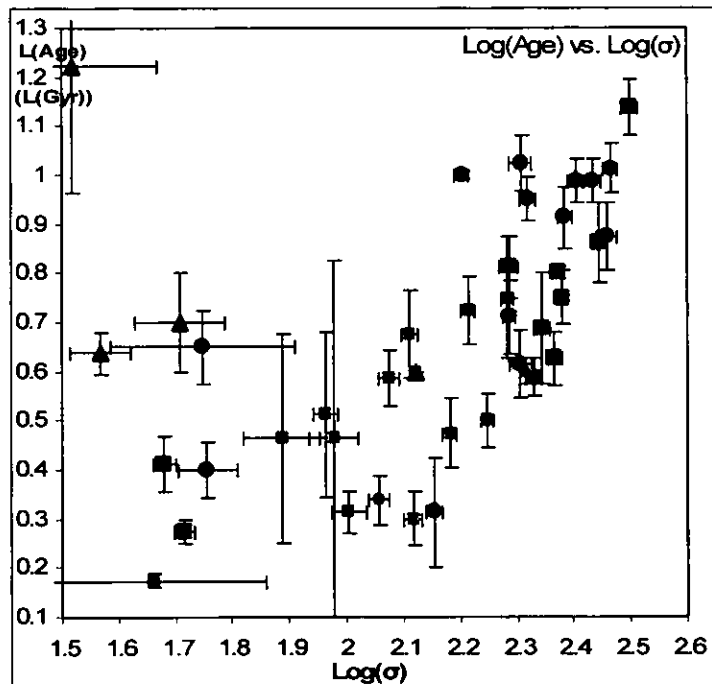


Figure 5.3: Log(Age) versus Log( $\sigma$ ), of NTT and WHT data sets. The units of  $\sigma$  are  $\text{kms}^{-1}$ ; those of Log(Age) are Log(Gyr). Colours of data points are as in Figure 5.1a; blue data points are from the NTT data set, red are from the WHT data set late-types, green are from the WHT data set early-types.

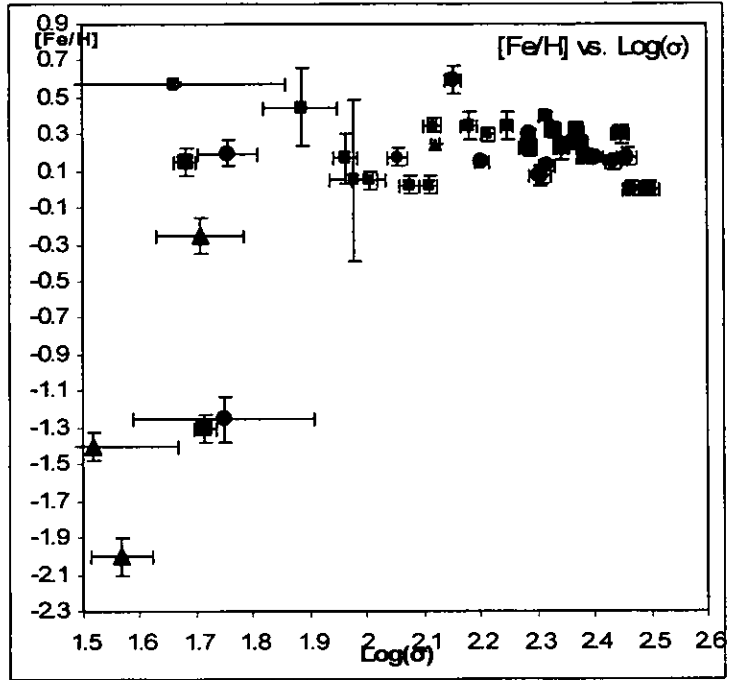


Figure 5.4:  $[\text{Fe}/\text{H}]$  versus  $\text{Log}(\sigma)$ , of NTT and WHT data sets. The units of  $\sigma$  are  $\text{kms}^{-1}$ . Colours of data points are as in Figure 5.1a.

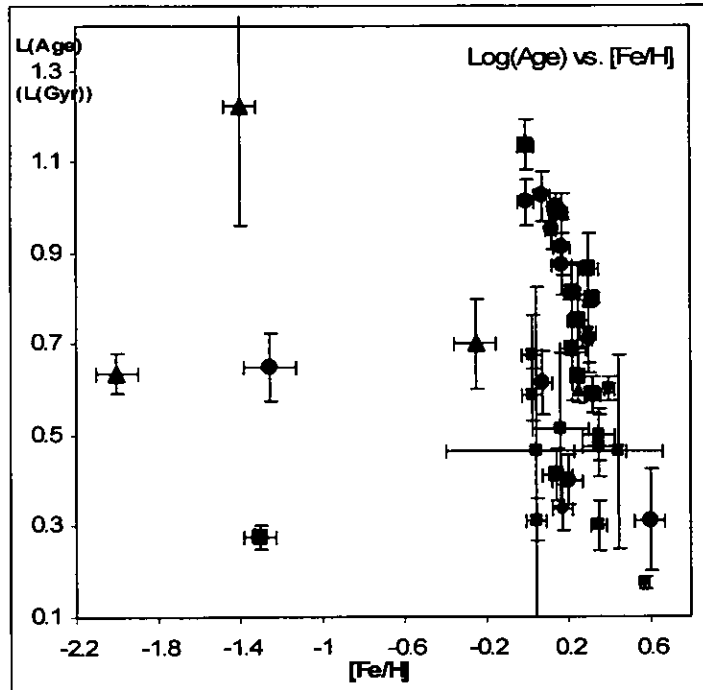


Figure 5.5:  $[\text{Fe}/\text{H}]$  is plotted against  $\text{Log}(\text{Age})$ . Units of  $\text{Log}(\text{Age})$  are  $\text{Log}(\text{Gyr})$ .

### 5.3 Discussion of Results

As mentioned in section 1.3, earlier work involving the WHT data alone left some claims to possible trends in the data uncertain due to the narrowness of the range in  $\sigma$  measured for the WHT data set. The correlations quantified in Table 5.1 show trends of line strengths with  $\sigma$ , which are statistically valid at the 1 % level of the two tailed test. However, the scatter of data points about the trend lines seen in Figure 5.1a, Figure 5.1b and Figure 5.2 suggest unaccounted for variables affect the correlations. The relatively high scatter of line strengths versus  $\sigma$  in the NTT data set compared with the higher  $\sigma$  WHT data set is apparent (see Figure 5.1a, Figure 5.1b and Figure 5.2). This is qualitatively similar to what was found in CRC03, where the low  $\sigma$  galaxies had a great scatter in correlations of line strengths versus  $\sigma$  (see Figure 1.2). Where the “high level” of scatter of line strengths versus  $\sigma$  is apparent in the plots shown in Figure 5.2, this may be indirectly indicative of a scatter in ages at low  $\sigma$ , supporting the result claimed by CRC03.

The correlations (reported in Table 5.1) for the combined early-type and LLE Z sensitive line strengths versus  $\sigma$  show statistically “good fits”. The correlation was made poorer however for the H $\beta$  line strength versus  $\sigma$  correlation by inclusion of the NTT data set H $\beta$  line strengths. This may be simply due to there being a poor correlation of the H $\beta$  line strength with  $\sigma$  for the NTT data set (as shown in Table 5.2). The correlations strengthened by the NTT data set for the other age sensitive indices however are qualitatively suggestive of a correlation of increasing age (or decreasing Z) with  $\sigma$  in the early-type galaxy data sets. However, as can be seen in Table 5.5, the correlation between age and  $\sigma$  for the NTT data set is very poor. Examining Figure 5.3 qualitatively, the NTT data set’s ages would appear to be at about the same level as those of the WHT late-types, with the exception of the E-SO LLE NGC 2328. In regards to the [Fe/H], about half the sample would appear to have very much lower Z than the other half (as can be seen in Figure 5.4). This apparent result is considered further in Chapter 6; in the speculative discussion of section 6.2, in regard to dSph galaxies.

The correlations found for line strengths versus  $\sigma$  mentioned above, are not better than those found when linking the NTT data set with the WHT late types (see Table 5.3). The question of whether LLEs are more closely correlated in line strength versus  $\sigma$  to spiral bulges (SBs) than to early-types is here addressed. Figure 5.1a and Figure 5.1b show the blue-dashed trend lines found by K000, extended to the low  $\sigma$  values typical of the NTT data set. The blue-dashed trend lines at low  $\sigma$  are at typically higher equivalent width values than the NTT data.

The NTT data can be seen from Figure 5.1a and Figure 5.1b to be not compatible with the extension of the K000 lines. The NTT data do however comfortably share the trend line of the WHT SBs, as seen in Figure 5.1a, Figure 5.1b and Table 5.3. In conjunction with this observation, quantitatively, in Table 5.3, the correlations for the WHT late-types are not improved by simultaneous fitting with the NTT data set. They are made poorer. Interestingly, the correlations shown in Table 5.3 column 5 are very much akin to those in Table 5.1 column 5. However, the correlations in Table 5.1 assume that the extrapolation of the K000 trend lines is wrong and that the NTT LLEs actually belong to a different set of trend line extrapolations (i.e. the trend lines for early-types plotted in Figure 5.1a and Figure 5.1b). To remain in accord with K000, the early-type trend lines in Figure 5.1a and Figure 5.1b should be false. A thorough testing of the trend lines above would require more observations at intermediate  $\sigma$  of early-type galaxies.

Comparing the results of this Chapter to those found in Poggianti et al. (2004 and 2001) appropriately, some interesting apparent parallels between results were identified. Poggianti et al. (2001) examined a large sample of dwarf and giant galaxies between -20.5 and -14 in  $M_B$ , from which Lick indices were extracted and ages and metallicities derived. Throughout the data set of the Poggianti et al. (2001) paper, the Z sensitive Lick indices increase, and age-sensitive decrease, with respect to luminosity. This is qualitatively as found for the WHT data set; if the assumption that increasing luminosity is positively correlated with increasing  $\sigma$  is made. Yet for the low  $\sigma$  LLEs of the NTT data set such a statement can only be extended to the metallicity sensitive Lick indices (see Table 5.5). The NTT data set

galaxies largely scatter in Figure 5.3 about the ages of about 2 to 6 Gyr (with the outlier NGC 2328 at  $16.8 \pm 1.83$  Gyr). Poggianti et al. (2001) found a broader range of ages, from younger than 3 Gyr to older than 9 Gyr at all magnitudes (i.e. including dwarfs). Were Poggianti et al. (2001) to correlate age sensitive Lick indices with Luminosity for the dwarfs in their sample alone, the natural expectation from Table 5.5 and Figure 5.3 is that they would find little or no correlation.

Poggianti et al. (2001) found metallicity to increase with Luminosity, with a particularly high scatter where faint galaxies are concerned; which may be qualitatively similar to what can be found in Figure 5.4, following the above arguments. The results of Poggianti et al. (2001) became particularly interesting when considering their finding regarding correlations between metallicity and age; in regards to “faint” galaxies (with ages  $< 3$  Gyr and possibly those of 3-9 Gyr) they found that their data could be separated into a metal poor and metal rich group ( $Z$  about -1.5 and 0 respectively). Qualitatively, this result matches the one mentioned above for the NTT data set, as can be seen in Figure 5.4. Poggianti et al. (2001) ascribe to the dwarf galaxies in their data set ages of  $< 3$  Gyr with errors of  $\pm 2$  Gyr. If errors are taken into account the dwarf galaxies Poggianti et al. (2001) observe can not be said to be definitively younger than the older metal rich LLEs in the NTT data set.

Poggianti et al. (2001) suggest two distinct paths of galaxy formation for the “faint” galaxies in their sample. Poggianti et al. (2004) further investigate the apparent separation between the metal rich and metal poor faint galaxies in their data set. This includes the use of the Mg Lick indices to distinguish between metal poor and metal rich faint galaxies; such a separation as the Mg indices indicate in the Poggianti et al. data can also be qualitatively found in the NTT data (by way of comparing carefully data point symbols in Figure 5.4 and Figure 5.1a). In Poggianti et al. (2004), initial observations and results are mentioned to produce higher signal-to-noise data to test more strongly for a “bimodal distribution” in their data set of faint galaxies; they were however limited by bad weather in the number of galaxies and line strengths they might investigate. The large number of Lick indices observed in good signal to noise spectra, used to determine (amongst

other things)  $[Fe/H]$  for this thesis provides strong evidence for such a bimodal distribution. Poggianti et al. (2004) suggest possible formation mechanisms that could explain the separation of faint galaxies in their sample, and also therefore perhaps LLEs in the NTT data set, according to their metallicities. Their first two suggestions were found to be in agreement with the suggestions that were made as to the formation of the metal rich (as high  $Z$  LLEs) and metal poor (as low  $Z$  LLEs) faint galaxies in section 6.2.2.

Interestingly, studies made of the Sloan Digital Sky Survey (SDSS) data do not appear to find such bimodal distributions for faint galaxies, which could be due to sample selection effects (private communication, Proctor, R., 2006). The faint, or low  $Z$  LLEs, discussed here may well be usually of apparent magnitudes too low for them to be readily “netted” by the SDSS; for the SDSS data, magnitude limits are at about 22.2 (from the SDSS web page “<http://www.sdss.org>” at extension “/dr4/”), at wavelengths comparable to those of spectra used in this thesis (see Table 3.1).

Due to previous bad experience with web site information, and the size of the SDSS survey, a paper that takes a large sample from the SDSS survey was examined; Heavens et al. (2004) in their study of a large sub-sample of local Universe SDSS data use galaxies of (red) apparent magnitudes in the range 15.0 to 17.77, with a mean redshift of 0.1 (much greater than  $z$  of galaxies in the NTT data set). Using  $H_0 = 71 \text{ kms}^{-1} \text{ Mpc}^{-1}$  (Spergel et al. 2003), and using the standard equations for absolute magnitude and Hubble’s law (Carroll and Ostlie 1996, p. 67 and p.1267 respectively), and mean apparent magnitude of about 16.4, this gives a mean absolute magnitude of -21.7. Even the high  $Z$  LLEs from the NTT data set, which are brighter than the low  $Z$  LLEs, can be expected qualitatively speaking from these figures to be fainter at absolute magnitudes than galaxies in the Heavens et al. (2004) sample; this is assuming that most galaxies in the Heavens et al. data set will not be significantly brighter in red than bolometric magnitudes. However, since bolometric magnitudes were not given in Heavens et al. (2004) nor have been identified on the SDSS URL for their data set, a thorough quantitative comparison was not possible. A further complication was found from the SDSS URL (extension “/dr1”) in

that the magnitude model for data release 1 (as used by Heavens et al. 2004) was faulty. Later data releases have this problem apparently resolved, but in any case no papers from the SDSS survey were found concerning what could be faint enough to be a group of faint dwarf galaxies or LLEs.

Heavens et al. (2004) find that age is negatively correlated with mass for the galaxies in their sample. This is quite different to what might be expected from considering the WHT (early-types in particular) data in Figure 5.3. There is no evidence for “downsizing” in regard to the low  $Z$  LLEs in the NTT data, though perhaps some of the older high  $Z$  LLEs if linked to the WHT late-types are an example of downsizing.

A speculative discussion of what may be inferred from the results given and discussed in this Chapter, in relation to galaxy formation scenarios, is given in section 6.2.2.

## Chapter 6

### Discussion, Conclusions and Future Work

This thesis makes a general contribution to the body of knowledge in the field of galaxy formation. The thesis represents in particular new results on an under-observed class of galaxies, LLEs. These galaxies are compared directly with the more luminous (and apparently more massive) spheroidal type galaxies, using the correlations that are measured. The correlations suggest how LLEs fit generally into the picture of galaxy formation. The conclusions of this thesis, together with some relevant discussion, are given in section 6.1 and section 6.2. Possible future work is suggested in section 6.3.

#### 6.1 Discussion and Conclusions from GCE modelling

The results from the GCE modelling, and tests of the GCE model, using the sample galaxy NGC 2831, are summarised in section 2.9. Regarding tests of the GCE model, the key findings from section 2.5 showed that the GCE model worked reliably. This reliability was demonstrated by experiments with a pseudo galaxy which showed the GCE model can reproduce model parameters for a given galaxy. Displacing the model parameters for a pseudo galaxy even up to 50% of their original values was demonstrated not to prevent recovery of the original model parameters.

However, the GCE model lacked fineness of parameter space to search relative to the SSP model, which leaves open a possible area for future research. In section 2.2, delayed feedback was discussed in regards to the GCE code; mass loss at the end of stellar lifetimes may be not fed into the cosmic cycle “on time” for stars of short enough life span compared to the

time step used. Thus, mass loss may be incorrectly modelled as instantaneous in some cases. Another key finding was that SNIa rate variance had only minor effect on the goodness of fit (see Table 2.7 and Table 2.11), as tried with the best fit model parameters found with the sample galaxy used. The SNIa rates tried were in accordance with the range of supernovae Ia values that was determined from the literature (see section 2.3). Three SNIa rates with units of  $\times 10^{-5} M_{\odot}^{-1} \text{Gyr}^{-1}$  were tried, fitting the range determined from the literature for SNIa rates; 3.8 (a lower limit, from Sansom and Proctor 1998), 6.5 (from the best fit for NGC 2831) and 12 (from the literature, as an upper limit). A further finding was that the SNIa rate and the times searched for starbursts were closely tied, more so than to other variable model parameters.

The results from investigating the entire WHT data set indicate that SO and E galaxies favour higher end SNIa rates in their SFH, and that spiral galaxy bulges favour lower end SNIa rates in their SFHs. Specifically, Es were best fit with the mid SNIa rate, SOs with the top SNIa rate, and spiral bulges with the bottom SNIa rate. A possible explanation for this is that Es and SOs have a higher rate of star formation than the bulge part of spiral galaxies, in the WHT data set.

Experiments showed that a non-solar abundance ratio model generally produces the lowest  $\chi^2$  for E type galaxies (with the mid SNIa rate applied and initial and final coefficients of star formation rate of 2 and of 0.03 respectively). They also showed, in contour plots for Es especially, that the best fits with non-solar abundance ratios were more constrained than in the solar abundance ratio case. By “constrained”, what is being referred to here is that possible solutions were fewer in parameter space and that the dip in parameter space where the best solution was found was steeper. However, the opposite is true for other galaxy types in regards to  $\chi^2$ , something which suggests that (possibly) the star formation history of spiral bulges and SOs are similar. Confidence in conclusions from this last set of experiments with the GCE model however requires a cautionary note, which is to consider the high  $\chi^2$  in the results. How confidence in future results could be increased by way of improved  $\chi^2$  is discussed in section 6.3

## **6.2 Discussion and Conclusions from Study of LLEs**

Statistically significant correlations between  $\sigma$  and Lick indices were found for the Es and SOs of the combined NTT and WHT data set, confirming the suggestion that such correlations may exist in PS02. Some observations were made about these correlations in section 5.2, from which conclusions are given in subsection 6.2.1. Section 6.2.2 suggests some possible explanations for these correlations. This leads to some of the suggestions for future work in section 6.3.

### **6.2.1 Conclusions from Study of LLEs**

The main motivational question has been answered. Low  $\sigma$  LLEs provided a continuation of the trends for SBs found in PS02. However, the combined LLE and WHT early-type galaxy data set also correlated well; an observation which taken without consideration of the K000 trend line and low number of WHT E and SO data points might suggest a link between LLEs and the WHT early-types. However, they are not positioned realistically if the K000 trend lines are to be believed. Briefly, the conclusions can be listed as:

- The LLEs in the NTT data set are located below the extrapolated positions of the trend line (from K000, as in PS02) for early-type galaxies. This suggests that the LLEs are not linked to the early-type

galaxies by way of a linear relationship between line strength and  $\log(\sigma)$ .

- The LLE and WHT SB combined data set have significant line strength versus  $\sigma$  correlations. However, there may yet be a non-linear relationship between early-types and LLEs in line strength versus  $\log(\sigma)$  plots. This is essentially an unknown. Further possible investigation regarding this possible “non-linear link” is given in section 6.3.
- The age-sensitive line strengths are all seen to decrease with  $\sigma$  in Table 5.1 (i.e. indicating age increasing with  $\sigma$ ). This may support the trend suggested in PS02 with regards to  $H\beta$ , a trend of increasing age or decreasing  $Z$  with  $\sigma$  in early-type galaxies.
- The first of these two trends appears to be supported by Figure 5.3. The latter possible trend is not supported by what is seen in Figure 5.4. These latter findings are in support of a scenario of increasing age with  $\sigma$ .
- That, however, from Figure 5.4,  $[Fe/H]$  appears to be increasing with  $\sigma$ . However, this is with a complication: that some of the LLEs may well have been misclassified in terms of morphology (see section 6.2.2).
- The results concerning age, as can be seen in Figure 5.3, indicate that the LLEs in the NTT data set are in general younger than the early-type galaxies of the WHT data set (i.e. by about 4 Gyr). The LLEs appear to be of similar age to the SBs in the WHT sample (i.e. about 2.5 Gyr). This finding makes any possible link between the

NTT data set's young LLEs and more massive, older early-types more likely;

- That the possible correlation of increasing age with  $\sigma$ , was with increased scatter at low  $\sigma$  in Figure 5.2 and Figure 5.3. A high scatter of line strengths with respect to  $\sigma$  is qualitatively as seen in CRC03.

## 6.2.2 Speculative Discussion from Study of LLEs

Now let us consider possible physical causes for the observed correlations. First, there is to consider if the correlations of line strength versus  $\sigma$  may be better in the joint LLE and late-type data sets than the joint LLE and early-type data sets. Following from subsection 6.2.1, we have that LLEs correlated well with SBs. A possible speculative explanation is that LLEs are spiral galaxies stripped of their spiral arms and discs. A lower  $\sigma$  could result in an SB becoming of reduced mass after a merger event powerful enough to remove the disc. However, since from Figure 5.3 the LLEs appear to be largely of similar age to the SBs, this would seem to be an unlikely explanation.

There is also the possibility that the LLEs are actually linked to the Es and SOs. In Figure 1.2 are shown plots of line strength versus  $\sigma$  from CRC03, which extend to a lower range in  $\sigma$  than in the WHT sample. Looking at Figure 5.1a and Figure 5.1b, the low  $\sigma$  galaxies can be seen (despite the high scatter) in most cases to be dropping below the trend lines. This could indicate that finding LLEs of low  $\sigma$  below the extrapolation from the K000 trend lines should be "as expected". Qualitatively, in comparison of appropriate plots in Figure 1.2 and Figure 5.1a and Figure 5.1b, the middle of each low  $\sigma$  data set appears to be similarly placed below the relevant trend line.

A recent private communication (Proctor, R., 2006) identified about half the NTT galaxies to be of  $Z$  low enough for them to be actually dSph type galaxies. This finding is in qualitative agreement with Table 5.4 and Figure

5.4. These galaxies were ESO 118-34, ESO 157-30, NGC 2328 and NGC 59 and a high Z sample constituting the remaining galaxies. The metallicities derived for the low Z LLEs are less than -1 dex (or -2.5 dex in the case of NGC 59). Since dSph galaxies are thought to be the basic building blocks of the larger galaxies (Read, Pontzen & Viel, 2006), this finding strengthens further the possible link between these low Z LLEs and early-types.

Regarding the LLEs of the NTT data set, to confidently state them as being linked more closely to early-type galaxies than late-type galaxies requires further evidence than that discussed above. Comparing Figure 5.3 and Figure 5.4, there is no obvious consistent separation in Z and age between the low and high Z LLEs. NGC 2328, a low Z LLE, has an age comparable to that of the older early-types, and NGC 59 has an age comparable to that of most of the high Z LLEs. This may suggest that some LLEs (i.e. NGC 2328) have grown old with relatively little star formation compared to others (e.g. NGC 1331); perhaps NGC 2328 encountered relatively few significant merger events compared to (for example) NGC 1331. Galaxies in the NTT data set that are older than galaxies in the WHT data set late-types could be found to be stripped SBs; of these there appears to be only NGC 59 (and perhaps NGC 2325) as a possibility. How the NTT data set could be further separated into high and low Z LLEs is part of the discussion for future work given below.

### **6.3 Future work**

With the aim of furthering the findings of this thesis, a number of future possible avenues of investigation were identified. To begin with, the work on GCE modelling identified a number of possible ways for improving  $\chi^2$  fits of model versus data. One way appears to be increased fineness of parameter space (as discussed in section 2.7). Two possible steps toward increased fineness of parameter space are suggested here.

Firstly, to identify which parameters (such as the gas inflow rate and the time between starbursts) in particular would benefit the GCE model by having more discrete values to search. This could be indicated, hypothetically, by finding for example a larger effect on  $\chi^2$  due to varying the C0 than varying the value of C2. Such a result would indicate that more discrete values of C0 should be tried. Conversely, if the effect on  $\chi^2$  of varying a given parameter was very little, this may suggest that no further discrete values need to be added for searching for that parameter.

The second step would be to make the fineness of parameter space adjustable, so as to minimise model computation time. The GCE model could “home in on” the best fit. The GCE code would re-run with the previous lowest  $\chi^2$  best fit parameters and a finer parameter space to search. The fineness of parameter space would be increased by adding further discrete values in an automated manner, for the model to search, and then re-running the model so as to refine the best fit.

To further test if the GCE model can distinguish between different galaxy types, an individual S0, Sa and Sb could be selected by similar criteria to NGC 2831 so as to search for C0 and C2 values that work better for these types. The best C0 and C2 found for each galaxy type could then be used to guide experiments on others of the same type. As improvements to the GCE model and code allow lower  $\chi^2$  to be achieved, the effects on indices of solar and non-solar abundance ratios may become more apparent.

The data from which the line strength versus  $\sigma$  correlations are drawn is limited by one principle effect; that affect due to the trend line relationship of the combined NTT data set and WHT data set early-types lacking mid range  $\sigma$  data points. Work to produce a mid range of comparable data points would be good starting ground for future work.

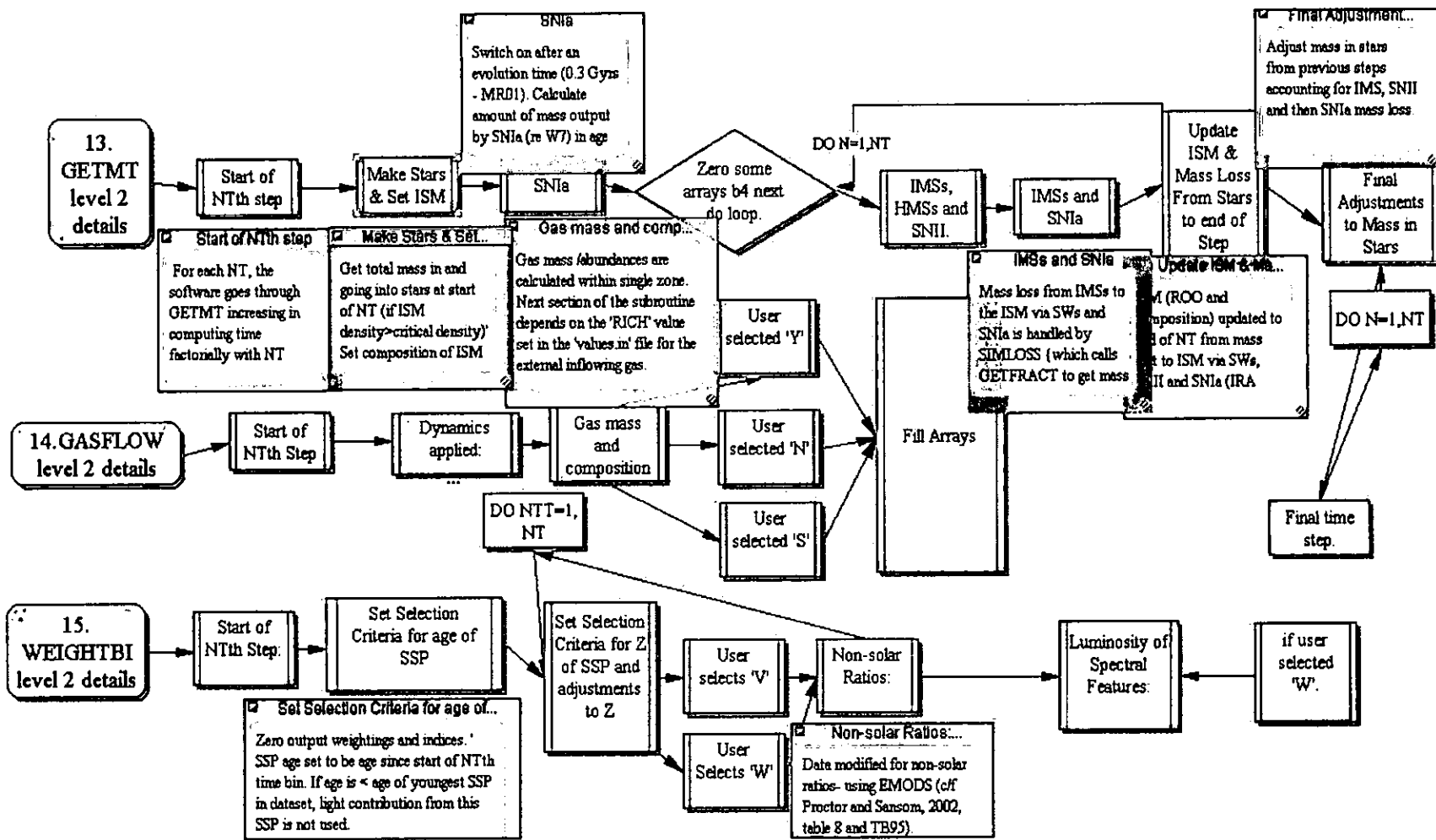
In the discussion of section 6.2, the idea that LLEs may be the building blocks of large galaxies was mentioned. This suggests a new investigation into the Z of other galaxies of data sets similar to the NTT data set. Such an investigation could provide interesting insights for galaxy formation scenarios. For example, could some fraction of the LLEs have very low Z, such as would warrant possible confidence in those particular galaxies being actually dwarf spheroidal (dSph) galaxies (private communication, Proctor,

R., 2006). If some LLEs are not at all similar to dSphs, how do they compare in  $Z$  (and age) to SBs?

If most dSphs have been accreted by larger galaxies (e.g. spiral galaxies) in the local Universe, then a comparison of LLE  $Z$ s with the old stellar halo of larger galaxies may further verify whether low  $Z$ , low  $\sigma$  LLEs are actually dSph galaxies (Read, Pontzen & Viel, 2006). If a fraction of the NTT data set was found to be probably in actuality of dSph galaxy type, then further conclusions could be inferred as to what fraction of low  $\sigma$  LLEs are actually dSph type galaxies. Such a conclusion could be further investigated by comparison studies of alleged LLE data sets and dSph data sets.

# Appendix A: GCE code detailed

Level 2 of the GCE block diagram given in Figure 2.1 is here given.



## Appendix B: Proto-type web-site

Whilst conducting experiments on the GCE model, web pages were written to attach to the on-line GCE model of Dr. Anne Sansom. This appendix provides the home page, variables page and main input form. These pages may provide some further sense of what the GCE model interface is like. The full web site can be viewed at:

[http://www.star.uclan.ac.uk/~msn/GCE\\_Home/GCE\\_index.html](http://www.star.uclan.ac.uk/~msn/GCE_Home/GCE_index.html)



UNIVERSITY  
— OF CENTRAL —  
LANCASHIRE

Galactic  
Chemical  
Evolution

Center for  
Astrophysics

### Home Page

Within the fields of astronomy and astrophysics, galactic evolution is a subject of intense research. Consideration of the light output from different galaxy types is integral to understanding the evolution of galaxies, from primordial times to the present epoch. This light is the sum of emission from individual stars composing the luminous part of galaxies. In essence, we aim to understand from this light the chemical abundances of galaxies and how these change with time. This is the subject of galactic chemical evolution (GCE), which tells us about the star formation history (SFH).

The *Extragalactic Astronomy group* within the Center for Astrophysics at the University of Central Lancashire is involved in a number of streams of research within the area of *galactic chemical evolution*.

**The GCE Computer Simulation** Galactic chemical evolution may be modeled using our GCE code. This software models chemical abundances and the resulting stellar spectral indices, to be compared to

spectral indices observed in the light from galaxies. Several variables are examined, such as those relating to star formation rate (i.e. Salpeter, with a variable efficiency as a coefficient) and the time where two major changes may have occurred. This (single zone) code allows for gas inflow during the evolution of the galaxy. The code currently predicts line strengths and colours.

A description of the inputs can be found, on the [GCE variables page](#). From here, you can link to our on-line model [GCE input form](#), which you may then use. It is planned that the on-line version of our code will be expanded as it is continued to be developed. More detailed information about galactic chemical evolution can be found on: [GCE research background](#).

#### **Contacts**

For more information on people working within the *Extragalactic Research Group*, see the following pages:

- [Anne Sansom](#) Senior Lecturer CfA
- [Mark Northeast](#) Research Student CfA
- [Robert Proctor](#) Recently graduated from CFA, currently post-doctorate at Swinburne.

---

Date Last Modified: 07/03/03

Web  
author: <mailto:MSNortheast@uclan.ac.uk>.

UNIVERSITY  
— OF CENTRAL —  
LANCASHIRE



## **Variables Page**

**Center for  
Astrophysics**

### **Page Links**

This page exists to enable the reader to study the inputs for the GCE model. The first table gives a list of the variables, including units. The 2<sup>nd</sup> table provides a more in-depth description of the variables and their limits. For the generic reader, it is advised that you follow the sections below on this page, before proceeding to the input form to run the GCE code.

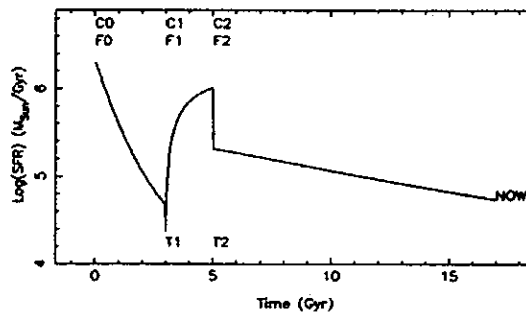
On this page:

- The Variables (*Brief summary of the variables in the GCE model, used in our code.*)
- Variable Descriptions and Limits. (*More details on the variables and their astrophysical and software derived or inferred limits.*)

On related pages:

- The GCE code input form.
- Advanced form; Link to follow when available...

The GCE code runs through the variables, assuming a galaxy evolving from the intergalactic medium, and undergoing two major changes (e.g. starbursts, such as due to a merger event) at times TCHANGE1 (T1) and TCHANGE2 (T2) (with the time between perhaps accounting for the summed effect of other such events).



An example graph of star formation rate (SFR) vs. time.

## The Variables

Variable	Short Description	Units
<u>NRR</u>	Number of radial ranges modeled in the galaxy. Default is 1.	N/A
<u>AL</u>	This is the index in the Schmidt law, for the SFR.	N/A

<u>ROOC0</u>	The number $\alpha$ which serves as the coefficient of the star formation rate	$\text{Gyr}^{-1}\text{Vol}^{-1}$ , where AL is 1
<u>RCRIT</u>	Density of the ISM below which the SFR goes to zero.	$M_{\odot}\text{Gyr}^{-1}\text{Vol}^{-1}$
<u>FLOSSLIM</u>	Limit for significant mass loss. (Fraction)	$M_{\odot}$
<u>SNIA_RATE</u>	The rate of SNIA in a galaxy.	$M_{\odot}^{-1}\text{Gyr}^{-1}$
<u>DT</u>	This is the time step limit set for the GCE, currently set by SNII.	Gyrs
<u>FLOWRATE0</u>	The inflow rate, into the ISM, from the intergalactic medium.	$M_{\odot}\text{Gyr}^{-1}$
<u>SNII</u>	The upper mass limit, considered for SN II events	$M_{\odot}$
<u>AM</u>	Index for Initial Mass Function (IMF). (Default is Salpeter).	N/A
<u>TYPIMF</u>	For IMF: S=Single slope IMF, is default. M=Modified IMF.	N/A
<u>SSPDATA</u>	The SSP data set used, to model spectral indices.	N/A
<u>X0</u>	The initial H mass fraction in the ISM gas.	N/A
<u>Y0</u>	Initial He fraction in gas	N/A
<u>Z0</u>	Initial metal fraction in gas	N/A
<u>TCHANGE1</u>	1st discrete time change	Gyr
<u>ROOC1</u>	1st changed SFR constant	$\text{Gyr}^{-1}$
<u>FLOWRATE1</u>	1st changed inflow rate	$M_{\odot}\text{Gyr}^{-1}$
<u>TCHANGE2</u>	2nd discrete time change .	Gyr
<u>ROOC2</u>	2nd changed SFR constant, which is used from time T2.	$\text{Gyr}^{-1}\text{Vol}^{-1}$
<u>FLOWRATE2</u>	2nd changed inflow rate	$M_{\odot}\text{Gyr}^{-1}$
<u>RICH</u>	Enriched inflow yes (Y) or no (N). The default is Y.	N/A

<u>BHMASS</u>	Mass of CO core for BH formation.	$M_{\odot}$
<u>TIME</u>	Time since stars started forming . The default is 17 Gyr.	Gyr

## Description and Limits of Variables

Input	Description
NRR	<p>The number of radial ranges which are modeled in the galaxy. This takes a value of 1 for single zone models (i.e. dimensionless).</p> <p>Upper and lower limits each= 1; for single zone models only.</p>
AL	<p>This is the index in the Schmidt law, for the SFR, with a value of 1.4 +/- 0.5, based partly on spirals as well as spheroidals (Kennicutt, 1998).</p> <p>Upper limit =2; Lower limit= 1</p>
ROOC0	<p>The number <math>c</math> which serves as the coefficient of the star formation rate .The SFR also depends on the gas density, in the Schmidt law (Kennicutt, R., 1998) as: <math>SFR = cp^a</math>, where <math>a = 1</math> and <math>p =</math> density of ISM. A threshold value in the SFR may be reached (<i>see RCRIT</i>); Then, SFR fails completely, to make a hard lower limit of 0. A hard upper limit could be set by the laws of thermodynamics regarding an singular open system at 1 (i.e. which assumes continuous inflow into a radial zone). Where mergers of systems occur, this value may be higher than one, however (for two spirals, 2 for example).</p> <p>In most models this co-efficient varies between 2 and 0.2, which should provide reasonable upper and lower limits (e.g. Matteucchi &amp; Recchi, 2001).</p> <p>A SFR co-efficient of 4 (assuming a galaxy such as our Galaxy, with diameter</p>

	<p>of 50 kpc and scale height of <math>\sim 400</math> pc) may be reasonable for early on in the evolution of a galaxy.</p> <p>Limits could be:</p> <p>Upper limit=4; Lower limit=0.</p>
RCRIT	<p>This is the density of the interstellar medium (ISM) below which the SFR goes to zero.</p> <p>An absolute hard limit would be zero. A hard upper limit here should be no less than the Jeans mass for a given ISM density and temperature.</p> <p>Upper limit=N/A; Lower limit=10 solar masses <math>\text{pc}^{-2}</math> (from Elmegreen, 1999).</p>
FLOSSLIM	<p>Limit for significant mass loss. (Fraction)</p> <p>From current research, a lower limit of 0.1 (10 % of each star's mass) is required if an effect is to be had on the density of the ISM.</p> <p>A hard upper limit could come from considering the fraction of matter in a galaxy that constitutes stars, and detectable changes in the amount of mass in the ISM.</p> <p>Upper limit=? (hard: 1) ; Lower limit = 0.1 (hard limit=0)</p>
SNIA_RATE	<p>The rate of SNIA in a galaxy.</p> <p>In the current GCE code (Sansom &amp; Proctor, 1998) the SN Ia rate is <math>3.8 \times 10^{-5} \text{ Gyr}^{-1} M_{\odot}^{-1}</math>. This value was derived from the models of Timmes, Woosley &amp; Weaver (1995), assuming a Galaxy mass of <math>1.4 \times 10^{11} M_{\odot}</math>. In summary SN Ia, which dominate supernovae events in early-type galaxies, appear in models and observations to have a similar rate of between <math>4.1</math> and <math>11.8 \text{ Gyr}^{-1} M_{\odot}^{-1} \times 10^{-5}</math> (in the local Universe). At larger redshifts, slightly higher SN Ia</p>

	<p>rates have been observed and fed through cosmological models to derive a rate of <math>10.4 \text{ Gyr}^{-1} M_{\odot}^{-1} \times 10^{-5}</math>. These values are converted from SNU assuming a value of <math>7.4 \times 10^{10} M_{\odot}</math> and a mass-to-light ratio of 3.4 (Carroll &amp; Ostlie, 1996, table 22.1).</p> <p>Obtaining the SNIA rate from studies of extragalactic SNIA, in field and cluster galaxies, ellipticals in particular, would be useful in inferring soft limits.</p> <p>However, a hard upper limit could be derived if half the star systems, about 2/3 of the stars in the galaxy, went SNIA inside of a single Gigayear (unlikely).</p> <p>Upper limit=<math>11.8</math>; Lower limit=<math>3.8 \text{ Gyr}^{-1} M_{\odot}^{-1} \times 10^5</math>.</p>
DT	<p>This is the time step limit set for the GCE. However, the lower limit is currently set by the GCE code.</p> <p>The time step may be decreased, based on observations of type II supernovae delayed feedback into the ISM. The delay time between leaving the MS and the supernovae explosion, and dispersion of material into the ISM, is of the order of <math>10^4</math> years. As a side note, the SNR is thought to last about 20 thousand years, after which time it is considered to have dispersed.</p> <p>Upper limit=<math>0.03</math> (hard upper limit must be less than TCHANGE1); Lower (hard) limit=<math>0.01</math>.</p>
FLOWRATE0	<p>The initial inflow rate, into the ISM, from the intergalactic medium. We arbitrarily assume an initial mass of <math>10^6 M_{\odot}</math> for the model galaxy.</p> <p>In the case of a merger, or even the effects of a close encounter, the inflow rate might be as high as <math>10^6 M_{\odot} \text{ Gyr}^{-1}</math> ! This is based on recent simulations . It may be more of the order of a 100 thousand. A galaxy is expected to overall accrete matter, in its lifetime.</p> <p>Upper limit=<math>10^7</math> ; Lower limit=<math>10^5</math> (hard limit=<math>0</math>).</p>
SNII	<p>The upper mass limit, considered for SN II events. Stars beyond this size may exist, but are considered too rare to effect the chemical abundances significantly, during the evolution of a galaxy. There</p>

	<p>is a default lower mass limit, which is set in the code at <math>8 M_{\odot}</math> (Regally, 2001). &lt;/SPAN&gt;</p> <p>Upper Limit=<math>120 M_{\text{sun}}</math>, Lower Limit= 70</p>
AM	<p>Index for Initial Mass Function (IMF). (Default is <u>Salpeter</u>), Observations of bulges may be relevant to spheroidal galaxies, which have generated indexes to the Salpeter IMF as high as 2.35 in spheroidals (Zoccali et al, 2001).</p> <p>Work has been done to investigate the validity of any IMF over the existing simple Salpeter IMF; in a study of the uncertainty inherent in any observationally deduced IMF invalidates much evidence for a variable IMF (Kroupa, 2001). These uncertainties arise from Poisson statistics of detections and stellar dynamics (such as systematic errors due to some stars being unresolved binaries). As a side note, the MFs in globular clusters appear to be, on average, systematically flatter than the Galactic-field IMF deduced in Kroupa (2001).</p> <p>Soft limits then may be: Lower=1 Upper=2.35.</p>
TYPIMF	<p>For IMF: S=Single slope IMF, is default. M=Modified IMF.</p> <p><i>The Salpeter IMF is further discussed on the <a href="#">GCE Research page</a>.</i></p>
SSPDATA	<p>The SSP data, used to model spectral indices: W=Worthey94 V=Vazdekis99.</p> <p>These refer to papers written detailing modeled spectral indices, for SSPs as discussed further on the <a href="#">GCE Research page</a>.</p>
X0	The initial H mass fraction in the ISM gas.
Y0	Initial He fraction in the ISM gas.
Z0	Initial metal fraction in the ISM gas.
TCHANGE1	First discrete time change.
ROOC1	First changed SFR constant, which is used from time T1.
FLOWRATE1	First changed inflow rate, which is used from time T1.
TCHANGE2	2nd discrete time change.

ROOC2	2nd changed SFR constant, which is used from time T2.
FLOWRATE2	2nd changed inflow rate.
RICH	Enriched inflow yes (Y) or no (N). The default is Y. The currently accepted wisdom is that the inflow into galaxies is pre-enriched. This may be, for example, by Population III stars.
BHMASS	Mass of CO core for BH formation. Currently, this is of the order of 8 solar masses.
TIME	Absolute time since stars started forming. The default is 17 Gyr, which is within errors, based on recent calculations of the Hubble Constant from the Hubble Space Telescope Key Project. Beyond the local universe, different cosmologies must be considered in interpreting co-moving rates employed in models.

## Input Form for Compose (GCE) Program

### Fixed parameters:

NRR	1	Number of radial ranges
AL	1.0	Index in SFR eqn.
RCRIT	0.0	Critical density (M/V) for SF
FLOSSLIM	0.1	Limit for significant mass loss. (Fraction)
SNIA_RATE	3.8E-5	SN Ia Number/Mo/Gyr
DT	0.03	Time step (Gyrs)
FLOWRATE0	0.0	Inflow Mo/Gyr
SNH	70.0	SN II highest mass limit
AM	1.35	Index for IMF (1.35=Salpeter)

TYPIMF	S	S=Single slope IMF M=Modified IMF
SSPDATA	V	SSP data: W=Worthey94 V=Vazdekis99
X0	0.7718	Initial H mass fraction in gas
Y0	0.2280	Initial He fraction in gas
Z0	0.0002	Initial metal fraction in gas
ROOC2	0.0	2nd changed SFR constant
FLOWRATE2	0.0	2nd changed inflow rate
RICH	Y	Enriched inflow (Y or N)
BHMASS	6.0	Mass of CO core for BH formation (Mo)
TIME	17.0	Time since stars started forming (Gyr)

**Varibale parameters:**

Const (C) in SFR=C*Ro**A (/Gyr)	ROOC0	4.0
1st discrete time change (Gyr)	TCHANGE1	2.0
1st changed SFR constant (/Gyr)	ROOC1	4.0
1st changed inflow rate (Mo/Gyr)	FLOWRATE1	1.0E+7
2nd discrete time change (Gyr)	TCHANGE2	2.4

## Appendix C: Critical values for Pearson r

Reproduced from the Web Stat URL:

[http://www.une.edu.au/WebStat/unit\\_materials/c6\\_common\\_statistical\\_tests/test\\_signif\\_pearson.html](http://www.une.edu.au/WebStat/unit_materials/c6_common_statistical_tests/test_signif_pearson.html)

Values in the table below were used to test the level of significance of correlations given in Table 5.1, Table 5.2 and Table 5.3.

df (= N-2) (N= number of pairs)	Level of significance for one-tailed test			
	.05	.025	.01	.005
	Level of significance for two-tailed test			
	.10	.05	.02	.01
8	.549	.632	.716	.765
15	.412	.482	.558	.606
25	.323	.381	.445	.487

# Bibliography

## *Papers and Books*

- Arimoto, N., & Yoshi, Y., "Chemical and photometric properties of a galactic wind model for E galaxies", 1987, A&A. 173, 23
- Baade, W., "The Resolution of Messier 32, NGC 205, and the Central Region of the Andromeda Nebula.", 1944a, ApJ, 100, 137
- Baade, W., "NGC 147 and NGC 185, Two New Members of the Local Group of Galaxies", 1944b, ApJ, 100, 147
- Ballero, S., Matteucci, F., Chiappini, C., "The effects of Population III stars and variable IMF on the chemical evolution of the Galaxy", 2006, New Astronomy, 11, 306
- Bender, R., Burstein, D., Faber, S., "Dynamically hot galaxies. I - Structural properties", 1992, ApJ, 399, 462
- Binney, J., and Tremaine, S., 1987. *Galactic Dynamics*. Princeton: Princeton University Press
- Bolzonella, M., et al. "Photometric redshifts based on standard SED fitting procedures", 2000, A&A, 363, 476
- Brosch, N., et al., "FAUST observations in the Fourth Galactic Quadrant\*\*", 2000, MNRAS, 313, 641
- Burki, G., et al., "The atmospheric extinction at the E.S.O. La Silla observatory", 1995, A&AS, 112, 383
- Buzzoni, Alberto, "Evolutionary population synthesis in stellar systems. I - A global approach", 1989, ApJS, 71, 817
- Caldwell, N., Rose, J., Concannon, K., "Star Formation Histories of Early-Type Galaxies. I. Higher Order Balmer Lines as Age Indicators", 2003, AJ, 125, 2891 (CRC03)
- Cappellaro, E., Evans, R. and Turatto, M., "A new determination of supernova rates and a comparison with indicators for galactic star formation", 1999, A&AS, 139, 531
- Carroll, B. and Ostlie, D., 1996. *An Introduction to Modern Astrophysics*. Reading Massachusetts: Addison and Wesley
- Cole, S., et al. "A Recipe for Galaxy Formation", 1994, MNRAS, 271, 781

- de Vaucouleurs, G. et al., 1991. *Third Reference Catalogue of Bright Galaxies*. New York: Springer-Verlag New York Inc.
- Dekel, A. & Cox, T., "The dissipative merger progenitors of elliptical galaxies", 2006, MNRAS, 370, 1445
- D'Onofrio, M., et al., "Major axis kinematics of 15 early-type galaxies in the Fornax cluster", 1995, A&A, 296, 319
- Faber, S., Friel, E., Burstein, D., Gaskell, C., "Old stellar populations. II - an analysis of K-giant spectra", 1985, ApJS, 57, 711
- Garcia-Segura, G., Low, M. & Langer, N., "The dynamical evolution of circumstellar gas around massive stars-I: The Impact of the time sequence O star LBV WR star", 1996, A&A, 305, 229
- Halliday, Claire, 1998. *Low Luminosity Elliptical Galaxies*. PhD thesis, University of Durham
- Heavens, A., Panter, B., Jimenez, R., and Dunlop, J., "The Complete Star Formation History of the Universe", 2004, Nature, 428, 625
- Kasten, F., "A New Table and Approximate Formula for Relative Airmass", 1966, Archiv fur Meteorologie, Geophysik und Bioklimatologie Ser. B., 14, 206
- Kasten, F., Young, A., "Revised optical air mass tables and approximation formula", 1989, Applied Optics, 28, 4735
- Kauffman, W., 1994. *Universe*. 4th ed., New York.: W.H. Freeman and Company
- Kauffman, W., 1988. *Universe*. 2nd ed., New York.: W.H. Freeman and Company
- Kuntschner, Harald, "The stellar populations of early-type galaxies in the Fornax cluster", 2000, MNRAS, 315, 184 (K000)
- Kroupa, P., "On the variation of the initial mass function", 2001, MNRAS, 322, 2, 231
- Kodama, T. and Arimoto, N., "Origin of the colour-magnitude relation of E galaxies", 1997, A&A, 320, 41
- Lacey, C. & Cole, S., "Merger Rates in Hierarchical Models of Galaxy Formation - Part Two - Comparison with N-Body Simulations", 1994, MNRAS, 271, 676

Lamers, H. & Nugis, T., "An explanation for the curious mass loss history of massive stars: From OB stars, through Luminous Blue Variables to Wolf-Rayet stars", 2002, *A&A*, 395, L1-L4

Larson, R., "Effects of supernovae on the early evolution of galaxies", 1974, *MNRAS*, 169, 229

Maeder, A., "Stellar yields as a function of initial Z and mass limit for black hole formation", 1992, *A&A*, 264, 105

Marigo, P., "Chemical Yields from Low and Intermediate Mass Stars: Model Predictions and Basic Observational Constraints", 2001, *A&A*, 370, 194

Marigo, P., Bressan, A., Chiosi, C., "The TP-AGB phase: a new model", 1996, *A&A*, 313, 545 (MBC)

Marmol-Queraltón, E., Cardiel, N., Gorgas, J., Pedraz, S., Cenarro, A., Sánchez-Blaquez, P., Peletier, R. and Vazdekis, A., "A New Stellar Library in the K Band", 2006, *MNRAS*, 370, 1213

Matteucci, Francesca, "Type Ia Supernovae and Novae: Their Roles in Galactic Chemical Evolution", 2005, American Institute of Physics Conference, 804, 237

Matteucci, F. and Recchi, S., "On the Typical Timescale for the Chemical Enrichment from Type Ia SN in Galaxies", 2001, *ApJ*, 558, 351

Mehlert, D., Thomas, D., Saglia, R., Bender, R. and Wegner, G., "Spatially Resolved Spectroscopy of Coma Cluster Early-type Galaxies, III. The stellar population gradients", 2003, *A&A*, 407, 423

Mihos, J. and Hernquist, L., "Gasdynamics and Starbursts in Major Merger", 1996, *ApJ*, 464, 641

Navasardyan, H., et al. "SN in isolated galaxies, in pairs and in groups of galaxies", 2001, *MNRAS*, 328, 4, 1181

Pain, R., et al. "The Distant Type Ia Supernova Rate", 2002, *ApJ*, 577, 120

Poggianti, B., et al., "A Photometric and Spectroscopic Study of Dwarf and Giant Galaxies in the Coma Cluster. III. Spectral Ages and Metallicities", 2001, *ApJ*, 562, 689

Poggianti, B., et al., "Two Formation Paths for Cluster Dwarf Galaxies?", 2004, *IAUS*, 217, 562

Proctor, R., and Sansom, A., "A Comparison of Stellar Populations in Galaxy Spheroids Across a Wide Range of Hubble Types", 2002, *MNRAS*, 333, pp.517 (PS02)

- Proctor, Robert, 2002, *Metallicities and Stellar Populations in Spiral Bulges*. PhD thesis, University of Central Lancashire
- Puzia, T., Saglia, R., Kissler-Patig, M., Maraston, C., Greggio, L., Renzini, A. & Ortolani, S., "Integrated Spectroscopy of Bulge Globular Clusters and Fields. I. The data base and comparison of individual Lick indices in clusters and bulge", 2006, A&A, 395, 45
- Read, J., Pontzen, A. & Viel, M., "On the formation of dwarf galaxies and stellar haloes", 2006, MNRAS, 821
- Reduzzi, L. and Rampazzo, R., "Candidates for a southern extension of the Karachentsev catalogue of isolated pairs of galaxies", 1995, Astrophysical Letters & Communications, 30, 1
- Regaly, Z., "Numerical Modelling of SN Type II", 2001, Publications of the Astronomy Department of the Eötvös University, 11, 95
- Renzini, A., and Voli, M., "Advanced evolutionary stages of intermediate-mass stars. I - Evolution of surface compositions", 1981, A&A, 94, 175 (RV81)
- Roos, M., 2003. *Introduction to Cosmology*. 3rd ed., Chichester: John Wiley & Sons. Ltd
- Salpeter, E.E., "The Luminosity Function and Stellar Evolution.", 1955, ApJ 121, 161
- Samland, M., "Modelling the Evolution of Disk Galaxies. II. Yields of Massive Stars", 1998, ApJ, 496, 155
- Sansom, A., and Proctor, R., "Pre-enriched, not primordial ellipticals", 1998, MNRAS, 297, 953
- Sargent, W., Schechter, P., Bokserberg A. and Shorridge, K., "Velocity dispersions for 13 galaxies", 1997, ApJ, 212, 326
- Shields, A., "Chemical Evolution of Galaxies", 2002, RevMexAA (Serie de Conferencias), 12, 189
- Sil'chenko, O., "Stellar Populations in Nearby Lenticular Galaxies", 2006, ApJ, 641, 229
- Sparke, L., and Gallagher, J., 2000. *Galaxies in the Universe: an Introduction*. 3rd ed. s.l.: Cambridge University Press
- Spergel et al., "First Year Wilkinson Microwave Anisotropy Probe (WMAP) Observations: Determination of Cosmological Parameters", ApJ, 594, 279

- Sullivan, M., et al., "The Hubble diagram of type Ia supernovae as a function of host galaxy morphology", 2003, MNRAS, 340, 1057
- Tantalo, R., et al. "Spectro-photometric evolution of elliptical galaxies. III. Infall models with gradients in mass density and star formation", 1998, A&A, 335, 823
- Thomas, D., Maraston, C., and Bender, R., "New clues on the calcium underabundance in early-type galaxies", 2003a, MNRAS, 343, 279
- Thomas, D., Maraston, C., and Bender, R., "Stellar population models of Lick indices with variable element abundance ratios", 2003b, MNRAS, 339, 897
- Timmes, F., Woosley, S., & Weaver, T., "Galactic Chemical Evolution, Hydrogen through Zinc", 1995, ApJS, 98, 617
- Tinsley, B. M., "Constraints on models for chemical evolution in the solar neighborhood", 1974, ApJ, 192, 629
- Tinsley, B. M., "Chemical evolution in the solar neighborhood. IV - Some revised general equations and a specific model", 1981, ApJ, 250, 758
- Trager, S., Worthey, G., Faber, S., Dressler, A., "Hot stars in old stellar populations: a continuing need for intermediate ages", 2005, MNRAS, 362, 2
- Trager, S.C., Faber, S.M., Worthey, G. and Gonzalez, J.J., "The Stellar Population of Early-Type Galaxies 2. Controlling Parameters of the Stellar Populations", 2000, AJ, 120, 1, 165
- Tripicco, M & Bell, R., "Modelling the LICK/IDS Spectral Feature Indices Using Synthetic Spectra", 1995, AJ, 110, 3035
- Wallerstein G., "Abundances in G. Dwarfs. VI. a Survey of Field Stars", 1962, ApJS, 6, 407
- Wallerstein G., Greenstein J., Parker R, Helfer H., and Aller L., "Red Giants with Extreme Metal Deficiencies", 1963, ApJ, 137, 280
- Wood, M., "Constraints on the Age and Evolution of the Galaxy From the White Dwarf Luminosity Function", 1992, ApJ, 386, 539
- Worthey, G. and Ottaviani, D., "H gamma and H delta Absorption Features in Stars and Stellar Populations", 1997, ApJS, 111, 377
- Worthey, G., "Comprehensive Stellar population Models and the Disentanglement of Age and Z Effects", 1994, ApJS, 95, 1, 107

Woosley, S. and Weaver, T., "The Evolution and Explosion of Massive Stars. II. Explosive Hydrodynamics and Nucleosynthesis", 1995, ApJS, 101, 181

Woosley, S., Langer, N., Weaver, Thomas A., "The evolution of massive stars including mass loss - Presupernova models and explosion", 1993, ApJ, 411, 823

Vazdekis, A., "Evolutionary Stellar Population Synthesis at 2 C<sub>2</sub> Spectral Resolution", 1999, ApJ, 513, 224

### ***Conferences***

National Astronomical Meeting 2003, Dublin: Trinity College (NAM03)

Stellar Populations '03 conference on the properties, applications and study of stellar populations, 6th-11th October, 2003. Garching: Max-Planck-Institut für Astrophysik. *Proceedings not published.* (SPS03)

### ***Electronic***

"Annotated SPSS Output Regression Analysis". Available at:  
URL:[http://www.ats.ucla.edu/STAT/SPSS/output/reg\\_spss.htm](http://www.ats.ucla.edu/STAT/SPSS/output/reg_spss.htm), [Last accessed September 2006].

"EMMI : ESO Multi-Mode Instrument". Available at:  
<URL:<http://www.ls.eso.org/lasilla/Telescopes/NEWNTT/emmi/>>, [Last accessed November 2005]. (EW)

"FORIS Exposure Time Calculator", 2003. Available at:  
<http://www.eso.org/observing/etc/bin/gen/form?>>, [Last accessed November 2003].

Hymes, R., 2003, "Magnitude to Flux Converter". Available at:  
<URL:[http://www.astro.soton.ac.uk/~sim\\_rih/applets/MagCalc.html](http://www.astro.soton.ac.uk/~sim_rih/applets/MagCalc.html)>, [Last accessed October 2003].

"Hypercat archive", 2003. Available at: <URL:<http://www-obs.univ-lyon1.fr/hypercat/>>, [Last accessed July 2006].

"HyperLeda", Available at: <URL:<http://leda.univ-lyon1.fr/>>, [Last accessed August 2006]

"Nasa Extragalactic Database", 2002. Available at:  
URL:<http://nedwww.ipac.caltech.edu/>, [Last accessed July 2006].(NED)

"RA Ordered List of Spectrophotometric Standards", 1992. Available at:  
<URL:<http://www.eso.org/observing/standards/spectra/stanlis.html>>, [Last accessed August 2006].

"SIMBAD Astronomical Database", Available at: <URL:<http://simbad.u-strasbg.fr/>>, [Last accessed August 2006].

SDSS web page, Available at:URL:<<http://www.sdss.org>>, [Last accessed December 2006]

WMAP Mission Results, 2003. Available at:  
<URL:[http://map.gsfc.nasa.gov/m/\\_mm/mr/\\_firststars.html](http://map.gsfc.nasa.gov/m/_mm/mr/_firststars.html)>, [Last Accessed December 2003].